

# **Stony Brook University**



OFFICIAL COPY

**The official electronic file of this thesis or dissertation is maintained by the University Libraries on behalf of The Graduate School at Stony Brook University.**

**© All Rights Reserved by Author.**

# **Vulnerable Plaque Risk of Rupture Examined via Patient Based Micro-CT and IVUS Fluid-Structure Interaction Studies**

A Thesis Presented

by

**Xuan Liang**

to

The Graduate School

in Partial Fulfillment of the

Requirements

for the Degree of

**Master of Science**

in

**Biomedical Engineering**

Stony Brook University

**December 2011**

Copyright by  
Xuan Liang  
2011

**Stony Brook University**

The Graduate School

**Xuan Liang**

We, the thesis committee for the above candidate for the  
Master of Science degree, hereby recommend  
acceptance of this thesis.

**Danny Bluestein– Thesis Advisor  
Professor, Biomedical Engineering**

**Yi-Xian Qin – Inside Committee Member  
Professor, Biomedical Engineering**

**Barry Baruch Lieber – Inside Committee Member  
Professor, Neurological Surgery**

This thesis is accepted by the Graduate School

Lawrence Martin  
Dean of the Graduate School

Abstract of the Thesis

# **Vulnerable Plaque Risk of Rupture Examined via Patient Based Micro-CT and IVUS Fluid-Structure Interaction Studies**

by

**Xuan Liang**

**Master of Science**

in

**Biomedical Engineering**

Stony Brook University

**2011**

Fluid-structure interaction (FSI) simulations were conducted in patient-specific coronary vulnerable plaque (VP) geometries reconstructed from Micro-CT and intravascular ultrasound (IVUS), in order to study the effects of several biomechanical factors on plaque vulnerability. The models reconstructed from IVUS included vessel wall, fibrous cap, lipid core and large calcifications. A model reconstructed post mortem from a coronary specimen of a patient with confirmed VP was scanned using high resolution micro-CT. This enabled capture of micro calcifications embedded in the VP fibrous cap in addition to the plaque components mentioned above. Regions susceptible to tissue failure were studied. The thin fibrous cap regions of the plaque were characterized by high stress concentrations. The presence of single or multiple micro-calcified spots embedded within the fibrous cap was studied as well. Micro-Ca

significantly enhanced stresses within the fibrous cap, significantly contributing to the risk of rupture. Micro-Ca embedded in the fibrous cap produced increased stresses predicted by previously published analytical model, and corroborated our previous studies. The ‘micro-CT to FSI’ methodology may offer better diagnostic tools for clinicians, while reducing morbidity and mortality rates for patients with vulnerable plaques and ameliorating the ensuing healthcare costs. Similarly, Fluid-Structure-Interaction (FSI) simulations of three-dimensional patient-based geometries of coronary arteries reconstructed based on Intravascular Ultrasound (IVUS) imaging dataset were performed to elucidate the correlation and dependence of crucial biomechanical risk factors, such as the fibrous cap thickness, hypertension, presence of microcalcification (micro-Ca) in the fibrous cap, and arterial anisotropy, in stress/strain distributions. It was verified that von Mises stress would exponentially increase with a fibrous cap thinner than  $65 \mu\text{m}$ . On average, von Mises stresses increased by 32%, 34%, 30%, and 34% following a 25% simulated blood pressure elevation in the four cases studied. Stress-driven reorientation and biochemically degradation of the collagen fibers in the vessel due to atherosclerosis would potentially result in an anisotropic fibrous cap with  $65^\circ$  degree fiber angles. Compared to its isotropic counterpart, a 23% von Mises stress increase was observed when the fibrous cap containing a micro-Ca was modeled as anisotropic material. IVUS based patient specific FSI simulations mapping the wall stresses and analyzing the biomechanical risk factors can be used as an additional tool for clinicians to determine proper treatment and intervention.

## Table of Contents

1. Introduction.....	1
a. Cardiovascular Disease Statistics	
b. Atherosclerosis In General	
c. Pathophysiology of Vulnerable Plaque In Human Vascular System: Especially Coronary.	
d. Biomechanical Factors in Details (Coronary Vulnerable Plaque Stability)	
e. Material Models: Vessel Behavior (Compare & Contrast)	
f. Medical Imaging Modalities Used For Plaque Evaluation (IVUS / microCT / Angiography)	
i. Intravascular Ultrasound Imaging Protocol	
ii. Micro-Computed Tomography Protocol.	
g. Three-dimensional reconstruction of the structures	
h. Computational Models	
i. FSI Approaches: BFL Approach for VP	
2. Methodology.....	11
a. Patient data acquisition using Micro-CT	
b. Reconstruction from Micro-CT	
c. Patient Data Acquisition Using IVUS.	
d. Reconstruction from IVUS	
e. Hypertensive and microcalcified cases.	
f. Material Models	

i.	Isotropic material models for vessel and fibrous cap	
ii.	Anisotropic material model for fibrous cap	
g.	FSI Methodology	
h.	Grid Independency Studies and Computational Capacity	
3.	Results.....	23
a.	Studies Performed On Idealized Geometries	
i.	General Hemodynamics for Geometries with Various Prestretch	
ii.	Vessel Only Anisotropic Simulations: Severe Stenosis.	
iii.	Vessel Only Anisotropic Simulations: Mild Stenosis	
iv.	Vessel Only Different Collagen Fiber Orientations	
v.	Effects of Fiber Angles- Fluid-Structure-Interaction ( FSI) Studies	
vi.	Summary of the parametric study of fiber orientations	
vii.	Influence of Micro-Ca Size and Shape	
1.	Mesh Independency Studies	
b.	Patient-specific baseline models	
c.	The effect of hypertension	
d.	The effect of microcalcification (micro-Ca)	
e.	The effect of anisotropy of the fibrous cap	
f.	Geometry reconstructed from Micro-CT imaging data.	
g.	Hemodynamics of VP	
h.	Overview of VP arterial wall dynamics and effects of micro-Ca on fibrous cap	
i.	Effect of microcalcifications on stresses developing in the fibrous cap	
j.	Stress distribution around the microcalcifications	



k. Phase-lag between peak pressure and maximal flow	
4. Discussion.....	54
a. IVUS Perspectives	
b. Micro-CT Perspectives	
5. Conclusions.....	66
References.....	68
Appendix.....	73
a. Mathematical derivations	
i. Iso & anisotropic strain energy function to Cauchy Stress/Strain Relationship	

**List of Tables:**

**Table 1:** Material Parameters determined for the material model used in our simulations .....16

**Table 2:** Influence of different prestretching on peak stress calculated.....25

**Table3:** Axial Pre-stretch (Units: Stress, Pa).....26

**Table 4:** Axial Pre-stretch In Order To Eliminate Irregular Bending.....27

**Table 5:** Stresses at Systole.....27

**Table 6:** Stresses at diastole for healthy fiber angles (5, 90 Deg) and also pathological fiber angle (65 Deg).....29

**Table 7:** Stresses associated with different angles and pre-stretches.....30

**Table 8:** Stresses extracted from FSI simulation at different fiber angles (Pa).....32

**Table 9:** Diseased Arteries and plaque characterizations.....37

**Table 10:** Summary of max von Mises stress, MAP stress, peak velocity, peak wall shear stress, and Principal Axis 1 ( $p_1$ ) stress.....45

**Table 11:** Material Parameters determined for the material model used in our FSI simulations .....52

**Table 12:** Fibrous cap stress results, flow and wall shear stress (WSS) values.....53

**List of Figures:**

**Figure 1A:** Number of deaths caused by various commonly known diseases, in which cardiovascular disease is the leading culprit. 1B: Pie chart representing the percentage breakdown of deaths within the group of cardiovascular diseases, coronary heart disease is responsible for majority of the deaths. 1C: Bar charts reflecting the health care cost of major cardiovascular diseases, coronary heart disease easily out-competes other major leading ones .....3

**Figure 2:** On top, it shows the relative position of coronary arteries on the surface of the heart. Coronary arteries are direct nutrients and oxygen sources for the myocardial muscles fibers. On the bottom, it briefly represents the cascade of the formation of the plaques. Low density lipoproteins get absorbed by the arterial wall to trigger the activation of endothelial cell surface receptors followed by the inflammatory reactions. Upon biochemical modifications, lipids absorbed or penetrated into the vessel wall become cells filled with lipids and inflammatory cells .....7

**Figure 3:** A: Stress-Stretch fitting curves generated from anisotropic Mooney-Rivlin model and experimental data of fibrous cap from human iliac artery. B & C: Stress-strain curves fitted with anisotropic material model separated by axial and circumferential directions.....18

**Figure 4:** Stress-strain curves generated from Mooney-Rivlin anisotropic material model tried to fit the experimental data of human coronary cadaver sample taken from different research groups. It actually shows the variation on the material data obtained for the same type of vessel from different groups. However, the trend, which vessel as soft tissue is much stiffer in the circumferential than axial direction and it closely assembles the physiological conditions that vessels undergo much larger expansions than stretching.....20

**Figure5:** Coronary geometry meshed in ADINA, solid and fluid domains are shown. Lower figure shows the boundary conditions, fixed at one end of the solid domain and free to move in the other end. For the fluid domain, all faces that are interacting with the solid domain are assigned with No-slip and FSI boundary conditions.....23

**Figure6:** Stress distribution, peak stress and blood velocity profile. Figure 5A shows the band plot of smoothed effective stress (von Mises stress) that represents the FSI model of isotropic coronary artery with lipid core. The peak stress at peak systole is 92,060 Pa. The lower image shows the flow field of the pathological coronary artery. Peak stress is shown on graph to be occurred at the surface of thin fibrous cap on upstream.....24

**Figure 7:** This figure shows the pathological fiber angle (65 Deg) increases the maximum stress at systolic pressure.....28

**Figure 8:** This figure shows the pathological fiber angle (65 Deg) increases the maximum stress at diastolic pressure.....29

**Figure 9:** (5 degree fiber angle): Smoothed effective stress and principal axial stress distributions. Zoomed in at stenosis region to identify maximum values.....31

**Figure 10:** (65 degree fiber angle) principal axial stress distribution and zoomed in at stenosis region at peak systole. In addition, velocity distribution is shown as well.....32

**Figure11:** Optimizing the mesh size until proper grid was reached that mesh independent results would be received. Coarser grid on the left and finer one on the right reveal the grid size definitely influences the stress distribution in the simulations.....34

**Figure 12:** Left: stress contour plots at the cross-sections in the fibrous cap region where in one case microcalcification was embedded. It revealed that the appearance of the microcalcification would change the location of peak stress predicted by the analysis. Right, zoomed in at the exact location where microcalcification was inserted and it showed that locally, microCa would present a bipolar high stress distribution along the tensile direction.....35

**Figure 13:** Band plot of von Mises stress distributions in all three cases showing higher stress regions can be found in the fibrous caps with the presence of micro-Ca. As shown in the figure, stress values would be substantially high at the poles of the inclusion.....36

**Figure 14:** Band plot of von Mises stress distributions (Isotropic Material Model) in all three cases showing higher stress regions can be found in the fibrous caps. As shown in the figure, stress values substantially increase and respond exponentially to the thinning of fibrous cap thickness. On average, F.C. thickness is reducing from Case I ~ Case III.....39

**Figure 15:** (a) reconstructed coronary artery (Case I): This geometry is composed of the arterial wall in silver, macrocalcification in white and necrotic core in red. (b) Pressure and mean flow velocity extracted from patient based coronary measurement and they were applied at the outlet and inlet of the vessel, respectively [1]. (c) Three dimensional representation of the axial and circumferential Cauchy stress over corresponding stretches for fibrous cap with 65 degree fiber angle.....40

**Figure 16:** Fluid wall shear stress (WSS) and velocity profiles at 4 different stages of the cardiac cycle for Case I. (Top: From Left to Right): Flow waveform at diastole, systole, peak flow rate, mean arterial pressure, and overlapped pressure and flow waveform showing a phase shifted condition. Maximum WSS and velocity can be found in the region of maximum stenosis (60%). WSS and velocity are low at systole but remain high at MAP due to the phase lag.....41

**Figure 17:** Zoom-in view of the von Mises stress distributions along the fibrous cap from three hypertensive simulations. Hypertension increases the stress concentration in the fibrous cap and almost linear relationship of peak pressure and maximum stress can be derived.....43

**Figure 18:** Cross-sectional view of the vessels, local (background) stress distributions show the effects of miniaturized calcified spot in the fibrous cap with isotropic material properties. 2.4, 2.6, and 2.2-fold increase of von Mises stress on the cross-sectional plane, where micro-Ca are

located, can be observed compared to the local stresses at the same cross-section without micro-Ca.....44

**Figure 19:** Coronary vulnerable plaque 3D reconstruction from MicroCT. (A) – (D) 3-D reconstruction of coronary vessel with atheromatous lesion is shown. Wall and lumen of vessel are shown in (A). Fibrous cap of atheromatous lesion is displayed in green (B). Fatty lipid core is shown in blue (C). Several macrocalcifications are shown in white (D). Microcalcification landmarks are presented overlaying the fibrous cap in 3-D view (E) and cross-sectional view (F). Arrows in (E) and (F) point out the three microcalcifications.....47

**Figure 20:** Fluid domain results from FSI simulations. Velocity and wall shear stress (WSS) profiles of the coronary artery under dynamic pulsatile conditions with phase lag are shown at three stages of the cardiac cycle: peak systole (0.4s), early diastole – peak flow (0.6s), and late diastole – flow deceleration (0.9s). Region of highest velocity and wall shear stress is located at the region of maximum stenosis (47.6% compared to inlet). This region of stenosis corresponds to the pathology of interest, the coronary vulnerable plaque (CVP). It is observed that WSS remains high throughout the cardiac cycle.....49

**Figure 21:** The effect of micro-Ca on fibrous cap stress. Three micro-Ca embedded in the fibrous cap, using micro-CT, were simulated using FSI. All three micro-Ca were simulated together in the same geometry. Cross sections of the CVP geometry are shown at the axial level for the three micro-Ca. Corresponding results are shown for the same axial levels without embedded micro-Ca (control simulations). Maximum von Mises stress results, reported for each cross section individually, show a 2.15-fold increase in the local stress values of the fibrous cap with micro-Ca inclusion (paired *t*-Test,  $p < 0.015$ ).....51

**Figure 22:** Principal stress,  $p_2$ , distribution at the microcalcified region. (a) Principal stress along the fibrous cap with isotropic material properties is shown. (b) Stress values increase from 29.2 kPa (without micro-Ca) to 57.8 kPa (with micro-Ca) for the first micro-Ca (geometry with and without the computational grid). (c) Stress values increase from 35.5 kPa (without micro-Ca) to 67.8 kPa (with micro-Ca) for the second embedded micro-Ca. (d) Stress values increase from 34.8 kPa (without micro-Ca) to 88.8 kPa (with micro-Ca) for the third embedded micro-Ca....53

**Figure 23:** a) Relationship between pressure and flow rate for  $\alpha=3.34$ . b). Phase lag between pressure and flow as a function of  $\alpha$ .....59

**Figure 24:** Cauchy stress versus the axial and circumferential stretches for fibrous cap anisotropic material properties. The mechanical response predicted from the constitutive model shows apparent stiffening in vessel with 65 degree fiber orientation compared to 5 degree fiber orientation.....60

## List of Abbreviations

*CVD*-Cardiovascular Disease

*VP*-Vulnerable Plaque

*F.C*-Fibrous Cap

*LAD*-Left Anterior Descending

*MacroCa*-Macrocalcification

*MicroCa*-Microcalcification

*N.C*-Necrotic Core

*AAA*-Abdominal Aortic Aneurysm

*VCAM*-Vascular Cell adhesion Molecules

*IVUS-VH*-Intravascular Ultrasound Virtual Histology

*R.F*-Radio Frequency

*MicroCT*-Micro-Computed Tomography

*IKI*-Iodine Potassium Iodide

*FSI*-Fluid Structure Interaction

*ADINA*-Automatic Dynamic Incremental Nonlinear Analysis

*M-R*-Mooney Rivlin

*ATS*-Automatic Time Stepping

*FEM*-Finite Element Method

Title

**Vulnerable Plaque Risk of Rupture  
Examined via Patient Based Micro-CT and  
IVUS Fluid-Structure Interaction Studies**

## **Introduction:**

### *a. Cardiovascular Disease Statistics*

Cardiovascular disease (CVD) is the leading cause of death in developed countries, and it is rapidly becoming the number one killer in the developing countries [2]. According to current estimates, 61,800,000 Americans have single or multiple types of cardiovascular disease [3]. Every year, more than 1 million people in the United States and greater than 19 million others worldwide experience a sudden cardiac event (acute coronary syndromes and/or sudden cardiac death). Total CVD include hypertension, congenital cardiovascular defects, stroke, and coronary heart disease *et al.* Amongst them, coronary heart disease is on top for both the number of incidents happened per year and total direct or indirect health care cost (Figure 1). CVD accounted for 38% of all death in Women and 24% in men. Moreover, half of the deaths directly or indirectly related to CVD occurred below the age of 70 years in the developing countries and this number was much lower, only a quarter, in the developed countries. CVDs are expected to remain the main cause of death globally within the next 15 years due to a still fast increasing dominance in developing countries. Initially, the treatment of hypercholesterolemia and hypertension was expected to dramatically decrease the effect of CVD and even eliminate it. However, rapidly growing incidence of obesity and diabetic related diseases in the western world also contributes greatly to the long term effects. Many of these people have no prior symptoms [4], so definitely there is considerable demand for investigations of the pathologic conditions that underlie these sudden cardiac events.



Type of disease	# of deaths
CVD	910,614
Cancer	554,643
Alzheimer	63,343
HIV	13,544
Accident	105,695

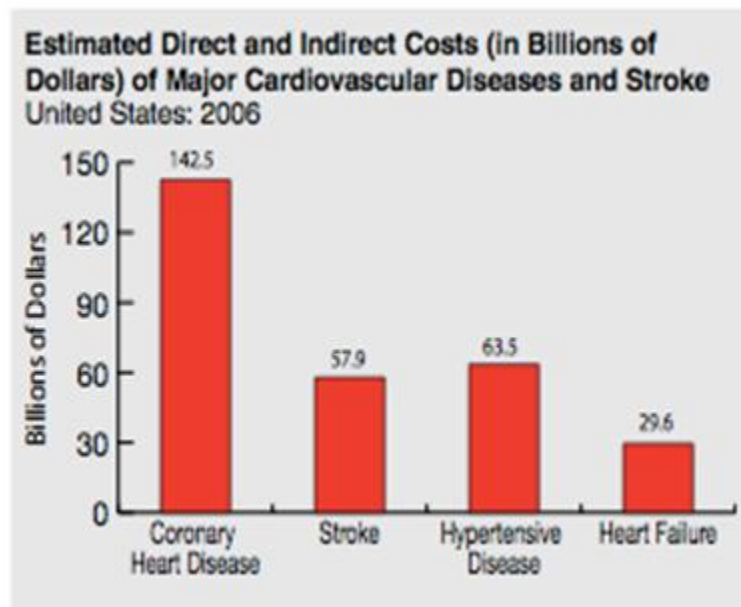
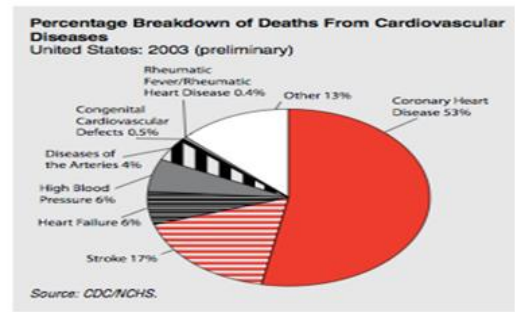


**Figure 1A:** Number of deaths caused by various commonly known diseases, in which cardiovascular disease is the leading culprit. **1B:** Pie chart representing the percentage breakdown of deaths within the group of cardiovascular diseases, coronary heart disease is responsible for majority of the deaths. **1C:** Bar charts reflecting the health care cost of major cardiovascular diseases, coronary heart disease easily out-competes other major leading ones.

*b. Atherosclerosis In general*

Research has confirmed that inflammation plays a very important role in the initiation and development of coronary artery disease. It has been proven that the atherosclerosis is the main cause of CAD and it is an inflammatory process that immune system combining with metabolic

risk factors together to initiate, propagate, and activate lesions in the arterial tree[5]. Atherosclerosis is defined as the focal thickenings of the innermost layer of the artery, more specifically, the intima. Atherosclerotic lesions usually are composed of cells, connective-tissue elements, lipids, and debris. A typical atheroma consists of inflammatory and immune cells in substantial amount and vascular endothelial and smooth muscle cells as the remainder. Previously, continuous luminal narrowing from the growth of smooth-muscle cells in the plaque was considered as the major cause of infarction. Lately, based on the results from the angiographic studies, it has been observed that severe stenosis was not highly correlated with identified culprit lesions. It is evident that the activation and progression of plaque rather than stenosis are more relevant biomarkers. Generally speaking, the formation of the vulnerable plaque is initiated by the deposition of the lipids in the blood stream on vessel wall and gradually absorbed by the tissue. Then, endothelial cells being activated would trigger the inflammation cascade. More specifically, inflammatory cells, such as macrophages, will mix with the lipids on site and get penetrated into the vessel wall forming the plaque (Figure 2). As the disease progresses, vessel remodels to try to overcome or reverse the process. Without proper intervention or treatment, plaque thinning will eventually lead to rupture. Heart attack may occur if the contents inside the lipid layer are in direct contact with the blood stream.

*c. Pathophysiology of Vulnerable Plaque In Human Vascular System: Especially Coronary*

Vulnerable plaque (VP) is atherosclerotic plaque that is covered by a thin fibrous cap which during an irregular process can lead to rupture causing thrombosis [6]. The rupture of the vulnerable coronary plaque is widely recognized as the principal cause of all unstable coronary syndromes such as acute myocardial infarction or unstable angina. More specifically, most acute coronary syndrome occurs when there is an insufficient supply of oxygen from the coronary

artery to support myocardial demand and is resulted from sudden luminal thrombosis [7]. Luminal thrombosis can be a result from plaque rupture, erosion and calcified spot embedded in or adjacent to the fibrous cap [8]. Fibrous cap (FC) formation occurs as a result of progression from a macrophage-rich fatty streak lesion [6]. The FC is a layer of fibrous connective tissue that arises from the migration and proliferation of vascular smooth muscle cells and is composed of macrophages, smooth muscle cells, foam cells and lymphocytes. The vulnerable plaque is defined as a lesion with a fibrous cap  $<65 \mu\text{m}$  thick and infiltrated by macrophages ( $>25$  cells per  $0.3\text{mm}$  diameter field). Over 50% of fibrous caps are distributed in the proximal artery and most frequently in the left anterior descending (LAD) artery [9]. Virmani [7-15] et al. defined vulnerable plaque rupture as a thin fibrous cap ( $23 \pm 19 \mu\text{M}$ ) heavily infiltrated by macrophage, T-cells, and an underneath necrotic core that is in direct contact with flowing blood promoting luminal thrombus. Plaque morphology has been widely considered to play an important role in determining plaque vulnerability as well as clinical outcome. Thinning and losing collagen content of the fibrous cap increase plaque vulnerability [16, 17]. Dhume et al. measured the thickness of the fibrous caps in the carotid artery from the adventitial side to the luminal end at the widest portion of the fibrous cap. They reported that the mean thickness of the fibrous cap from asymptomatic plaques was  $129 \pm 10 \mu\text{M}$ , while that from symptomatic plaques was  $35 \pm 3 \mu\text{M}$  [18]. Burke et al. further defined this lesion as containing a fibrous cap less than  $65 \mu\text{M}$  thick. The  $65 \mu\text{M}$  thickness in cases with vulnerable plaque was chosen as a criterion of the assessment of vulnerability because in arteries with ruptured plaque, the mean cap thickness was found to be  $23 \pm 19 \mu\text{M}$  and 95% of the caps actually measured less than  $64 \mu\text{M}$

#### *d. Biomechanical Factors in Details (Coronary Vulnerable Plaque Stability)*

Coronary calcification has shown high correlation with plaque burden [8, 10, 19, 20]. Its precise mechanism that directs the shift of critical stresses remains a mystery since macrocalcifications underlying or adjacent to a lipid-rich necrotic core have been proposed to have a stabilizing effect [21, 22]. However, Vengrenyuk *et al* introduced that stress-induced debonding of micro-Ca embedded in fibrous cap can activate the rupture of thin-cap fibroatheroma [20]. These micro-Ca are dangerous when appearing near the region of high peak circumferential stress. The spherical inclusion, which sizes range from 10 to 20  $\mu\text{m}$ , will intensify the local stress to 545kPa or higher when the cap thickness is less than 65  $\mu\text{m}$  [23]. It has been suggested that early calcification formation in coronary arteries is an active process and results from calcification of smooth muscle cell organelles [12]. Additionally, pulse pressure is a well-recognized biomarker routinely used for the risk assessment of cardiovascular diseases [24, 25]. For instance, hypertension has been considered to play a role in the pathogenesis and rupture risk of abdominal aortic aneurysm [26]. However, the influence of hypertension on coronary vulnerable plaque is not well established.

The orientation of the collagen fibers in the subendothelial layer is not uniform through the thickness of the vessel [27]. In the early stage of pathogenesis, patches of arterial endothelial cells start to secrete adhesion molecules, which can bind to leukocytes, and the expression of these molecules is characterized as a response to vascular injury where eventually develop atheroma [28]. Macrophages accumulate within regions of high stress, usually at the shoulders of the fibrous plaque and express the multi-domain enzyme MMP-9. These enzymes contribute to the vulnerability of the plaque by slowly degrading collagen type I fibers and elastin, decreasing

the tensile strength of the tissue allowing it to be more prone to rupture. Macrophages are the cells predominantly occurred at the immediate site of either rupture or superficial erosion of the fibrous cap [29].

*e. Material Models: Vessel Behavior (Compare & Contrast)*

The artery has three main layers; intima, media and adventia. The intima (innermost layer) comprises of a single layer of endothelial cells lining the arterial wall and subendothelial layer.

The orientation of the collagen fibers in the subendothelial layer is not uniform through the thickness of the layer [27]. Normal endothelium cells do not in general support binding of white

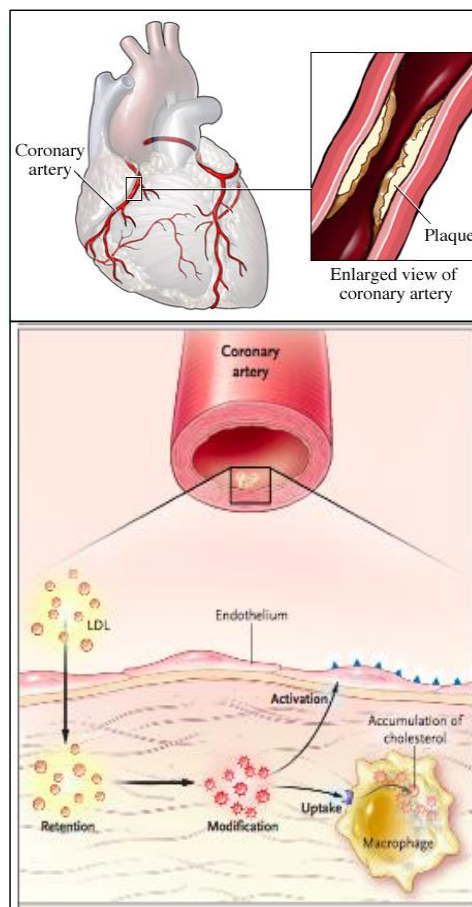


**Figure 2: On top, it shows the relative position of coronary arteries on the surface of the heart. Coronary arteries are direct nutrients and oxygen sources for the myocardial muscles fibers. On the bottom, it briefly represents the cascade of the formation of the plaques. Low density lipoproteins get absorbed by the arterial wall to trigger the activation of endothelial cell surface receptors followed by the inflammatory reactions. Upon biochemical modifications, lipids absorbed or penetrated into the vessel wall become cells filled with lipids and inflammatory cells.**

blood cells. In the early initiation of an atherogenic diet, patches of arterial endothelial cells

begin to express selective adhesion molecules that bind to various classes of leukocytes.

Vascular cell adhesion molecules (VCAM-1) bind precisely to monocytes and T-lymphocytes.

The expression of these molecules tends to overlap within the site of the artery and eventually

develop atheroma [28]. Macrophages accumulate within regions of high stress, usually at the

shoulders of the fibrous plaque and secrete a multi-domain enzyme known as MMP-9. These

enzymes contribute to the vulnerability of the plaque by slowly degrading collagen type I fibers

and elastin, decreasing the tensile strength of the tissue allowing it to be more prone to rupture.

Its catalytic mechanism depends on zinc at the active center . The reason why macrophages tend

to lay in the regions of high stress within the fibrous cap is relatively unknown. Macrophages

are predominantly the cells at the immediate site of either rupture or superficial erosion of the

fibrous cap [29].

Many researchers have focused on the orientation of collagen fibers in both healthy and

pathological vessels because collagen is commonly recognized as the structure to provide

mechanical strengths to withstand high stresses that arteries experience during cardiac cycle. For

instance, in the media, two helically distributed bundles of collagen fibers are closely arranged in

the circumferential direction. However, collagen fibers are more dispersed in adventitia and

intima layers [27, 30-36]. Thus, investigation of gross fiber orientation leads to a better

understanding and predictability of the mechanical properties of the tissue [37]. Holzapfel et al.

measured mean fiber angles in the adventitia, media, and intima layer of thirteen human coronary arteries to be 67.0, 20.61, and 60.3 degrees, respectively [38-45] and 49, 7, and 0 degree in human external iliac artery [44]. Moreover, Deguchi et al. assessed detailed structure of collagen in the fibrous cap in mouse atherosclerotic plaques and they observed that thinning of the fibrous cap gives rise to the loss of collagen contents and the disorganization of collagen fibers. Furthermore, they found that mean fiber orientation in the fibrous cap to be  $14.3 \pm 2.6^\circ$  [30, 46-48]. As a result, considering fiber orientation will represent a more realistic situation that vulnerable plaques encounter. For soft biological tissues, Continuum based constitutive equations are used to describe the relations of the overall tissue mechanical properties with the corresponding internal structures. Without the proper constitutive relations, governing equations describing the system's mechanics are not solvable. Furthermore, constitutive equations are critical tool for understanding the mechanism of failure under either physiological or pathological conditions.

*f. Medical Imaging Modalities Used For Plaque Evaluation (IVUS / microCT / Angiography)*

*Intravascular Ultrasound Imaging Protocol*

Intravascular ultrasound (IVUS) is a minimally invasive, catheter-based imaging technique for the evaluation of coronary plaque, lumen, and vessel dimensions. IVUS can measure lumen, plaque, and vessel area as well as morphological features of the vessel. Detecting both unstable fibrous cap with thickness equal or less than 65  $\mu\text{m}$  and microscopic calcifications within the fibrous cap would require imaging resolution beyond the scope of IVUS-VH. With the development of more advanced micro-CT imaging modality, all vulnerable plaque components can be captured in details. Especially, it is capable of pinpointing the exact location of microcalcifications in the fibrous cap for better prediction of the potential site of rupture.

Currently, no angiography compatible micro-CT probe available on the market can be found and all micro-CT images can only be performed on post-mortem samples.

*g. Current Computational Models For Coronary VP Studies.*

Up to date, several 3D multicomponent medical imaging based FSI computational models proposed by researches to perform and investigate flow and plaque stress/strain analysis, and to identify critical stress/strain conditions, which may be related to plaque rupture. However, most of these simulations used isotropic solid material models to represent actual vessel conditions due to the lack of accurate vessel material properties in the literature (15-18). While plaque morphology and related imaging technologies are important for identifying vulnerable plaques and providing critical information about plaque components, mechanical forces also play an important role in plaque progression and rupture process. Both mechanical forces (rupture triggers) and plaque structures are key factors in the rupture process and should be considered in an integrated way (19). Tang et al. studied IVUS-based 3D Fluid-Structure Interaction models with anisotropic vessel properties for human coronary plaque. They claimed that an anisotropic material model used for the vessel for more realistic modeling, more accurate computational flow, and better stress/strain predictions (20). However, only few studies can be found to integrate orientation of fiber angles in both healthy and pathological vessel wall while performing 3D multicomponent FSI simulations. Holzapfel et al. measured anisotropic mechanical properties for tissue components of human atherosclerotic plaques (21). They also measured layer-specific mechanical properties such as fiber angles in three arterial layers of human coronary arteries (22).

*h. FSI Approaches: Biofluids Laboratory Approach for VP*



Patient specific dynamical analysis between fluid and solid structures in pathological coronary vulnerable plaques (VP) involves several stages. Initially, a three-dimensional reconstruction is rendered from the imaging data source. Boundaries of the reconstruction are considered to optimize proper observation of the vessel pathology. Using Mimics image reconstruction software [10], we reconstruct the anatomical components of the vessel, such as the outer wall, lumen, atheroma lipid core, atheroma fibrous cap, macrocalcifications and microcalcifications (micro-Ca). In a normal coronary vessel, the outer wall is a reinforced, yet highly elastic fibrous material that surrounds the blood carrying lumen. Atheroma plaque formation will produce a gradual stenosis of the lumen over time. The 3D vessel geometry is decomposed into a computational mesh prior to FSI simulation in ADINA. Material properties for fluid and solid components of the VP geometry along with details of FSI simulation runtime are further described below. The quantitative information acquired from FSI through this approach can be used to provide quantitative information to gain an understanding of flow disturbances and fibrous cap stress patterns in VP pathology.

### **Methods:**

*Patient data acquisition using micro-CT (Developed and Implemented by Weinbaum Group from City College of New York).*

Formalin-fixed human coronary segments (25 mm in length, n = 24) obtained at autopsy were scanned by using the eXplore SP Pre-Clinical Specimen Micro-CT acquisition and analysis system (GE Healthcare, Piscataway, NJ). For image acquisition, 720 consecutive X-ray projections were acquired at 60kVp and 167 $\mu$ A. Power settings were chosen to increase the contrast between soft tissue, atheroma's lipid content and the mineralized tissue. The image magnification was set to 7  $\mu$ m isotropic pixel size and 5 exposures were averaged to reduce noise

in each projection. Prior to acquisition, a bright and dark flat field correction was performed at the same power settings.

X-Ray projections were converted into axial images using a modified back-projection reconstruction algorithm included in the eXplore SP Micro-CT system. Reconstruction parameters for artifact correction, Ring Artifact Correction and Beam Hardening Correction were kept constant in all samples for calibration and standardization purposes. The set of axial images for a sample consists of approximately 3500 2D slices with 7  $\mu\text{m}$  isotropic voxel resolution and 16 bit gray levels.

Mineral density was calibrated by using a phantom containing hydroxyapatite, air, and water. Density-calibrated images were segmented by using a global threshold method built-in Mimics visualization and analysis software (Materialise; Version 2.1.2). The presence of mineral, soft tissue, lipid, and air in the vessels was distinguished by the high sensitivity of the system to the different densities of each of these compartments. Mineralized tissue particles were recognized in each volume of interest, and isosurfaces of microcalcifications in the fibrous cap of the atherosclerotic lesion were rendered using the Mimics software [20].

#### *Reconstruction from Micro-CT*

Micro-CT imaging data described above was used to reconstruct this non-ruptured VP geometry. Layered masks were automatically segmented in Mimics software as previously described [23]. The coronary specimen studied had an inlet diameter of 3.08 mm, whereas the region of maximal stenosis has a diameter of 2.23 mm producing 47.6% cross-sectional stenosis, considered asymptomatic under most clinical scenarios. The region of maximal stenosis also corresponded to the primary location of the fibroatheroma. Three-dimensional structures for the vessel wall,

micro-Ca, lipid pools, fibrous cap, lumen boundary, and micro-Ca were subsequently rendered in Mimics with further iterative smoothing. This process allowed for the generation of a cohesive three-dimensional image set which portrayed the pathological details of each particular case in proper anatomical relationship to surrounding vessel features (Figure 19). The model is shown in Figure 19A-D. Micro-Ca landmarks are presented in relation to the 3D geometry are pointed out in Figure 19E-F. The reconstruction followed these steps: Anatomical features representing pathology of the vessel were recreated using 35 $\mu$ m and 7 $\mu$ m resolution CT image libraries of the same vessel specimen. The 35 $\mu$ m cross sections were sufficient to reconstruct the vessel wall, lumen, subintimal lipid pools, and large calcification. However, reconstruction of the fibrous cap and micro-Ca required use of the 7 $\mu$ m high-resolution CT image slices. Three micro-Ca of radius of 21, 26 and 30  $\mu$ m were reconstructed from the fibrous cap. The fibrous cap itself had an almost uniform thickness of approx. 300  $\mu$ m.

#### *Patient Data Acquisition Using Intravascular Ultrasound.*

Intravascular ultrasound (IVUS) is a minimally invasive, catheter-based imaging technique for the evaluation of coronary plaque, lumen, and vessel dimensions. IVUS can measure lumen, plaque, and vessel area as well as morphological features of the vessel. Calcified regions and dense fibrous appear bright and homogenous due to a good reflection of the ultrasound energy. IVUS has the ability to localize plaques and quantify plaque burden and its axial resolution is ~150  $\mu$ m, when using 20-MHz phase-array, 2.9-F catheter (Eagle Eye; Volcano Corporation, Rancho Cordova, CA, USA) as in these cases. Virtual histology (VH) is an advanced IVUS imaging technique (IVUS-VH) for assessing tissue characterization of plaques using spectral analysis of the radiofrequency (RF) data. The VH technique provides quantitative assessment of

the wall morphology and plaque components. IVUS-VH, which is based on spectral and amplitude analysis of the IVUS backscatter signals, allows reliable characterization of the mechanical and acoustic properties of vascular tissues [49-51]. The raw signals from reflection of ultrasound waves are transduced into a color-coded representation of plaque characteristics.

### *Reconstruction from IVUS*

A dedicated application written in Matlab (MathWorks Inc., Natick, MA, USA) was developed in the framework of the current study and used to evaluate the plaque area and its component characteristics based on the IVUS-VH images. A few morphological operations have been applied to obtain smoother IVUS-VH images and a simple volume reconstruction of the entire lesion. Small regions below the spatial resolution of IVUS-VH were ignored, and connected components of the same tissue were grouped together. An edge detector generated boundary lines for the various plaque components, and automatic labeling defined the region of each tissue. The lumen and the media contours were used to set the vessel wall thickness. A 3D mesh of the arterial anatomy and the complex plaque geometry were reconstructed by collecting the IVUS-VH cross-section images along the path of the center of the catheter. The segmented contours were imported to Avizo (version 6.1.1, VSG, France) and a surface was generated for each tissue. The Avizo software package allowed us to thoroughly examine the generated surface by enabling a high-end rendering. Our 3D geometry included both the fluid domain and the solid domain. The solid domain consisted of the fibrotic artery wall, calcium, necrotic core and media (Fig. 2). For computational load reduction, the model was simplified and each tissue surface was reduced from >100,000 to 500 faces. In this study, three IVUS based patient-specific coronary plaques with various fibrous cap thicknesses were reconstructed and incorporated into the analysis. Specifically, the fibrous cap for Case I was varied from 400  $\mu\text{m}$  to 150  $\mu\text{m}$ , and Case II

varied from 250  $\mu\text{m}$  to 150  $\mu\text{m}$ , which can be visualized with current IVUS resolution. For Case III, we artificially incorporated a very thin fibrous cap with a uniform thickness of 65  $\mu\text{m}$ , which is the limit of unstable plaque, to study the effect of fibrous cap thickness on stress/strain distributions. As depicted in Figure 15a, the reconstructed coronary vessel (Case I) is composed of the vessel wall shown in silver, necrotic core in red, and the macrocalcification in white.

#### *Hypertensive and microcalcified cases.*

In order to examine the contribution of a calcified spot on vessels' stress variation, a three-dimensional theoretical model of a rigid spherical inclusion with 10 $\mu\text{m}$  diameter was placed downstream the plaque shoulder within the thin region of the fibrous cap [19, 20]. Both global and local von Mises stress distributions were compared, while local stress measures the stress value at the same background in the fibrous cap with or without micro-Ca embedded. Hypertension was represented by consistently elevating the physiologically normal pressure by 25% for the entire cardiac cycle. Peak systolic pressure was increased from 122 mmHg in normal case to 152.5 mmHg in hypertensive case.

### **Material Models**

#### *Isotropic material models for vessel and fibrous cap*

Three-dimensional non-linear modified Mooney-Rivlin (M-R) isotropic material model was used to characterize the material property of the coronary vessel including arterial wall, necrotic core, and calcification. The isochoric elastic response of the strain energy function (per unit volume),  $\bar{\psi}$ , for the isotropic M-R model, without the hydrostatic pressure term  $-pI$ , is shown in equations (1) & (2).

$$\bar{\psi} = C_1(I_1 - 3) + C_2(I_2 - 3) + D_1[\exp(D_2(I_1 - 3)) - 1] \quad (1)$$

$$I_1 = \text{tr}(\mathbf{C}_{ij}), \quad I_2 = \frac{1}{2}[I_1^2 - \text{tr}(\mathbf{C}_{ij}^2)], \quad J = \lambda_1 \lambda_2 \lambda_3 = \det \mathbf{F} \quad (2)$$

$\lambda_\alpha$  ( $\alpha = 1, 2, 3$ ) Principle Stretches

In an incompressible material formulation, the arbitrary hydrostatic pressure work,  $-pI$ , commonly known as reaction stresses, is always considered in the stress representation. Scalar  $p$  is chosen to maintain incompressibility, which means  $\det \mathbf{F}$  is equal to 1, and is separately interpolated. Where  $I_1$  and  $I_2$  are the first and second strain invariant of the strain tensor, isotropic strain energy function shown in equation (1) can be used to calculate the second Piola-Kirchhoff stress tensor,  $\mathbf{S}$ , by taking the derivative of the function with respect to Right Cauchy-Green tensor,  $\mathbf{C}$ . With the calculated stress tensor, the Cauchy stress obtained through the relation  $\boldsymbol{\sigma} = \mathbf{F}\mathbf{S}\mathbf{F}^T$ , where  $\mathbf{F}$  is the deformation gradient can be used to fit the experimental data in order to generate material constants [31]. The material constants,  $C_i$  and  $D_i$ , are taken from previous experiment [52, 53]. All values used in the simulations can be found in Table 1.

Model	$C_1$ (kPa)	$D_1$ (kPa)	$D_2$	$k_1$ (kPa)	$k_2$	Fiber Angle
Vessel Wall	28.14	1.31	11.5	—	—	—
Necrotic Core	0.5	0.5	0.5	—	—	—
Calcification	281.4	13.1	11.5	—	—	—
Anisotropic Fibrous Tissue	8.29	0.907	3.1	8.824	3.7	$5^\circ, 65^\circ, 85^\circ$

**Table 1: Material Parameters determined for the material model used in our simulations**

### *Anisotropic material model for fibrous cap*

Anisotropic material model was applied to investigate the high degree of anisotropy of the fibrous cap material. Anisotropic strain energy function,  $\bar{\psi}$ , (per unit volume; without the hydrostatic pressure term  $-pI$ ) is shown in equations (3) & (4).

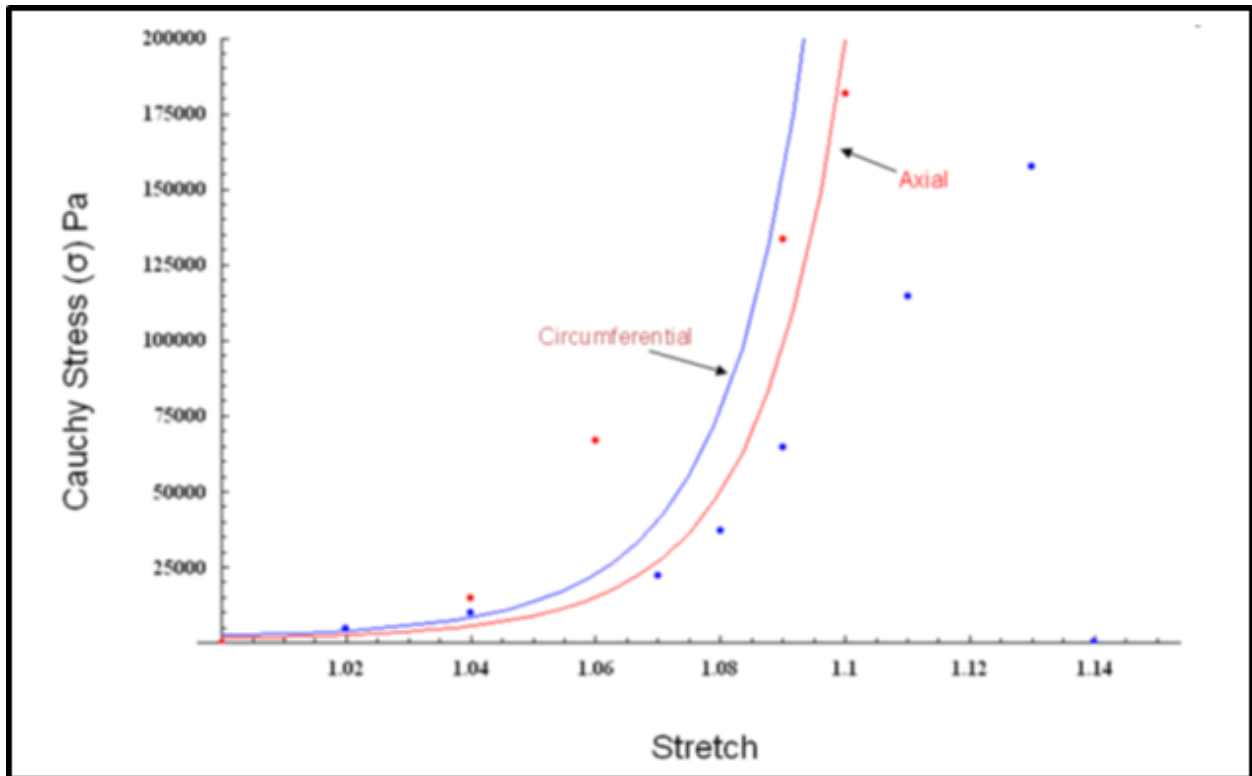
$$\bar{\psi} = C_1(I_1 - 3) + D_1(e^{D_2(I_1-3)} - 1) + \frac{k_1}{2k_2}(e^{k_2(I_4-1)^2-1}) \quad (3)$$

$$I_1 = tr(C_{ij}) \quad , \quad I_4 = C_{ij}(n_a)_i(n_a)_j \quad (4)$$

This model is the combination of the Holzapfel anisotropic material formulations, which describe the arterial wall as fiber-reinforced tissues, with a Fung type of material [54]. Where  $I_4$  is the Pseudo-invariant of the strain tensor, incorporating the fiber angle into the function and  $k_1$  and  $k_2$  are material constants that are specifically associated with anisotropic characteristics.  $n_a$  is the angle between the collagen fiber and the circumferential direction in the vessel so it acts as a geometrical parameter [38, 53, 55](Detailed mathematical derivation can be found in Appendix). Various fiber angles, for example  $5^\circ$ ,  $65^\circ$ , and  $85^\circ$ , were used to represent both healthy and diseased fiber directions. 65 degree fiber angle was expected to behave as diseased condition according to the literature [38]. As shown in Figure 15c, three-dimensional representation of the axial and circumferential Cauchy stress over corresponding stretches for fibrous cap with 65 degree fiber angle was plotted to observe the stress behavior under both small and large strain conditions.

Relevant tissue material constants can be determined by curve fitting data from Holzapfel, G.A et al [56]paper. All values are listed in Table 1. However, there naturally exists so much difference on the mechanical response of various vessels under loading such as the external iliac artery and coronaries [53, 56-58] and even the predicted stress values described by available

material models introduced by different research groups also slightly differ, such as shown in Figure 4[38]. Moreover, Deguchi *et al.* assessed detailed structure of collagen in the fibrous cap in mouse atherosclerotic plaques and they observed that thinning of the fibrous cap gives rise to the loss of collagen contents and the disorganization of collagen fibers. Furthermore, they found that mean fiber orientation in the fibrous cap to be  $14.3 \pm 2.6^\circ$  [46] As a result, considering fiber orientation will represent a more realistic situation that vulnerable plaques encounter.





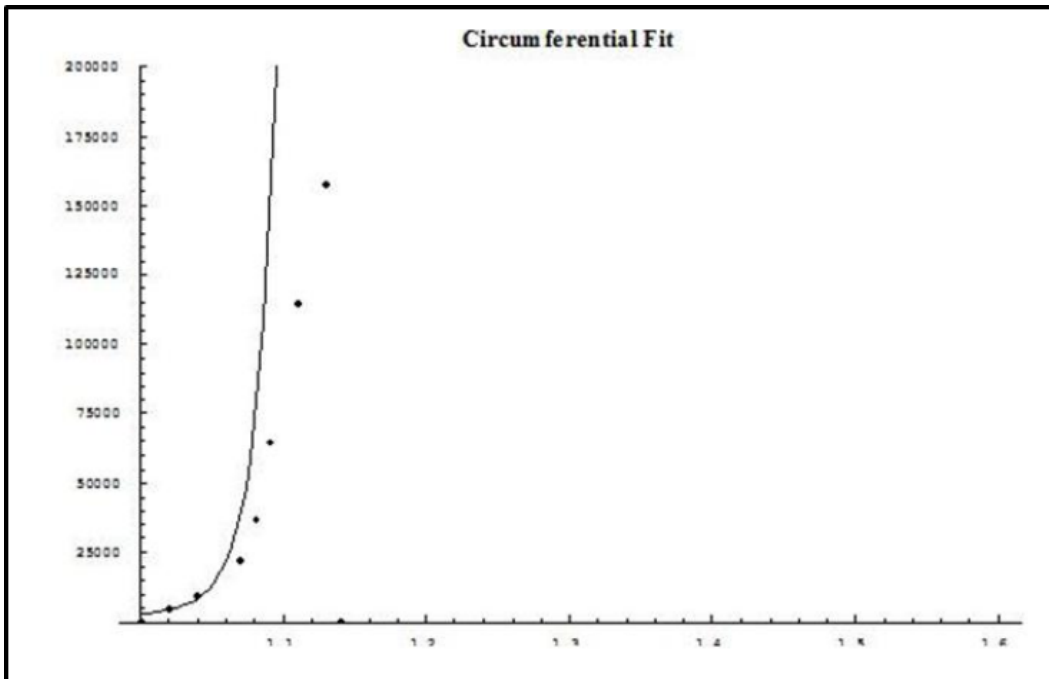
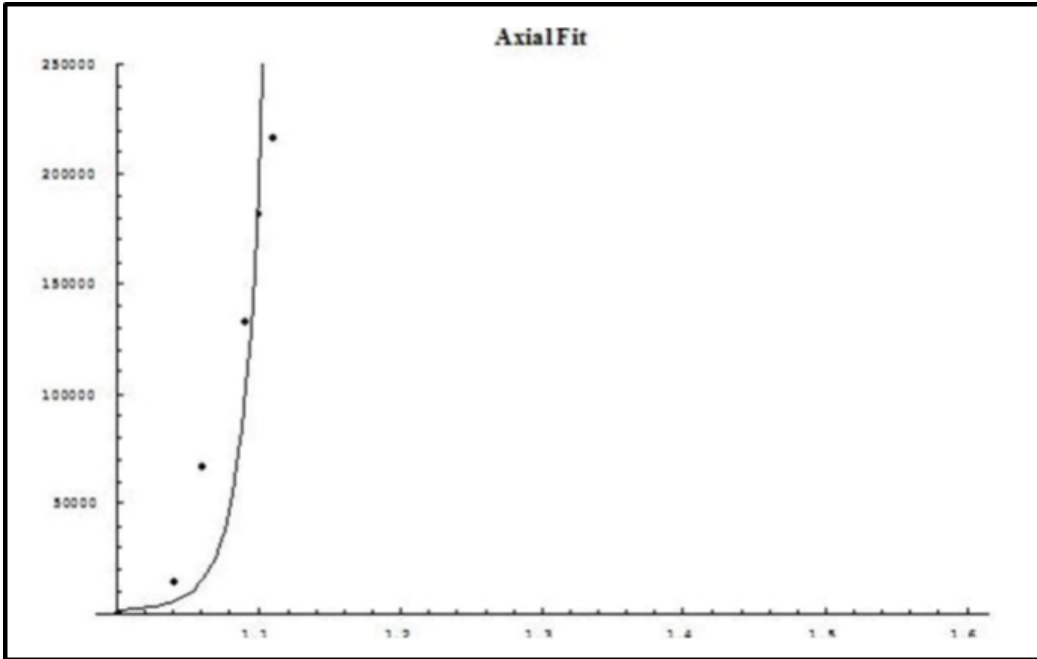


**Figure 3: A: Stress-Stretch fitting curves generated from anisotropic Mooney-Rivlin model and experimental data of fibrous cap from human iliac artery. B & C: Stress-strain curves fitted with anisotropic material model separated by axial and circumferential directions.**

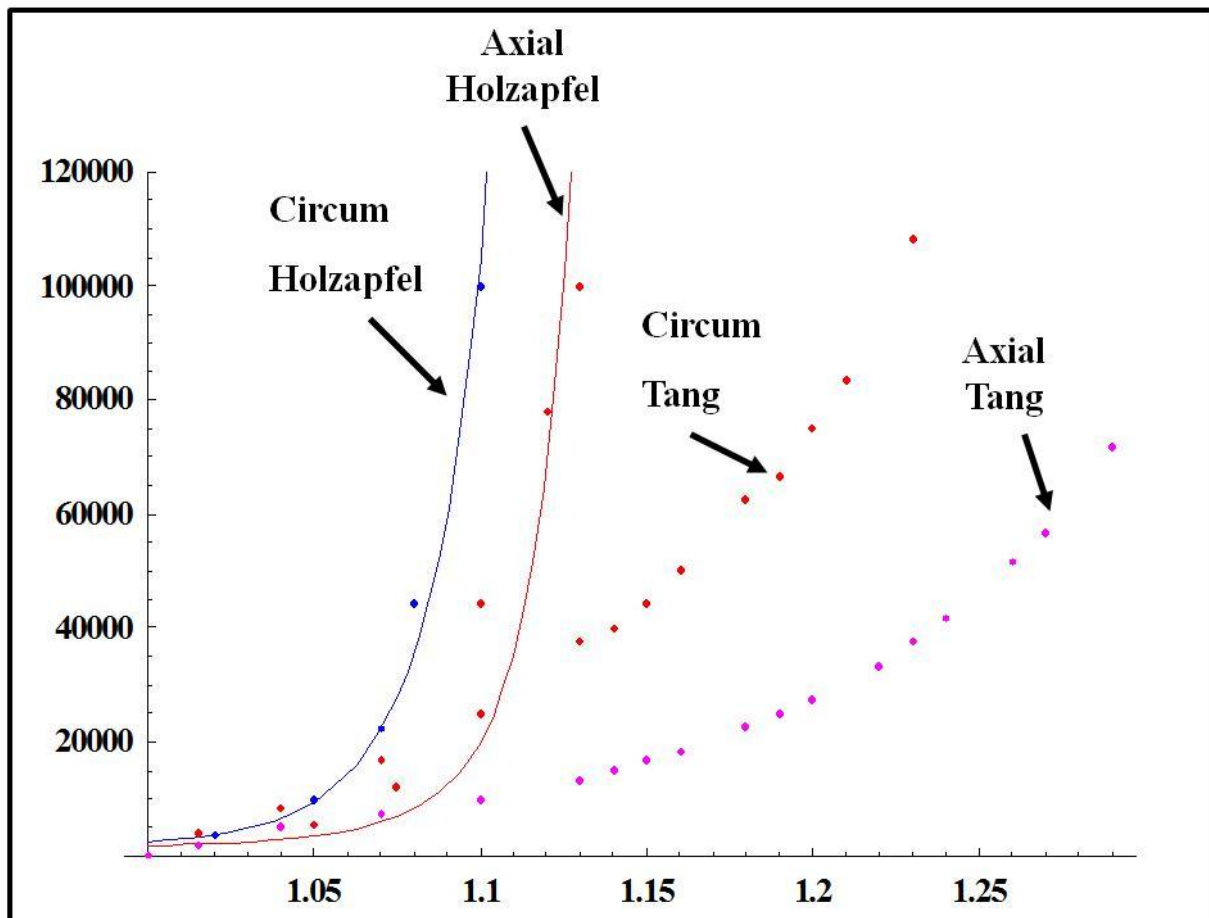


**Figure 4: Stress-strain curves generated from Mooney-Rivlin anisotropic material model tried to fit the experimental data of human coronary cadaver sample taken from different research groups. It actually shows the variation on the material data obtained for the same type of vessel from different groups. However, the trend, which vessel as soft tissue is much stiffer in the circumferential than axial direction and it closely assembles the physiological conditions that vessels undergo much larger expansions than stretching.**

### *FSI Methodology:*

Three-dimensional FSI model was created from patient specific imaging data set to assess blood flow and stress/strain distributions on the wall in the vessel. Blood flow was assumed to be laminar, Newtonian, viscous, and incompressible. The governing equations were the Navier-Stokes equations with arbitrary Lagrangian-Eulerian formulation. Physiologically, there is a 72° phase lag existed between the occurrence of coronary peak pressure and flow (Figure 15b) due to the fact that coronary arteries receive the maximal flow during diastole [1]. Pressure condition was applied at the outlet of the vessel and mean flow velocity waveform for the complete cardiac cycle was assigned at the inlet as shown in Figure 15b. In order to accurately examine the impact brought by the flow on the interacting vessel wall, parabolic velocity profile corresponding to specific geometry was calculated and applied at the inlet. Furthermore, physiological boundary waveforms measured from patients taken from the literature were fitted with an in-house Matlab to find proper function describing them and accurately incorporated into the simulations. Matlab code can be found in the Appendix. For the vessel wall, both inlet and outlet were only allowed to move in axial direction [54] and 10% pre-stretching was applied to the vessel [59-62]. Natural traction equilibrium and no-slip conditions were assumed to all interfaces. Moreover, displacements that fluid and solid undergo should be compatible and stresses that fluid and solid withhold are equal to each other [54, 55]. Blood density and viscosity used in the simulations were assumed to be  $1.050\text{g}\cdot\text{cm}^{-3}$  and 3.5cP respectively. For FSI, both solid and fluid domains of the VP model were introduced in ADINA (ADINA R&D Inc., Watertown, MA) and a first order finite-element scheme was used to solve the set of motion and fluid equations [19, 54, 55].

### *Grid Independency Studies and Computational Capacity*

Mesh was locally refined at the boundaries of two distinct components of plaque sample. Computational mesh size was analyzed and finally chosen for the simulations until only 4% of solution difference was achieved. A 1  $\mu\text{m}$  elemental size was used to mesh the embedded micro-Ca in order to capture the finer details of stress distribution around them in the fibrous cap [55]. The final luminal blood flow domain of the four patient specific cases studied contains 17,367, 34,781, 48,984, and 82,319 elements in Case I, II, III, and IV, respectively. The corresponding solid domain, which was composed of the vessel wall, necrotic core, macrocalcification, and embedded micro-Ca, has 184,244, 231,605, 196,185, and 816,529 elements in Case I to IV. Initially, the domain was pressurized for 1 second to reach physiological pressure of  $\sim 90$  mmHg. Then, two complete cardiac cycle of 100 time-step for each cycle (initial  $\Delta t = 0.01$  sec) were performed. Automatic time stepping (ATS) control was used for achieving optimized converged solution by subdividing the time step until it reaches convergence [54, 55]. The FSI simulations were conducted on a high capacity computing cluster composed of four quad core Xeon CPUs with a shared memory of 64 GB RAM. The CPU time for each simulation was approximately four days for the finest grid. A direct numerical approach was used for the integration of the highly non-linear coupled system of equations.

Results

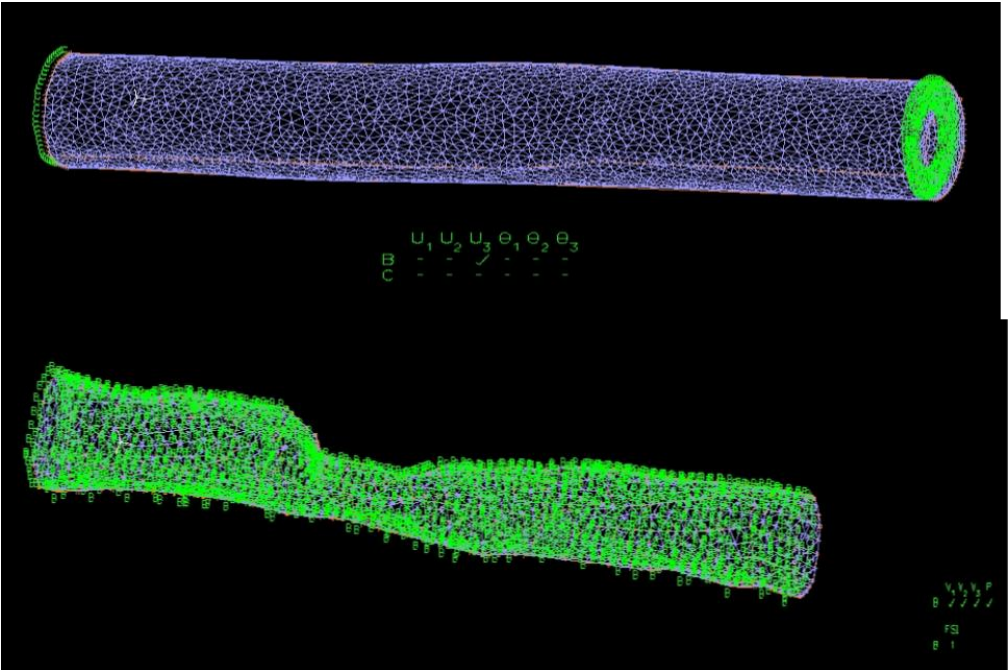
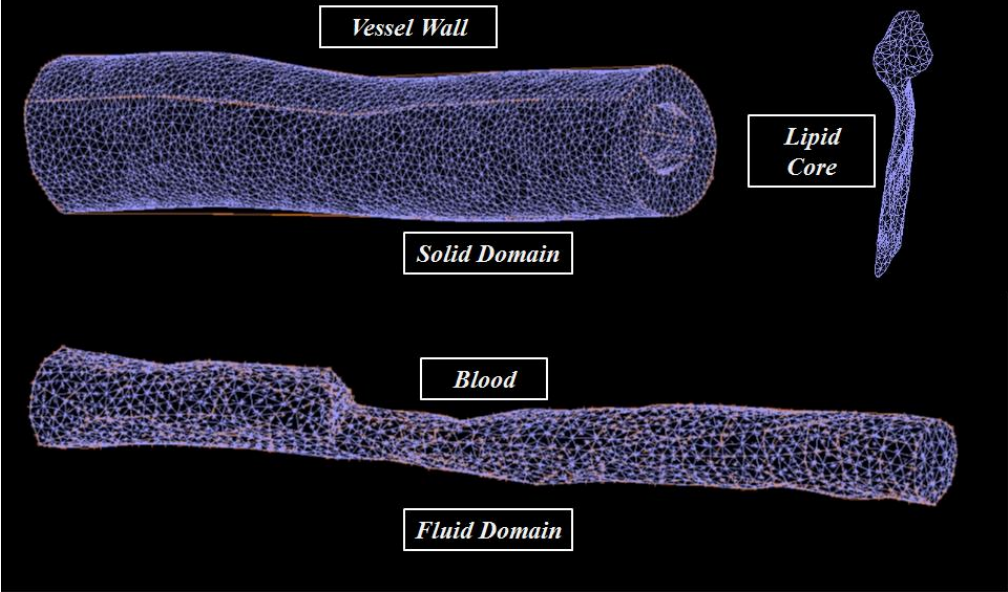


**Figure5: Coronary geometry meshed in ADINA, solid and fluid domains are shown. Lower figure shows the boundary conditions, fixed at one end of the solid domain and free to move in the other end. For the fluid domain, all faces that are interacting with the solid domain are assigned with No-slip and FSI boundary conditions.**

*General Hemodynamics for Geometries with Various:*

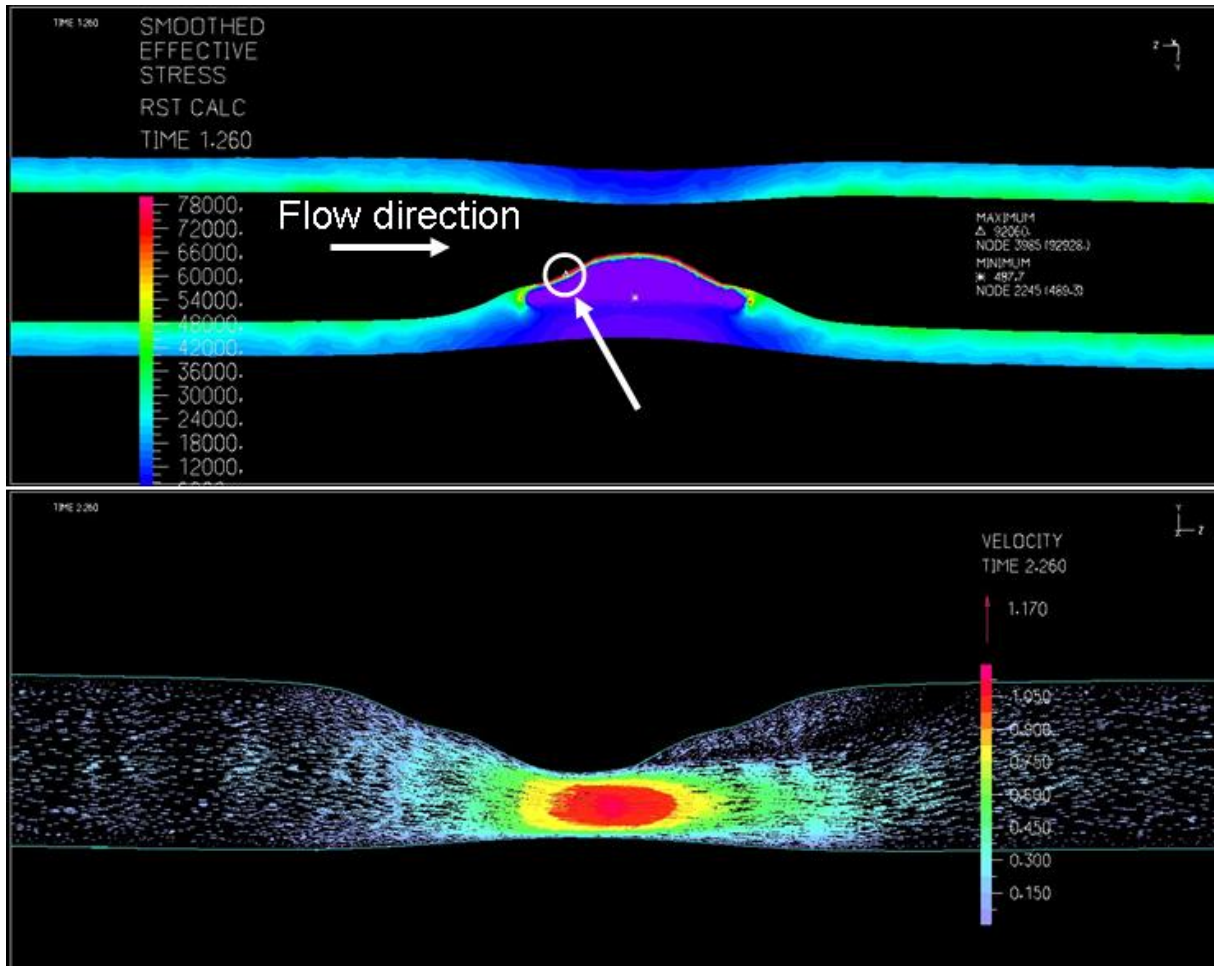


**Figure6. Stress distribution, peak stress and blood velocity profile. Figure 5A shows the band plot of smoothed effective stress (von Mises stress) that represents the FSI model of isotropic coronary artery with lipid core. The peak stress at peak systole is 92,060 Pa. The lower image shows the flow field of the pathological coronary artery. Peak stress is shown on graph to be occurred at the surface of thin fibrous cap on upstream.**

*Prestretch:*

Initially three stretching case studies were performed to obtain the optimum stretching percentage for the geometry (Figure 4&5). The stretching percentages studied were: 10%, 15% and 20%. Each case produced the following peak stresses, which are listed in Table 2 shown below with minimum in 20% stretch. Apparently, it reveals that axially stretching should be taken into account when we try to reconstruct and mimic more physiological behaviors of the vessels.

<b>Model</b>	<b>Peak Stress</b>
Isotropic, 10% Axial Stretch	95777 Pa
Isotropic, 15% Axial Stretch	92460 Pa
Isotropic, 20% Axial Stretch	88710 Pa

**Table 2: Influence of different prestretching on peak stress calculated.**

### **Vessel Only Anisotropic Simulations-*Severe Stenosis***

Vessel only anisotropic simulations with higher stretches were applied in order to resolve irregular bending of the vessel in the previous cases. Anisotropic model with 5/185 degree was treated as our baseline. We performed 20%, 25%, and 30% stretching as Tang *et al* used in their studies of carotid artery [52, 61] and observed if the unrealistic bending was still present.

Relevant stresses corresponding to each case have been included in the Table 3&4 below.

**Table3. Axial Pre-stretch (Units: Stress, Pa)**

Stretch	20%	25%	30%
Effective Max Stress	199499	196964	205904
Effective Min Stress	2715	3399	2610
Smoothed Max Stress	111129	106686	109004
Smoothed Min Stress	3688	4049	3285
Bending	Yes	Slightly	No

According to the observation, 30% pre-stretch was then incorporated into the preliminary parametric study of fiber orientations of both idealized normal and pathological human coronary arteries.

### **Vessel Only Anisotropic Simulations: Mild Stenosis**

Same methodology as in previously performed severe case was applied. Vessel only anisotropic simulations with various stretches were applied in order to resolve irregular bending of the vessel. Anisotropic model with 5/185 degree was treated as our baseline. We performed 25%, 30%, and 35% stretching as Tang *et al* used in their studies of carotid artery and observed if the unrealistic bending is still present. Stresses corresponding to each case have been included in the table below.



**Table 4: Axial Pre-stretch In Order To Eliminate Irregular Bending**

Stretch	25%	30%	35%
Smoothed Max Stress	210164	208043	228245
Smoothed Min Stress	210164	6390	6882
Bending	Yes	Yes	Small (Negligible)

*Different Collagen Fiber Orientations:*

Unfortunately, both 25% and 30% pre-stretching were unable to prevent the occurrence of irregular bending. Although visible bending was observed in 35% pre-stretching condition as well, it has been considered to be negligible. Even higher stretching is required in this mild case than previous severe one might be caused by the much finer mesh used. All stresses checked are listed in the table below.

**Table 5: Stresses at Systole**

Pre-stretch	Fiber Angles (Deg)	5	90	65
35%	Smoothed Max Stress (Pa)	228245 (100%)	222970 (98%)	297012 (130%)

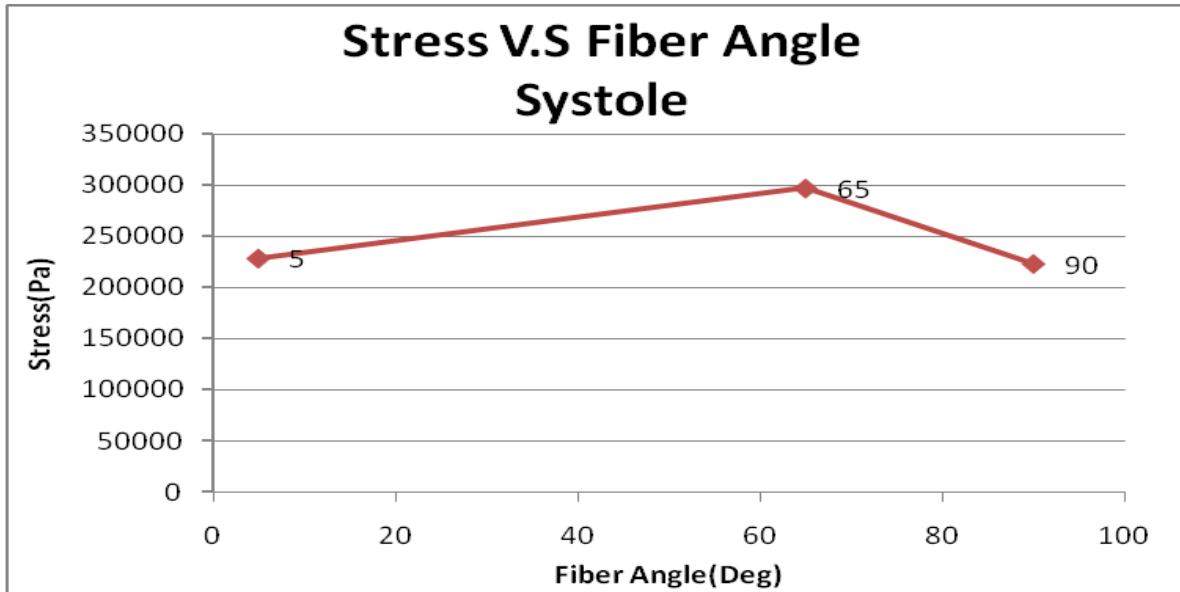


**Figure 7: This figure shows the pathological fiber angle (65 Deg) increases the maximum stress at systolic pressure.**

**Table 6: Stresses at diastole for healthy fiber angles (5, 90 Deg) and also pathological fiber angle (65 Deg)**

Pre-stretch	Fiber Angles (Deg)	5	90	65
35%	Smoothed Max Stress (Pa)	168386 (100%)	164918 (98%)	212757 (126%)

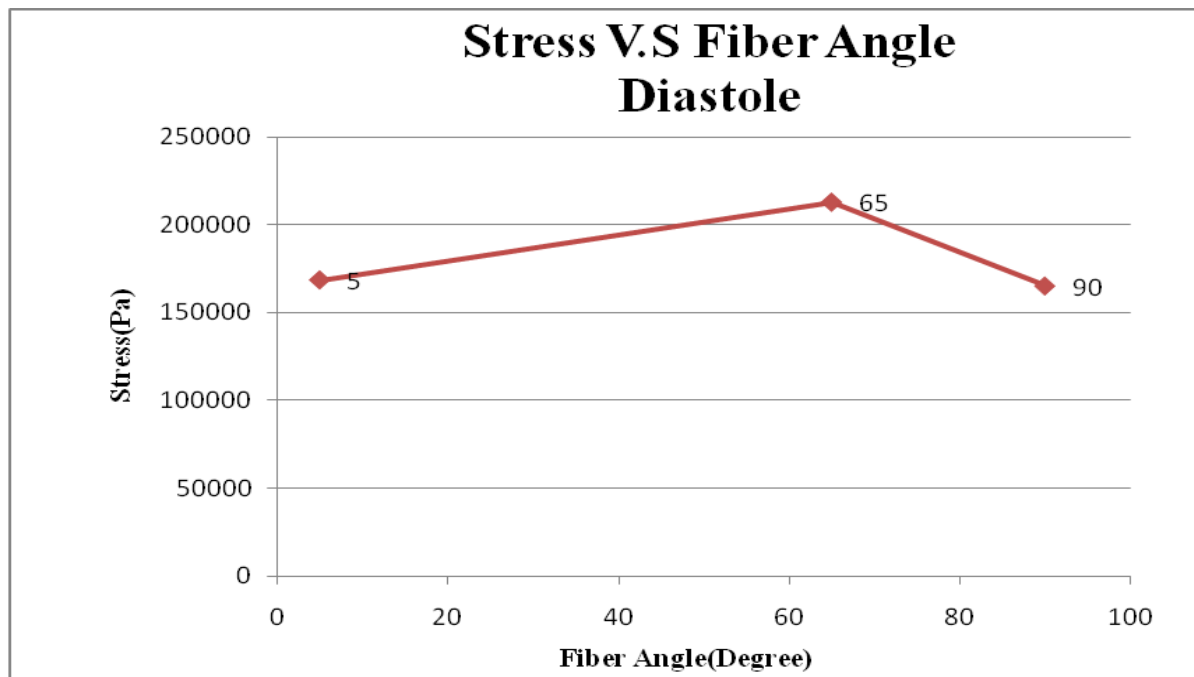


**Figure 8: This figure shows the pathological fiber angle (65 Deg) increases the maximum stress at diastolic pressure.**

## Effects of Fiber Angles- *Fluid-Structure-Interaction ( FSI) Studies*

Maximum stresses are always higher in the range of 60~70 degree fiber angles, which are considered to be pathological fibers [38]. Particularly, approximate 25%~35% increase of maximum stress could be found when 65 degree fiber angle was used in comparison to 5, 45, and 90 degree healthy fiber angles as depicted in Figure 7&8 during both systole and diastole.

### Mild Case

**Table 7 ( Stresses associated with different angles and pre-stretches)**

Pre-stretch	Fiber Angle (Degree)	5	90	65(Pathological)
35%	Smoothed Max Stress (Pa)	<b>168386</b> <b>(100%)</b>	164918 (98%)	<b>212757</b> <b>(126%)</b>
30%	Smoothed Max Stress (Pa)	<b>208043</b> <b>(100%)</b>		<b>272657</b> <b>(131%)</b>
25%	Smoothed Max Stress (Pa)	<b>210164</b> <b>(100%)</b>		<b>264671</b> <b>(125%)</b>

### Severe Case

Pre-stretch	Fiber Angle (Degree)	5	90	65(Pathological)
30%	Smoothed Max Stress	<b>109004</b> <b>(100%)</b>	109289 (100%)	<b>147370</b> <b>(135%)</b>

## FSI simulations: Mild Stenosis

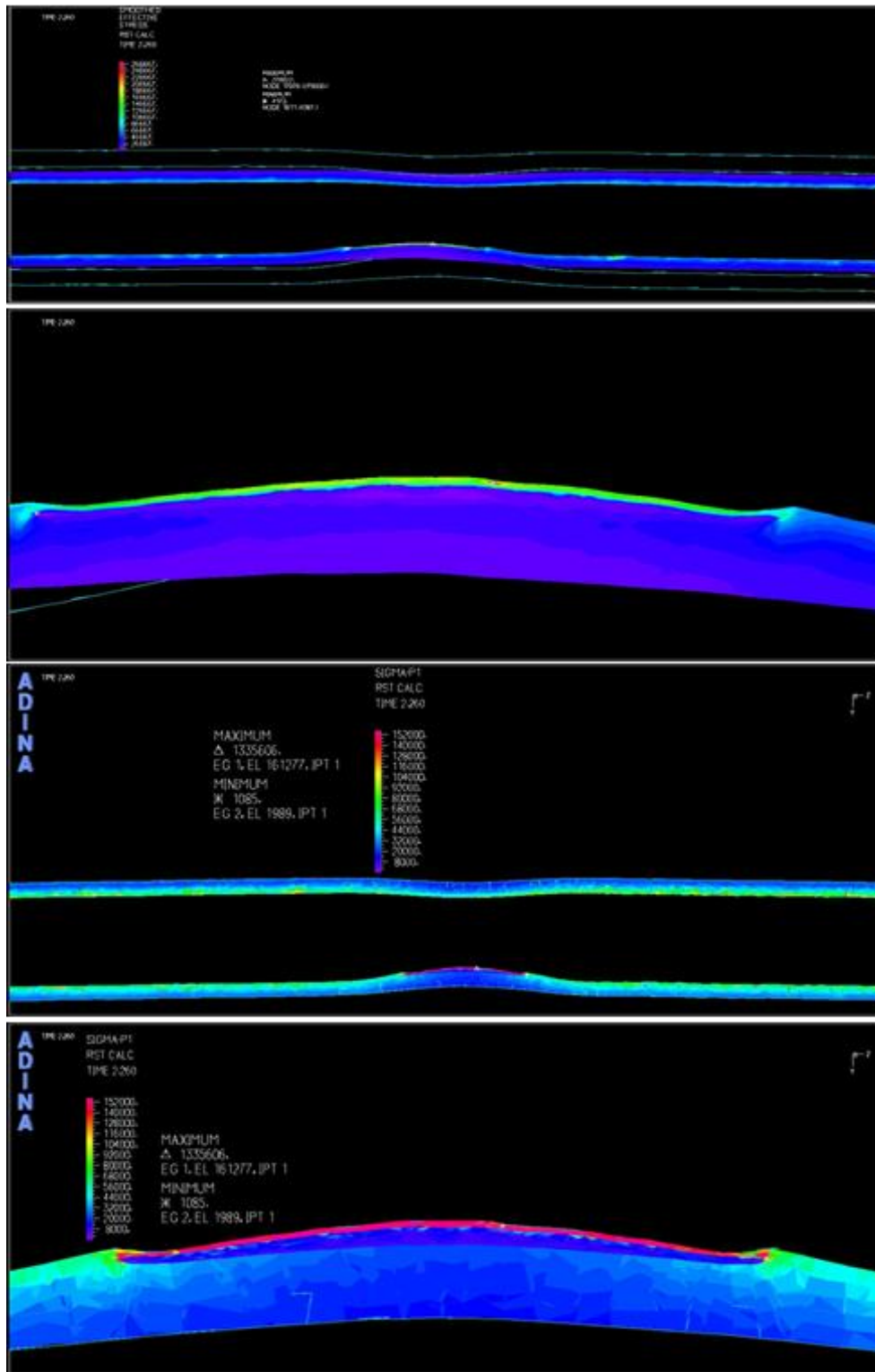
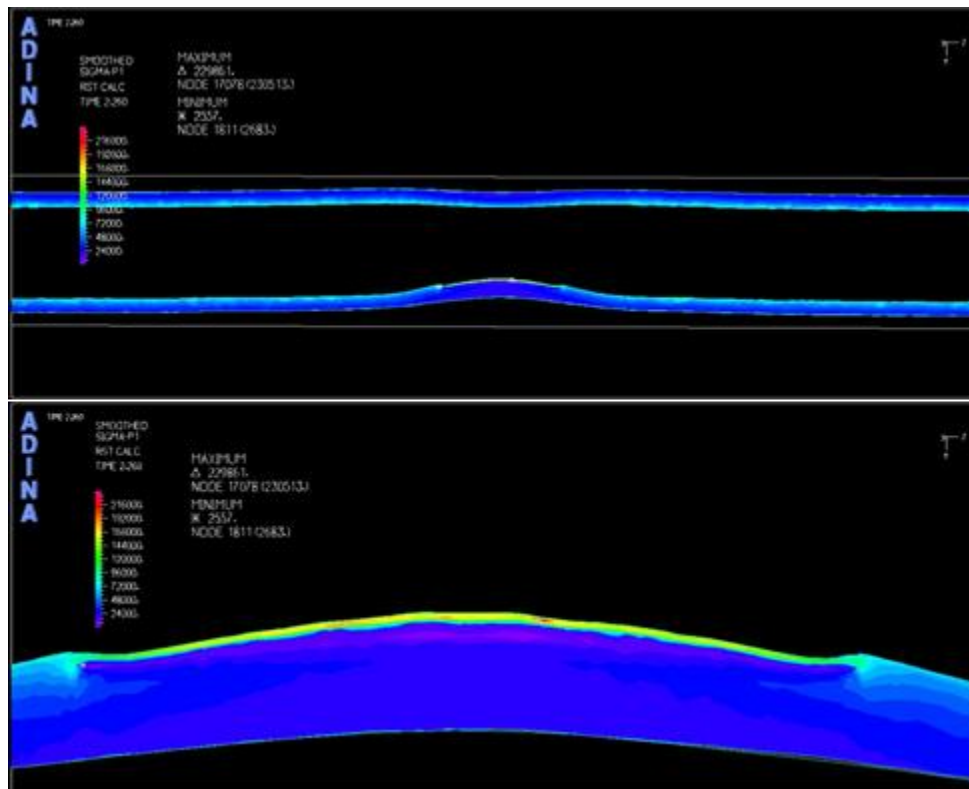


Figure 9: (5 degree fiber angle): Smoothed effective stress and principal axial stress distributions. Zoomed in at stenosis region to identify maximum values.



**Figure 10: (65 degree fiber angle) principal axial stress distribution and zoomed in at stenosis region at peak systole. In addition, velocity distribution is shown as well.**

**Table 8: Stresses extracted from FSI simulation at different fiber angles (Pa).**

Pre-stretch	Fiber Angle (Degree)	5	65(Pathological)
35%	Smoothed Max Stress	<b>228938 (100%)</b>	<b>297842 (130%)</b>

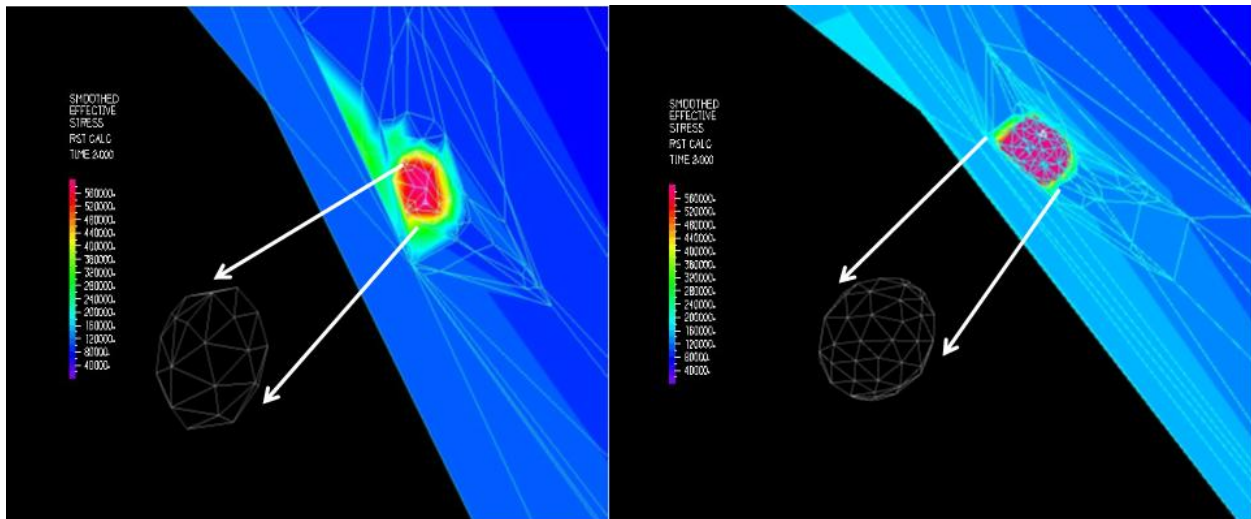
### **Summary of the parametric study of fiber orientations**

In this parametric study, we examined the effects of fiber angles on critical stress distribution. Fiber angles observed in both healthy and pathological human coronary arteries were considered and FSI stimulations of both severe and mild case were performed. In the anisotropic simulations, 30% - 35% pre-stretch were applied to severely and mildly stenosed vessels respectively in order to eliminate irregular bending. According to the literature reviewed [36, 37, 53, 63-66], 5, 50, and 90 degree were particularly chosen to represent fiber orientations in healthy vessels. Moreover, fiber angles will be in the range of 64.33 ~ 70.95 Deg in pathological coronary arteries based on the in vivo histological data found by Holzaphel and collaborators [38]. Initially, we used 5, 45, 50, and 90 degree as normal fibers and 65, 68, and 72 as pathological fibers in severely stenosed case. We surprisingly found that maximum stresses (Table 6&7; Figure 7&8) were always higher when 65,68 and 72 degrees were implemented , which were found to be associated with diseased vessels and also the assumption of normal fiber angles 5, 50, and 90-degree seem to be reasonable because the peak stresses of these cases are basically the same. Moreover, we also observed that there was always approximate 25-35% maximum stress increase when 65 degree angle was used. In order to further verify this trend, we performed FSI simulations with mild stenosis at 5 and 65 degree fiber angles. As summarized, stress elevation was still consistent with the trend that has been previously observed.

*Micro-Ca Size and Shape:*

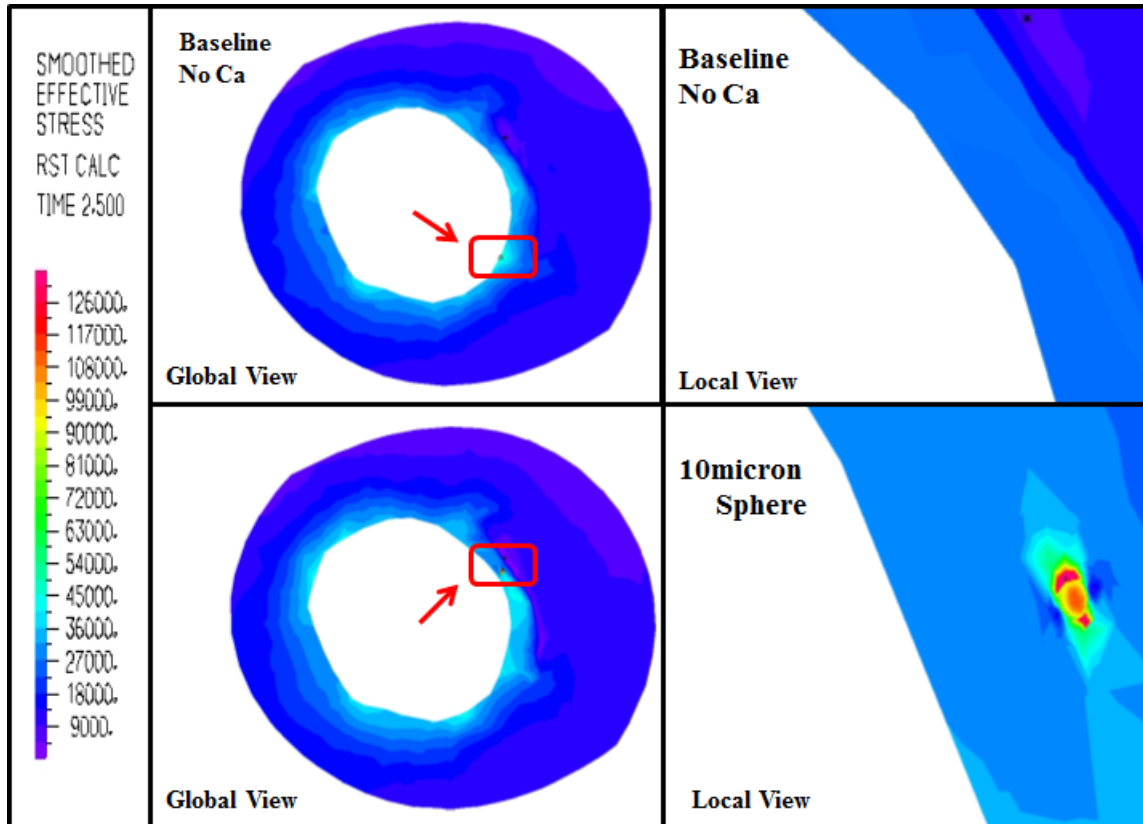
*Mesh Independency Studies.*

In this study, we combined IVUS-VH, a minimally invasive imaging modality clinically used for coronary plaque examination, with FSI simulations to investigate the effects of fibrous cap, hypertension, vascular calcification, and fibrous cap anisotropy on coronary plaque vulnerability. The results are summarized as following.

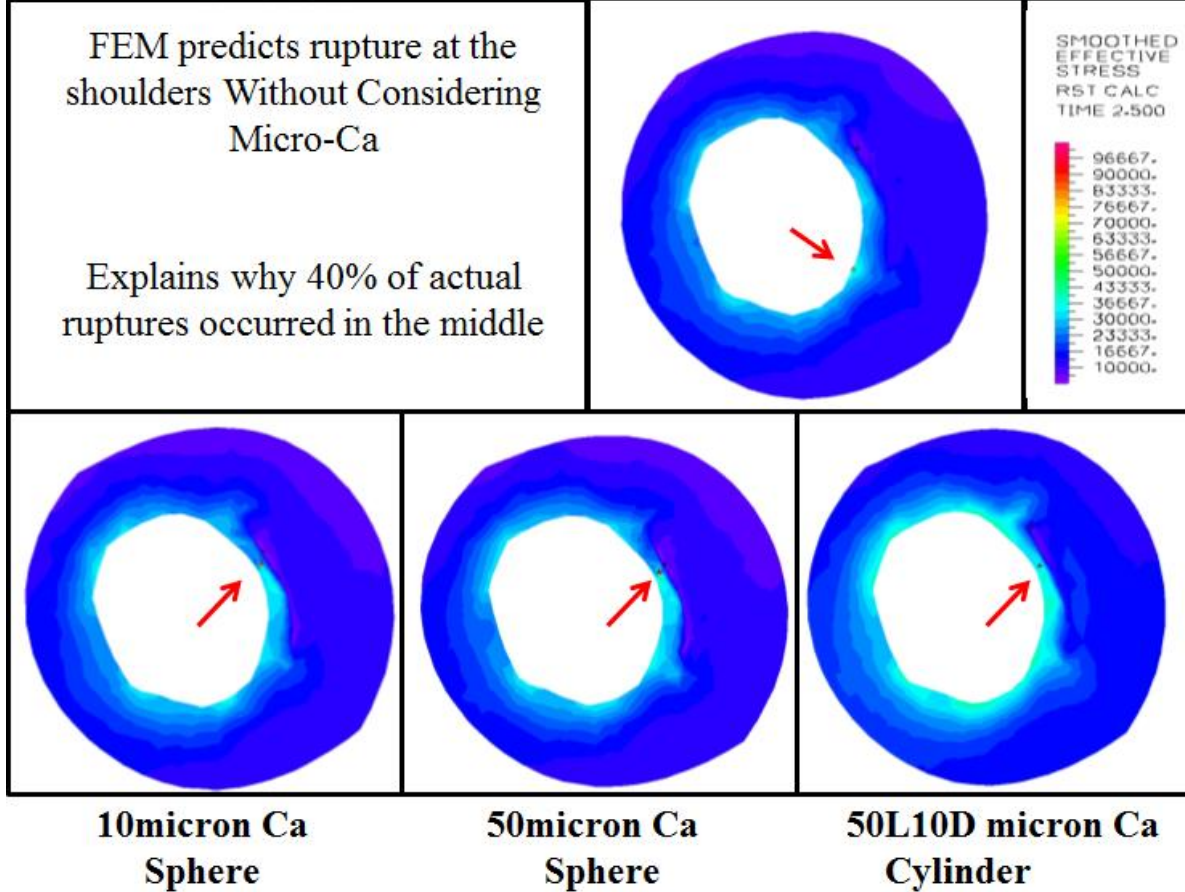
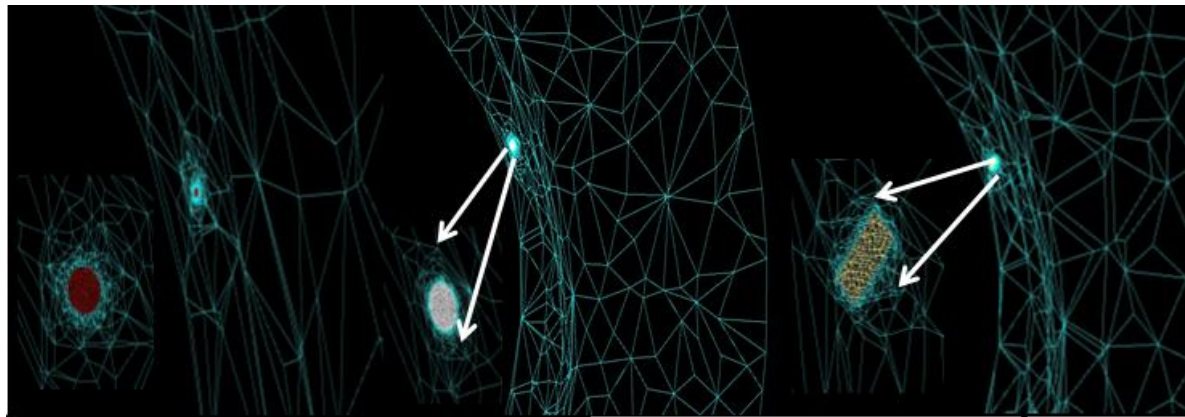


**Figure11: Optimizing the mesh size until proper grid was reached that mesh independent results would be received. Coarser grid on the left and finer one on the right reveal the grid size definitely influences the stress distribution in the simulations.**





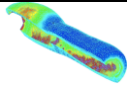
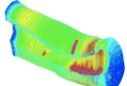
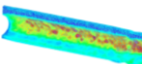
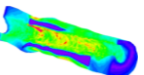
**Figure 12: Left: stress contour plots at the cross-sections in the fibrous cap region where in one case microcalcification was embedded. It revealed that the appearance of the microcalcification would change the location of peak stress predicted by the analysis. Right, zoomed in at the exact location where microcalcification was inserted and it showed that locally, microCa would present a bipolar high stress distribution along the tensile direction.**



**Figure 13: Band plot of von Mises stress distributions in all three cases showing higher stress regions can be found in the fibrous caps with the presence of micro-Ca. As shown in the figure, stress values would be substantially high at the poles of the inclusion.**

*Patient-specific baseline models*

Four IVUS based patient-specific coronary plaques as described in the methods section with various fibrous cap thicknesses, were studied. Typical characteristics of these four vessels can be found in Table 9. They were chosen as baseline samples, while normal pressure was applied, no micro-Ca was present in the fibrous cap, and the fibrous cap was modeled as isotropic

Subject	Representation	Max Diameter(cm)	Min Diameter(cm)	Fibrous Cap Thickness ( $\mu m$ )	Length of The Vessel (cm)	Large Calcification	Necrotic Pool
Case I		0.36	0.21	150~350	3.04	+	+
Case II		0.23	0.20	150~250	3.60	+	+
Case III		0.21	0.20	65	3.10	-	+
Case IV		0.16	0.14	>300	1.75	-	+

+/-: Present/Not Present

**Table 9:** Diseased Arteries and plaque characterizations.

material. Calculated Reynolds numbers at the inlet of the fluid domain at peak flow were 458 in case I, 247 in case II, 339 in case III, and 459 in case IV. Wall shear stresses at peak flow were  $157 \text{ dyn/cm}^2$ ,  $125 \text{ dyn/cm}^2$ ,  $96 \text{ dyn/cm}^2$ , and  $310 \text{ dyn/cm}^2$  in case I ~ IV, respectively. As shown in Figure 16 (case I), wall shear stress remained high throughout the entire cardiac cycle and maximal flow velocity was found at diastole due to the presence of a  $72^\circ$  phase lag. Specifically, high wall shear stress and fast blood flow also occurred at mean arterial pressure. Mean arterial pressure (MAP), where it can be approximated as pressure at diastole plus one third of the sum of systolic and diastolic pressure, is the mean pressure that the vessel experiences under pulsatile

flow physiologically. As shown in Figure 14, higher stress concentration regions can always be found in the fibrous cap, where is usually the thinner portion of the fibrous cap and is considered to be mechanically weak. Physiologically normal pressure waveform was applied to the vessels in all three cases. So, it was verified that the highest stress is most likely to occur at where the coronary fibrous cap was the thinnest. Moreover, maximal von Mises stresses in the fibrous cap were found to be 77kPa, 172kPa, 267kPa, and 82kPa during diastole and MAP stresses were 66kPa, 130kPa, and 210kPa, 33kPa in case I~ case IV as shown in Table 2.

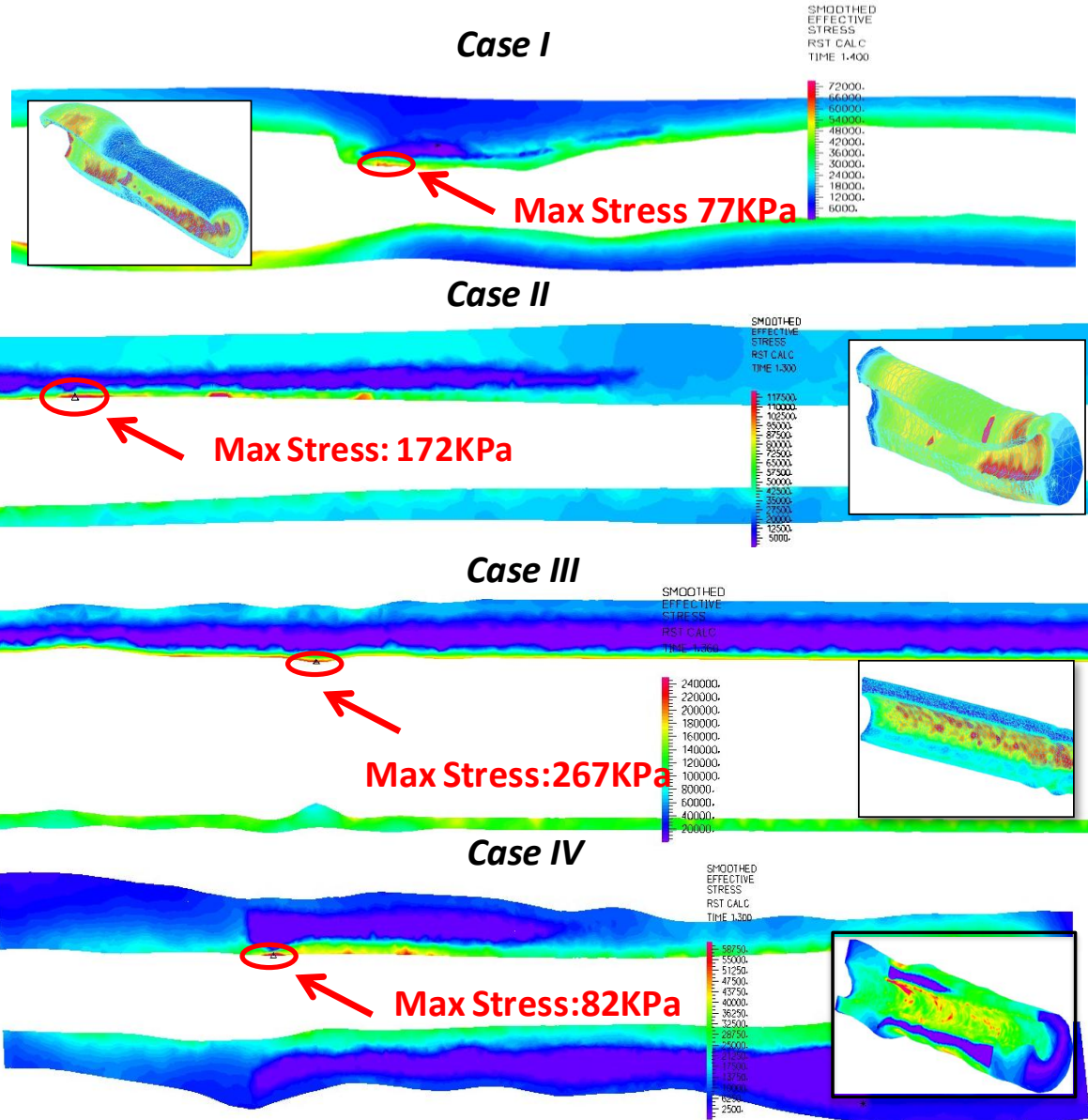


**Figure 14: Band plot of von Mises stress distributions (Isotropic Material Model) in all three cases showing higher stress regions can be found in the fibrous caps. As shown in the figure, stress values substantially increase and respond exponentially to the thinning of fibrous cap thickness. On average, F.C. thickness is reducing from Case I ~ Case III.**

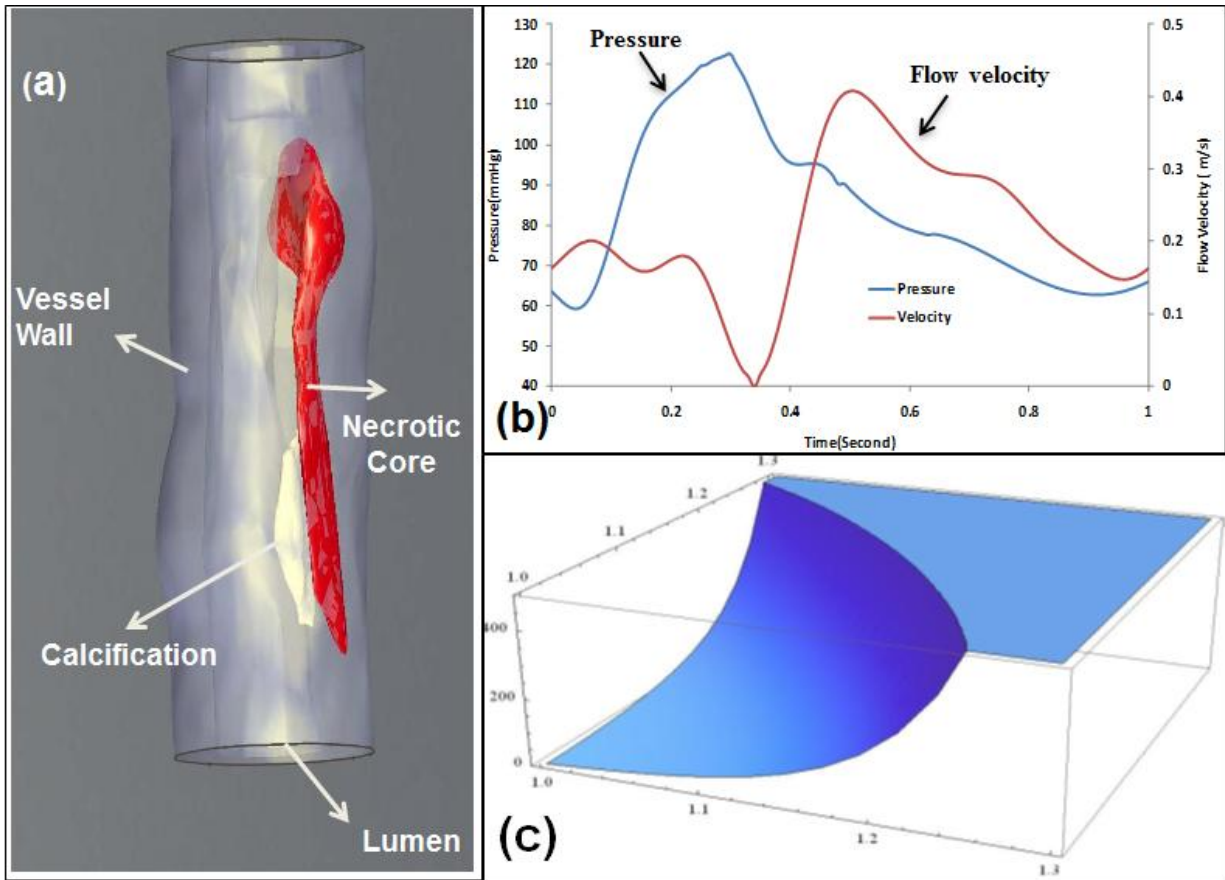


**Figure 15: (a) reconstructed coronary artery (Case I): This geometry is composed of the arterial wall in silver, macrocalcification in white and necrotic core in red. (b) Pressure and mean flow velocity extracted from patient based coronary measurement and they were applied at the outlet and inlet of the vessel, respectively [1]. (c) Three dimensional representation of the axial and circumferential Cauchy stress over corresponding stretches for fibrous cap with 65 degree fiber angle.**



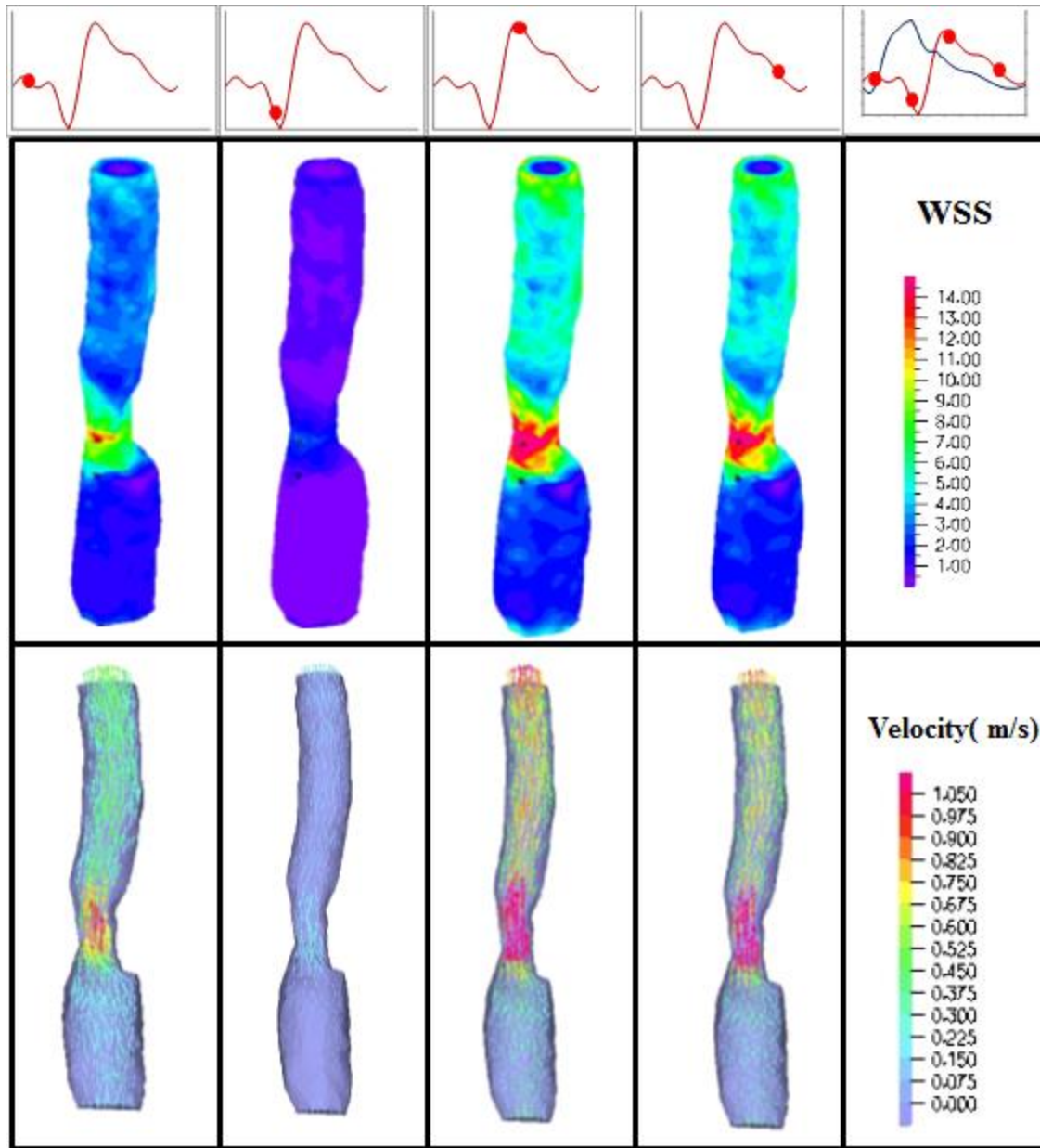


**Figure 16: Fluid wall shear stress (WSS) and velocity profiles at 4 different stages of the cardiac cycle for Case I. (Top: From Left to Right): Flow waveform at diastole, systole, peak flow rate, mean arterial pressure, and overlapped pressure and flow waveform showing a phase shifted condition. Maximum WSS and velocity can be found in the region of maximum stenosis (60%). WSS and velocity are low at systole but remain high at MAP due to the phase lag.**

### *The effect of hypertension*

Comparing to corresponding baseline models, the von Mises stress concentrations along the fibrous cap increased by 32%, 34%, 30%, and 34% following a 25% simulated blood pressure elevation in case I, II, III, and IV, respectively. MAP stresses were 83kPa, 170kPa, and 254kPa, 45kPa in Case I~ IV. As depicted in Figure 17, considerable increases of both maximal stress and MAP stress distributions along the fibrous cap demonstrate that coronary vulnerable plaque patients, who also suffer from hypertension, potentially possess higher risk of plaque rupture compared to non-hypertensive patients. WSS were 152dyn/cm<sup>2</sup>, 156dyn/cm<sup>2</sup>, and 124dyn/cm<sup>2</sup>, and 340dyn/cm<sup>2</sup> in case I ~ IV. For Case I, where the vessel is approximately 60% stenosed, peak velocity decreased from 1.94 to 1.82m/s, and reduced by 6%, in hypertensive case due to further ballooning compared with baseline model. In the other three cases, peak velocities remained almost the same as shown in Table 10.



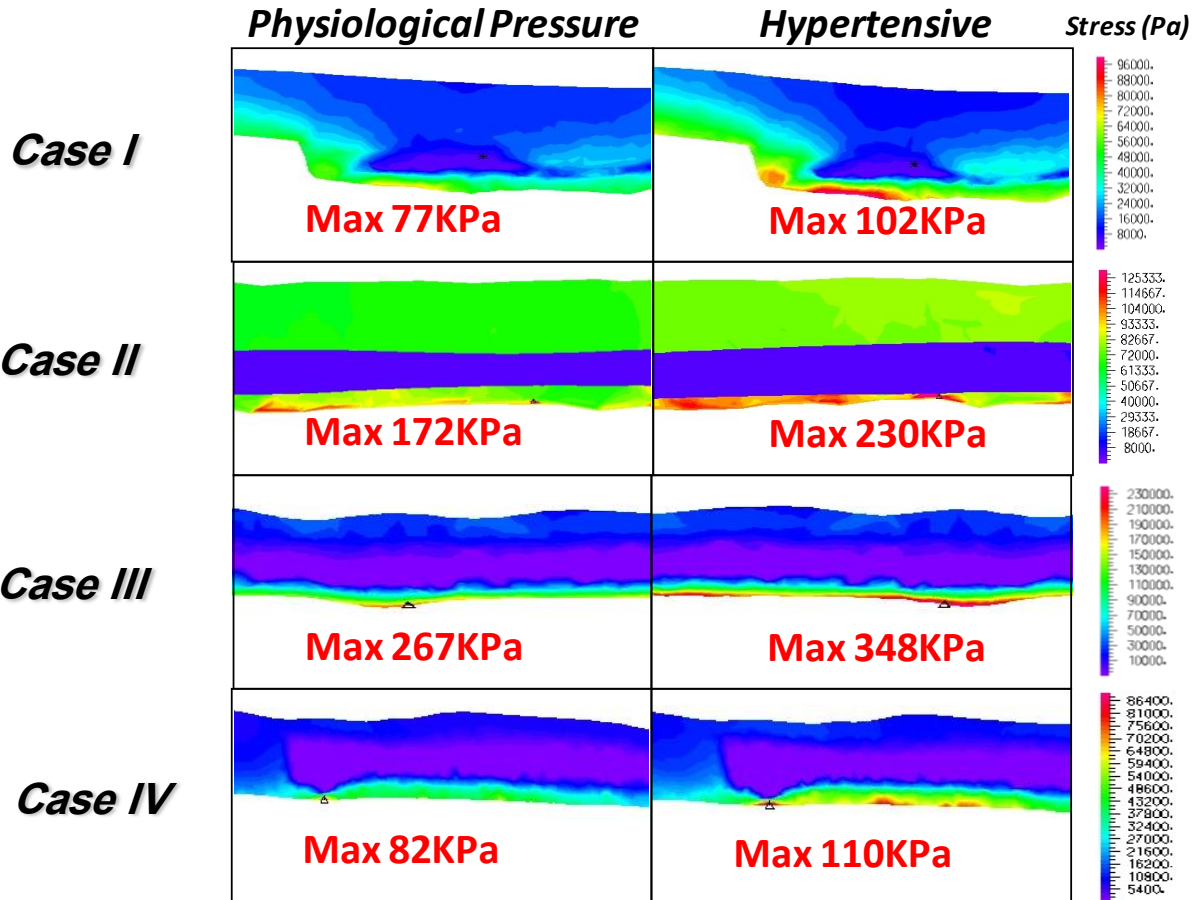


**Figure 17: Zoom-in view of the von Mises stress distributions along the fibrous cap from three hypertensive simulations. Hypertension increases the stress concentration in the fibrous cap and almost linear relationship of peak pressure and maximum stress can be derived.**

*The effect of microcalcification (micro-Ca).*

The presence of a micro-Ca, which was modeled using a sphere of 10µm in diameter in the fibrous cap, has been shown to further burden the vulnerable plaques and drastically boost up the local stress distribution around the lesion. Results obtained in this study revealed that the local maximal von Mises stresses increased from 43kPa to 103kPa for Case I, 153kPa to 408kPa for Case II, 232kPa to 510kPa for Case III, and 60kPa to 154kPa for Case IV compared to the

baseline models. The highest stresses occurred at the interface with the fibrous cap of micro-Ca. These values represent a 2.4, 2.6, 2.2, and 2.5-fold local increase (Table.10).

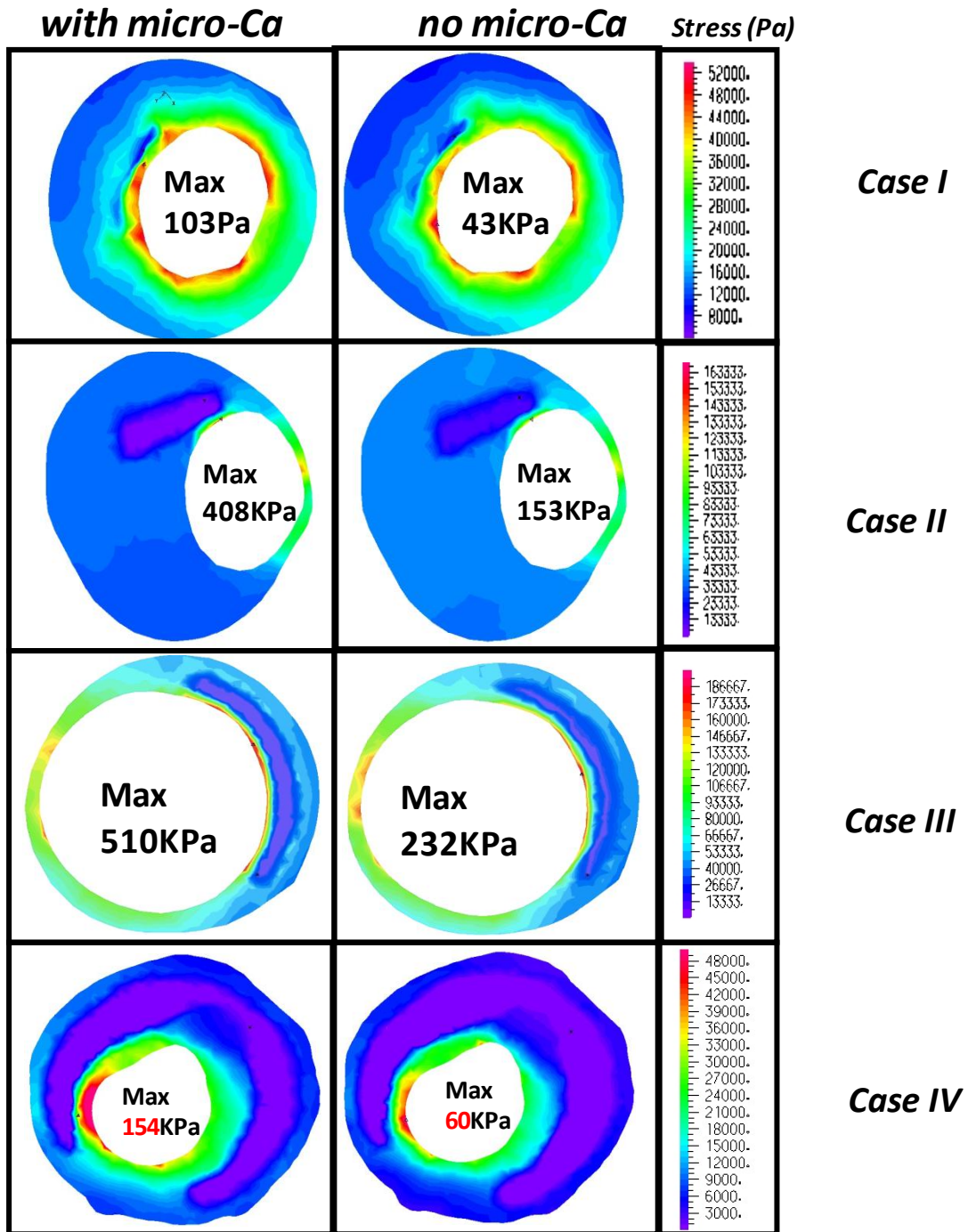


**Figure 18: Cross-sectional view of the vessels, local (background) stress distributions show the effects of miniaturized calcified spot in the fibrous cap with isotropic material properties. 2.4, 2.6, and 2.2-fold increase of von Mises stress on the cross-sectional plane, where micro-Ca are located, can be observed compared to the local stresses at the same cross-section without micro-Ca.**

*The effect of anisotropy of the fibrous cap.*

Anisotropic FSI simulations with varying fibrous cap fiber orientations were implemented to analyze the effect of tissue anisotropy on rupture risk. As shown in Table 10, maximum von Mises stress values of anisotropic FSI simulations with 5, 65, and 85 degree fibrous cap fiber angles were 238kPa, 260kPa, and 234kPa, respectively, similar to the values predicted in isotropic baseline models. Principal axis,  $p_1$ , stresses are also presented in Table 10. Simulations with different fiber angles predicted higher stress with increasing degree of fiber anisotropy.

Fibrous cap with 65 degree fiber angle produced the highest stress- $p_1$  and that was previously

		Maximal Stress Global (KPa)	Maximal Stress Local (KPa)	MAP Stress (KPa)	Peak Velocity (M/s)	Peak Wall Shear Stress (Dyn/cm <sup>2</sup> )
Case I	Baseline Model	77	43	66	1.94	157
	Hypertension	102(32%)	--	83(26%)		152
	MicroCa	103(34%)	103(140%)	84(27%)		153
Case II	Baseline Model	172	153	130	0.96	125
	Hypertension	230(34%)	--	170(31%)		156
	MicroCa	408(137%)	408(167%)	386(197%)		118
Case III	Baseline Model	267	232	210	1.02	96
	Hypertension	348(30%)	--	254(21%)		124
	MicroCa	510(92%)	510(120%)	372(77%)		95

Case IV	Baseline Model	82	60	33	0.86	310
	Hypertension	110(34%)	--	45		340
	MicroCa	154(88%)	154(157%)	41		310
Anisotropic F.C	5 Degree Fiber Angle	238	--	250kPa ( $p_1$ stress)		
	65 Degree Fiber Angle	260	626 (w/ micro-Ca)	265kPa ( $p_1$ stress)		
	85 Degree Fiber Angle	234	--	244kPa ( $p_1$ stress)		

**Table 10: Summary of max von Mises stress, MAP stress, peak velocity, peak wall shear stress, and Principal Axis 1 ( $p_1$ ) stress**

identified as diseased angle *ex vivo* according to the literature [38]. In the simulation where the fibrous cap contains an embedded micro-Ca was modeled as anisotropic tissue with 65 degree fiber angle, von Mises stress was found to be 626kPa. It increased by 23% compared to its isotropic counterpart. Moreover, it would give a 2.35-fold raise of von Mises stress in the fibrous cap for the presence of micro-Ca instead of 2.2-fold reported for the isotropic case.

Systematically examining the biomechanical factors that are influencing the coronary plaque stability by using IVUS based FSI simulations showed that fibrous cap thickness, hypertension, vascular calcification and anisotropic material property directly regulate the critical stress/strain distribution in the vessel.

*Geometry reconstructed from Micro-CT imaging data.*

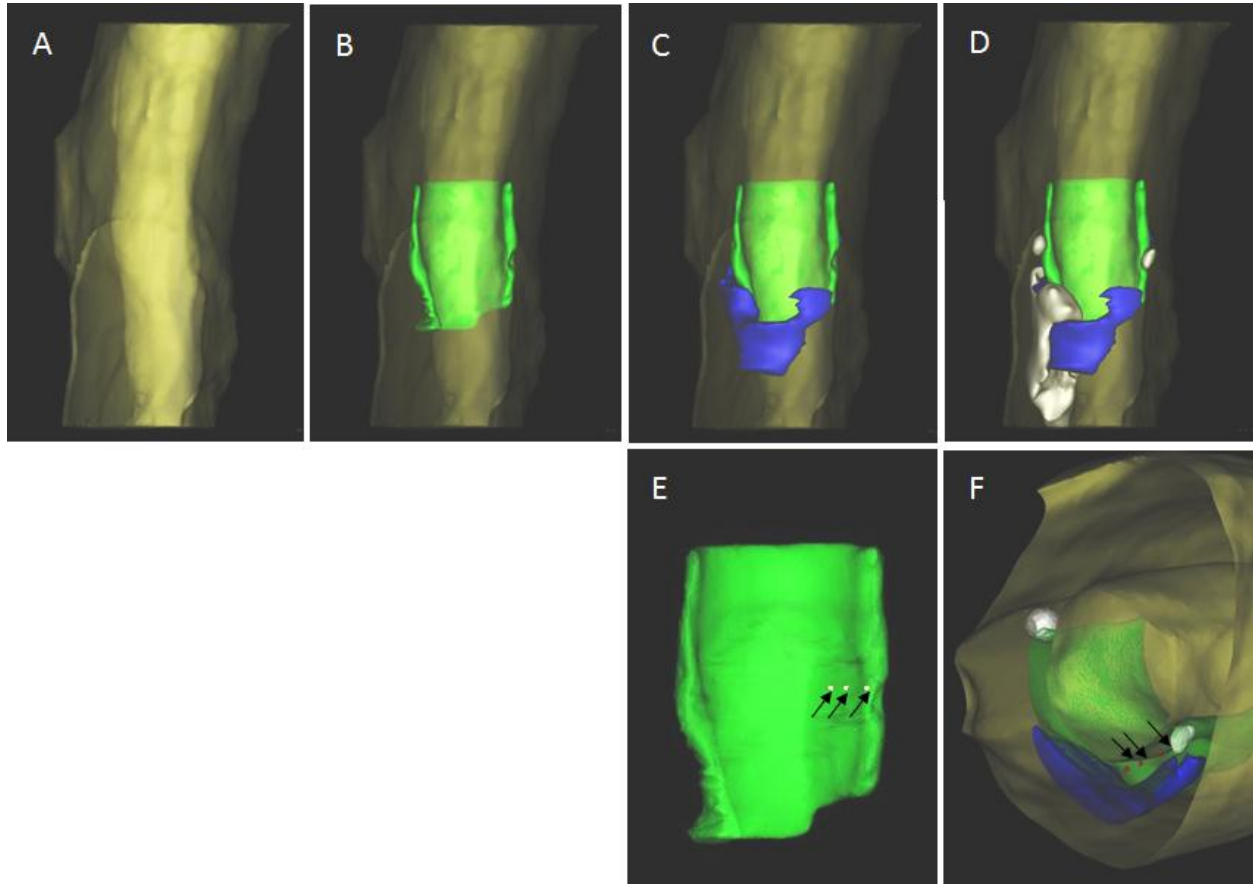


**Figure 19: Coronary vulnerable plaque 3D reconstruction from MicroCT. (A) – (D) 3-D reconstruction of coronary vessel with atheromatous lesion is shown. Wall and lumen of vessel are shown in (A). Fibrous cap of atheromatous lesion is displayed in green (B). Fatty lipid core is shown in blue (C). Several macrocalcifications are shown in white (D). Microcalcification landmarks are presented overlaying the fibrous cap in 3-D view (E) and cross-sectional view (F). Arrows in (E) and (F) point out the three microcalcifications.**

#### *Hemodynamics of VP (Micro-CT)*

In the case that the coronary plaque geometry was reconstructed from advanced Micro-CT imaging data and more importantly, the critical parameters, such as fibrous cap thickness was accurately quantified and the presence of three microCa in the fibrous cap were actually imaged instead of artificially embedded as in the other IVUS cases presented in this thesis. Blood flow

and wall shear stress (WSS) distributions are presented in Figure 20 at three phases of the cardiac cycle: (1) peak systole, (2) early diastole and (3) late diastole. Blood velocity and WSS are maximal at peak systole along the region of stenosis, specifically at the location of the fibrous cap and the primary vessel pathology. At peak systole, the maximum velocity of 46 cm/s and maximum WSS of 53.1 dynes/cm<sup>2</sup> correspond to the location of the primary vessel pathology – as compared to normal flow velocity of 25 cm/s at peak systole in a healthy main coronary artery circulation [67]. At maximal flow, the peak velocity and WSS increase to 81 cm/s and 115 dynes/cm<sup>2</sup>, respectively. Phase shifted peaks of pressure and blood flow induce a prolonged

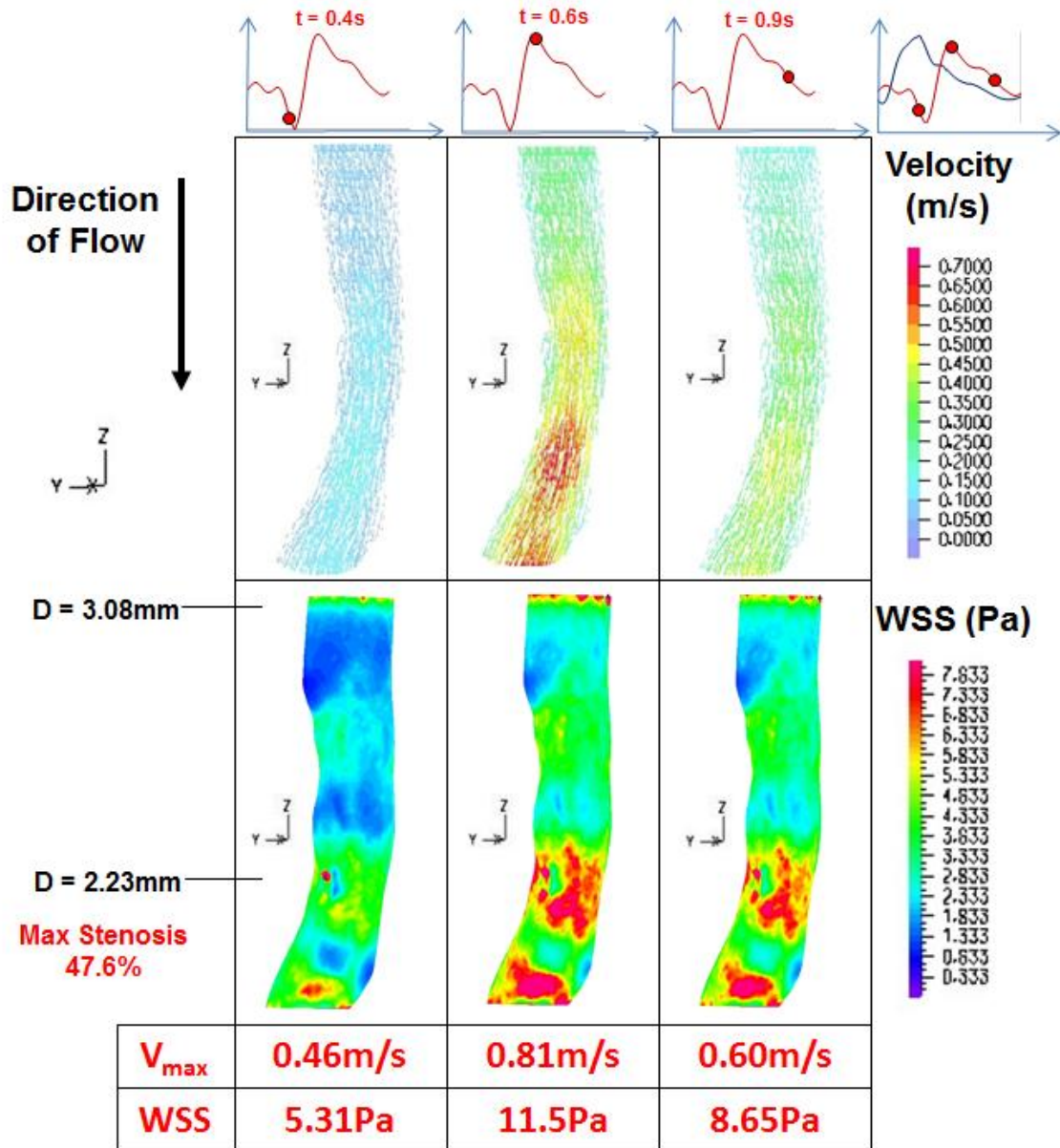


**Figure 20. Fluid domain results from FSI simulations. Velocity and wall shear stress (WSS) profiles of the coronary artery under dynamic pulsatile conditions with phase lag are shown at three stages of the cardiac cycle: peak systole (0.4s), early diastole – peak flow (0.6s), and late diastole – flow deceleration (0.9s). Region of highest velocity and wall shear stress is located at the region of maximum stenosis (47.6% compared to inlet). This region of stenosis corresponds to the pathology of interest, the coronary vulnerable plaque (CVP). It is observed that WSS remains high throughout the cardiac cycle.**

duration of high wall shear stress throughout the entire cardiac cycle as compared to synchronous waveforms. During late diastole, the peak velocity and WSS were 60 cm/s and 86.5 dynes/cm<sup>2</sup>,

respectively. All maximum velocities and WSS values coincide with the primary vessel pathology along the distal portion of the vessel, which is the region of maximal stenosis as described earlier. Blood flow results (peak velocity and WSS locations and values) did not appear to be affected by changing the material properties of the solid domain.

#### *Overview of VP arterial wall dynamics and effects of micro-Ca on fibrous cap*

Stress within the solid phase components of the vessel geometry, as obtained from fully-coupled FSI simulations are summarized in Table 12. We present first the effects of the micro-Ca inclusion on fibrous cap stress with isotropic material formulation, for comparing them to previous analytical models of micro-Ca inclusion [20] and additional numerical studies [23]. Stress values of the fibrous cap are of primary interest in assessment of the VP risk of rupture. Using an isotropic material formulation for the fibrous cap, the inclusion of the micro-Ca appears to increase the maximum stress levels from 33.17 kPa to 71.47 kPa, 2.15-fold increase, Table 2). The stress on the vessel wall itself remains at 160 kPa in both cases (with and without the micro-Ca). Thus, the peak stress on the fibrous cap increases to 2.15-fold of its original value as a result of micro-Ca inclusion. Table 12 summarizes the fibrous cap stress and wall stress as a percent change with respect to the original isotropic fibrous cap simulation with no micro-Ca inclusions.



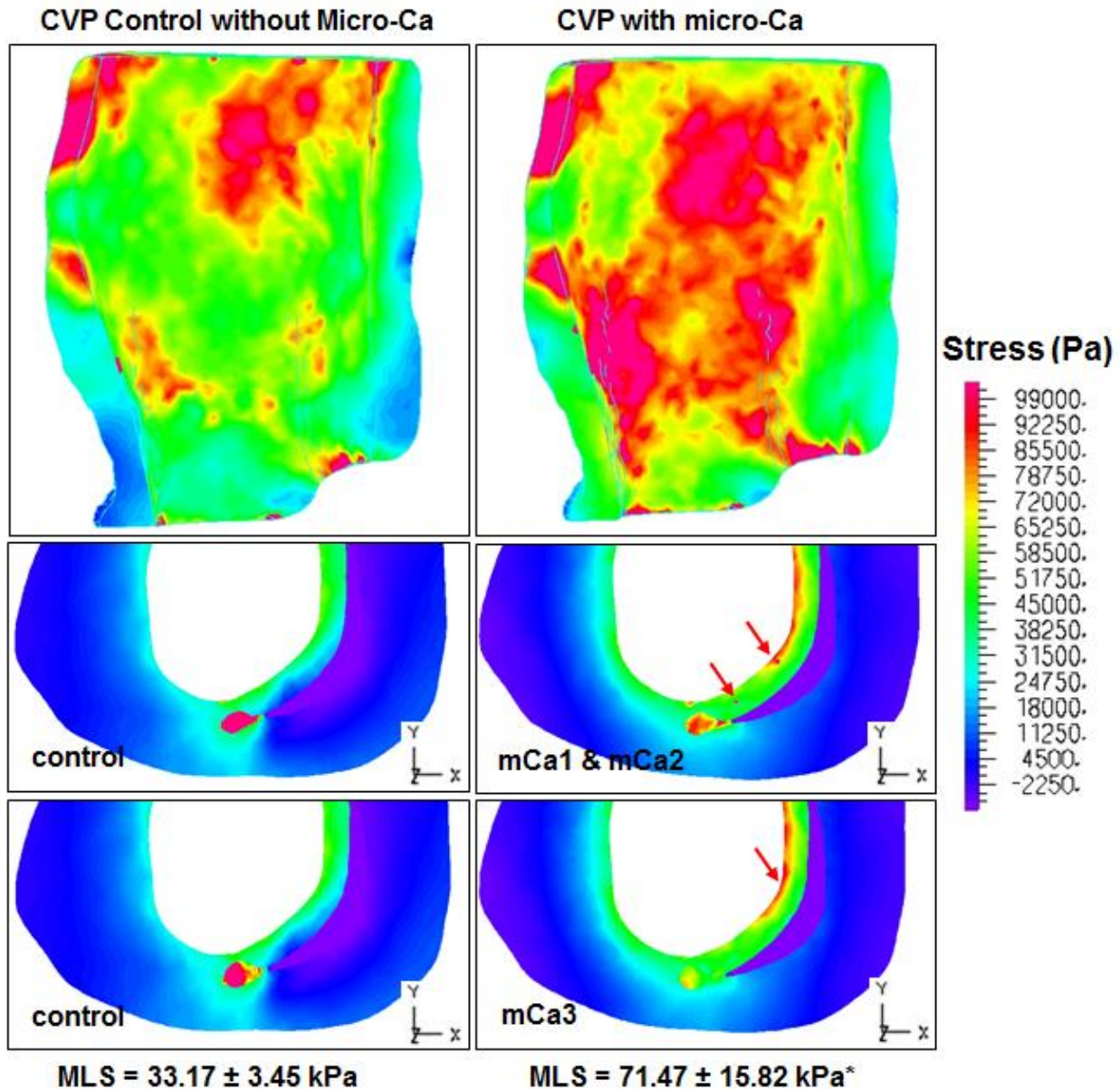


**Figure 21. The effect of micro-Ca on fibrous cap stress. Three micro-Ca embedded in the fibrous cap, using micro-CT, were simulated using FSI. All three micro-Ca were simulated together in the same geometry. Cross sections of the CVP geometry are shown at the axial level for the three micro-Ca. Corresponding results are shown for the same axial levels without embedded micro-Ca (control simulations). Maximum von Mises stress results, reported for each cross section individually, show a 2.15-fold increase in the local stress values of the fibrous cap with micro-Ca inclusion (paired *t*-Test,  $p < 0.015$ ).**

*Effect of microcalcifications on stresses developing in the fibrous cap*

The effect of each of the three micro-Ca individually examined is presented in Figure 21. Cross sections of the geometry, at the axial location of each micro-Ca, highlight the level of maximum wall stress (Figure 21). When the micro-Ca1, micro-Ca2, and micro-Ca3 are examined individually, it appears that the local stress changes are much more substantial. Local stress increases range from 29.2 kPa to 57.8 kPa (micro-Ca1), 35.5 kPa to 67.8 kPa (micro-Ca2), and 34.8 kPa to 88.8 kPa (micro-Ca3). All three micro-Ca were included in the FSI simulation, producing an average 2.16-fold increase (micro-Ca1: 1.98-fold increase, micro-Ca2: 1.91-fold increase, micro-Ca3: 2.6-fold increase) in the fibrous cap stress level ( $p < 0.015$ , paired  $t$ -Test, when considering each micro-Ca individually).

*Stress distribution around the microcalcifications*

Analyzing the principal stress distribution at cross sections, stress concentrations can be observed around the micro-Ca in the direction of the applied load at the poles of the inclusions.

Model	$C_1$ (kPa)	$D_1$ (kPa)	$D_2$
Fibrous Cap & Vessel Wall	28.14	1.31	11.5
Lipid Core	0.5	0.5	0.5
Calcification	281.4	13.1	11.5

**Table 11: Material Parameters determined for the material model used in our FSI simulations**

Simulation Case	Max Wall Stress (with FC) (kPa)	Averaged Local Fibrous Cap Stress around micro-Ca (kPa)	Hemodynamics at peak systole (t = 0.4s)		Hemodynamics at peak flow (t = 0.6s)	
			WSS	Velocity	WSS	Velocity
Isotropic F.C w/o Micro-Ca	54 / 35.5	33.17 ± 3.45	5.31	0.46	11.5	0.81
Isotropic F.C with Micro-Ca	117 / 88.8	71.47 ± 15.82 (2.15-fold increase)	5.31	0.46	11.5	0.81

Table 12. Fibrous cap stress results, flow and wall shear stress (WSS) values

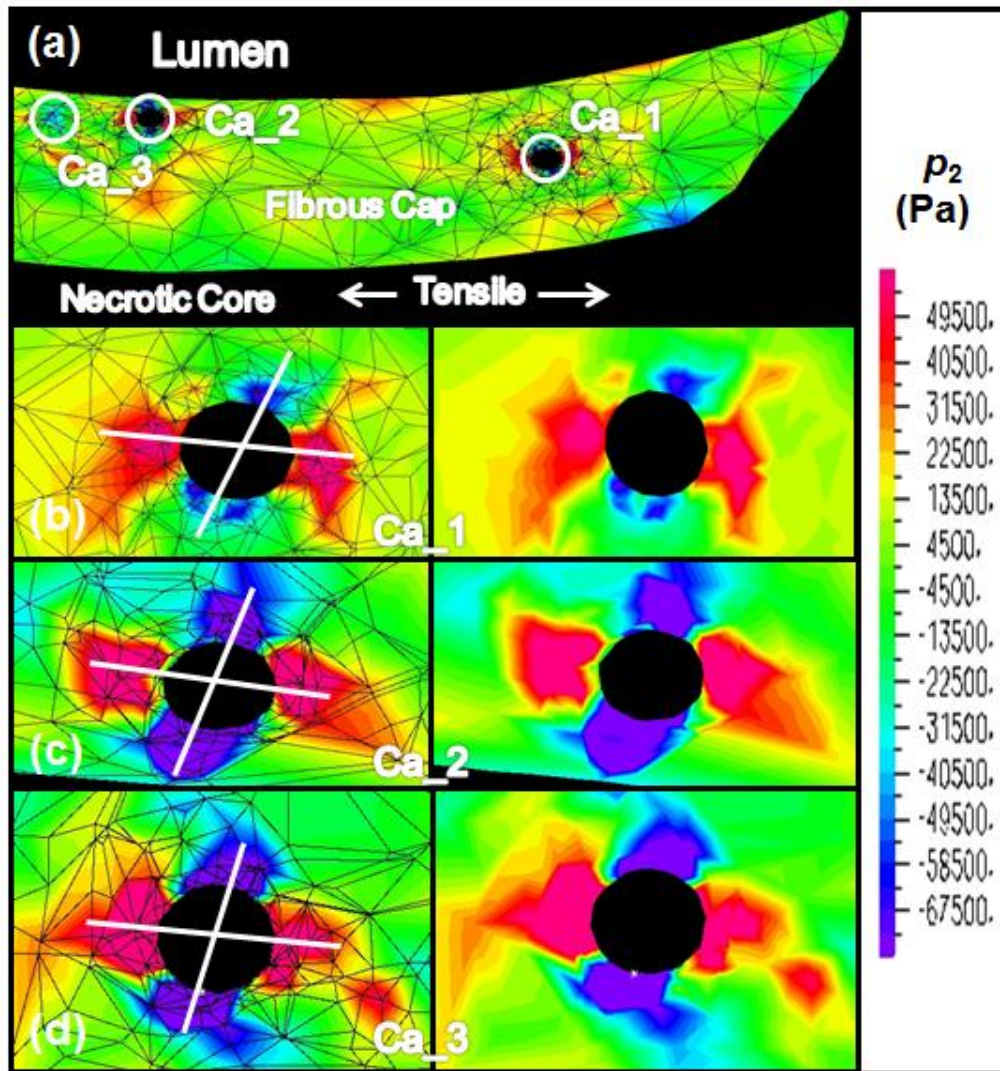


Figure 22. Principal stress,  $p_2$ , distribution at the microcalcified region. (a) Principal stress along the fibrous cap with isotropic material properties is shown. (b) Stress values increase from 29.2 kPa (without micro-Ca) to 57.8 kPa (with micro-Ca) for the first micro-Ca (geometry with and without the computational grid). (c) Stress values increase from 35.5 kPa (without micro-Ca) to 67.8 kPa (with micro-Ca) for the second embedded micro-Ca. (d) Stress values increase from 34.8 kPa (without micro-Ca) to 88.8 kPa (with micro-Ca) for the third embedded micro-Ca.

We observed poles of compressive and tensile stresses at each one of the micro-Ca embedded in the fibrous cap. The compressive poles (shown in blue, Figure 22) are on the radial direction of the vessel whereas the tensile poles (shown in red, Figure 22) are on the circumferential direction. These bipolar stress distributions have hypothesized [20, 23, 68] to lead to the debonding of the rigid inclusion causing a rupture of the fibrous gap.

## **Discussion:**

### IVUS Studies

Intravascular ultrasound is a minimally invasive technique to assess coronary artery plaque morphology and progression. Fluid-structure interaction (FSI) simulations were implemented using coronary artery model reconstructed from IVUS-VH imaging data. The methodology of combining FSI simulation and reconstruction of clinical imaging data has already shown its versatility and usefulness in studying various vascular pathologies such as carotid disease [69], abdominal aortic aneurysm [54], and coronary plaque [19, 53]. In this study, it was found that is possible to further extend the use of IVUS-VH based FSI method to study several aspects of coronary vulnerable plaque disease. The effects of cap thickness, material anisotropy, the presence of macro and micro-level calcified spot in the fibrous cap, and hypertension on plaque vulnerability in IVUS-VH reconstructed patient based coronary models were systematically assessed.

Previous studies confirmed that vulnerable plaque rupture leads to immediate thrombosis and total arterial occlusion [7-10, 15]. However, the mechanism and primary cause of plaque rupture remain unclear or controversial. Biomechanical factors that are usually considered in vulnerable

plaque mechanical analysis include fibrous cap thickness, vessel anisotropy, macro- and micro-Ca in the vulnerable region, cyclic bending caused by constant cardiac motion, and cap erosion due to biochemical degradation of the vessel [19, 23, 38, 53, 70]. In our study, we focused on fibrous cap thickness, the presence of micro-Ca in the fibrous cap, anisotropic material behavior, and hypertension. At sites of hemodynamic strain created by typical atherosclerotic flow patterns, increased inflammatory cell activities leading to the infiltration and accumulation of necrotic inside vessel wall can be observed and this process alters the fibrous cap by enlarging the volume ratio of necrotic core and the fibrous cap underneath [5]. As shown in Figure 14, the baseline models (normal pressure, no micro-Ca, and isotropic model) confirmed that reducing cap thickness increases the stress concentration in the lesion and this finding greatly corresponds to the literature, in which stress values increase exponentially with the fibrous cap, whose thickness is below the  $65 \mu\text{m}$  threshold value [70, 71]. To study the effects of hypertension on plaque vulnerability, we elevated the baseline pressure waveform by 25% percent while the peak pressure value stayed in the physiological range. Results shown in Figure 14 reveal that stress distributions developed in the fibrous cap in all three models respond almost linearly to the pressure elevation and seem to be independent of cap thickness [70]. Stress values increased by 32%, 34%, and 30% following 25% simulated blood pressure elevation in case I, II, and III, respectively. Thus, for coronary vulnerable plaque patients who also suffer from hypertension, fibrous cap vulnerability can be precisely evaluated by following the IVUS-FSI methodology.

However, studies using finite element method (FEM) to investigate the contribution of vulnerable plaque morphological features such as cap thickness and necrotic pool size on cap vulnerability and to predict the actual rupture location still cannot completely explain why,

clinically, forty percent of actual ruptures occurred in the middle of the fibrous cap instead of shoulders, where simulations would predict to be the highest stress region. An analytical model [20] described by Vengrenyuk, et al. and later confirmed by the same group with FEM simulations propose that interfacial debonding due to microcalcified inclusions (10 ~ 20  $\mu\text{m}$  diameter) can be accounted for many “mysterious” fibrous cap ruptures [23]. Previously, our group studied the effects of microcalcifications by embedding an artificial solid body in an idealized coronary model using FSI simulations and similar results were observed [19]. In the present work, we have examined the impact of micro-Ca on cap stability both locally and globally, where the local stress directly measures the stress developed at the same location in the fibrous cap with and without micro-Ca. The presence of a spherical microcalcified spot of 10  $\mu\text{m}$  diameter increased background von Mises stresses by 2.4, 2.6, 2.2 and 2.5-fold (Figure 18) in case I through IV, respectively. This observation is in close agreement with the hypothesis proposed by Vengrenyuk, et al. that more significant increase in local circumferential stress would be observed if the micro-Ca are embedded in the region of high background circumferential stress. As shown in Table 10, the local (background) von Mises stresses at the sites where micro-Ca were inserted were sufficiently high and comparable or equal to global maximum values in all baseline models. Especially, in Case III, where the fibrous cap is with a uniform thickness of 65  $\mu\text{m}$ . In Case II, the fibrous cap thickness at the location of the inserted micro-Ca is 150  $\mu\text{m}$  (limit of IVUS resolution) and stress values measured are also comparable to Case III but 20% lower (Table 10). However, none of the cases reported exceeds the stress threshold for rupture plaques [72]. In addition, we observed that large calcifications would not affect the stress distribution and could even stabilize the cap if these macrocalcifications are sitting at the shoulders of fibrous cap [20, 23]. Among several

proposed mechanisms, macrophage and smooth muscle cell apoptosis is considered to be responsible for the genesis of vascular calcification and it is suggested that necrosis and apoptosis are prevalent in diseases, such as atherosclerosis [73]. Detecting the microcalcification in the fibrous cap and take it into account in FSI coronary vulnerable plaque study would provide a more representative model of the disease.

We looked into the fact that most biological tissues, such as coronary arteries, do behave anisotropically under loading and realized that most available constitutive models describing arterial walls were derived based on unidirectional mechanical testing data [27, 34, 38, 48, 63, 74-79]. Since performing mechanical testing on coronary artery specimen, especially fibrous cap, has been extremely difficult and human coronary arterial property data are very limited in the literature. Three-dimensional modified Mooney-Rivlin model proposed by Tang, et al. based on *ex vivo* biaxial mechanical testing of coronary artery specimen considers tissue anisotropy by incorporating collagen fiber orientations [52, 53, 69]. In parametric FSI simulations examining tissue anisotropy, a distinct layer of fibrous cap in case III was modeled with different fiber angles varying from  $5^\circ$  to  $85^\circ$ . Our results indicate that tissues with  $65^\circ$  fiber angles produce the highest von Mises and  $p_I$  stress values among all angles used as shown in Table 10. In fact, tissues with 65-degree fiber orientations were predicted to be stiffer in both axial and circumferential directions in terms of Cauchy-Green stresses based on the modified Mooney-Rivlin material model. This particular angle was clinically found in patients with coronary atherosclerosis [38]. One possible explanation to this observation may be biomechanically stress-driven reorientation of the fibers. Kuhl, et al. pointed out that the collagen fibers in biological tissues undergoing remodeling would allow for a continuous reorientation to eventually align in the direction of maximum principal strain [80]. Much higher von Mises

stress was observed in the simulation modeling the combined effects of micro-Ca and if the micro-Ca was located in the anisotropic fibrous cap with 65-degree diseased fiber angle. It is already explained that isotropy of biological material has only been validated in the small strain region and sudden stress increases would be observed once the material is stretched beyond its potential threshold [81, 82]. It may also help us explain the observation that slightly lower von Mises stress values were received when non-calcified fibrous cap was modeled with anisotropic material properties (Table 10).

Additionally, we performed FSI simulations using physiological pressure and flow waveforms with a  $72^\circ$  phase lag[1]. The results show that delayed occurrence of coronary maximal flow after pressure peak would prolong the duration of high stress experienced by the wall throughout the cardiac cycle, especially, flow wall shear stress remains in a higher level and greater MAP stress would be observed as well compare to simulation results using synchronized pressure and flow waveforms (Figure 15). The reason for the phase shift that we have applied (72 degrees) is that this is the value that is reported in the literature by clinical measurements and this is important as most FSI simulations do not include the phase shift at all. Our results indicate a prolonged period of higher arterial wall stresses during the diastolic phase as a result). Womersley solution aside, the main reason for the phase shift in coronaries is because during systole the vigorous contraction of the LV almost blocks the perfusion through the 'squashed' coronaries (seen as a sharp dip in the flow rate waveform during peak systole) followed by a major portion flowing during diastole. Interestingly, the Womersley classical solution with typical coronary  $\alpha$  value of 3-4, as calculated for the case we studied, predicts almost identical phase shift approximately 70 degree as shown in Figure 23.



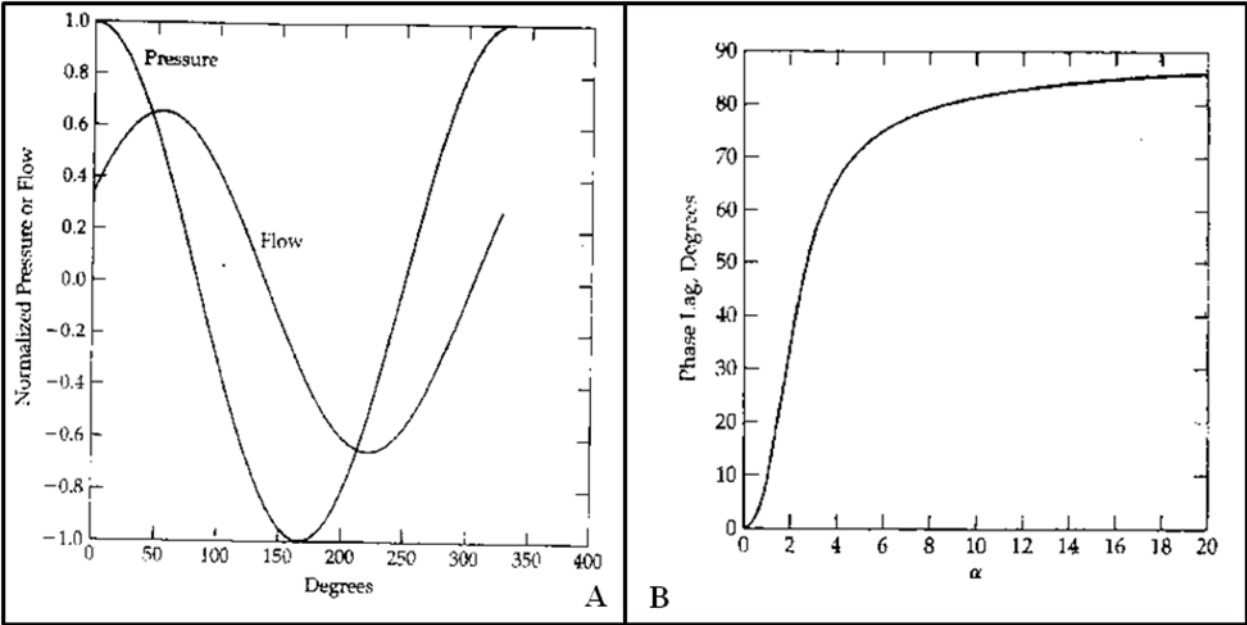


**Figure 23: a) Relationship between pressure and flow rate for  $\alpha=3.34$ . b) Phase lag between pressure and flow as a function of  $\alpha$ .**

By analyzing the effects of the biomechanical factors mentioned in the study, better understanding of the risk of rupture of the coronary vulnerable plaque was obtained. Fibrous cap thickness, micro-Ca in the lesion, anisotropic material property, and hypertension contribute differently to the fibrous cap vulnerability. Nevertheless, detailed geometrical features of the fibrous cap, such as thickness and micro-Ca, cannot be easily captured due to limited imaging resolution. IVUS-VH allows the assessment of atherosclerotic plaque morphology by using radiofrequency analysis of ultrasound signals; however, it has some limitations. IVUS-VH has axial resolution of 150 $\mu\text{m}$ , which an unstable fibrous cap of 65  $\mu\text{m}$  thick cannot be visualized. Furthermore, IVUS-VH is unlikely to detect subtle changes in plaque composition that occur over small distances due to ultrasound beam cross-sectional thickness. In the FSI simulations, laminar blood flow was assumed and arterial wall was modeled as one unified body instead of layer specific as in reality. Further studies incorporating exactly patient specific pressure and

flow patterns and layer specific modeling of the vessel components would be necessary to provide better predictions of plaque rupture. The present work should be a useful contribution to coronary vulnerable plaque studies because we systematically evaluated the effects of major biomechanical factors up to date on cap stability and further established the connections between IVUS imaging modality with FSI simulations.

#### Micro-CT Studies

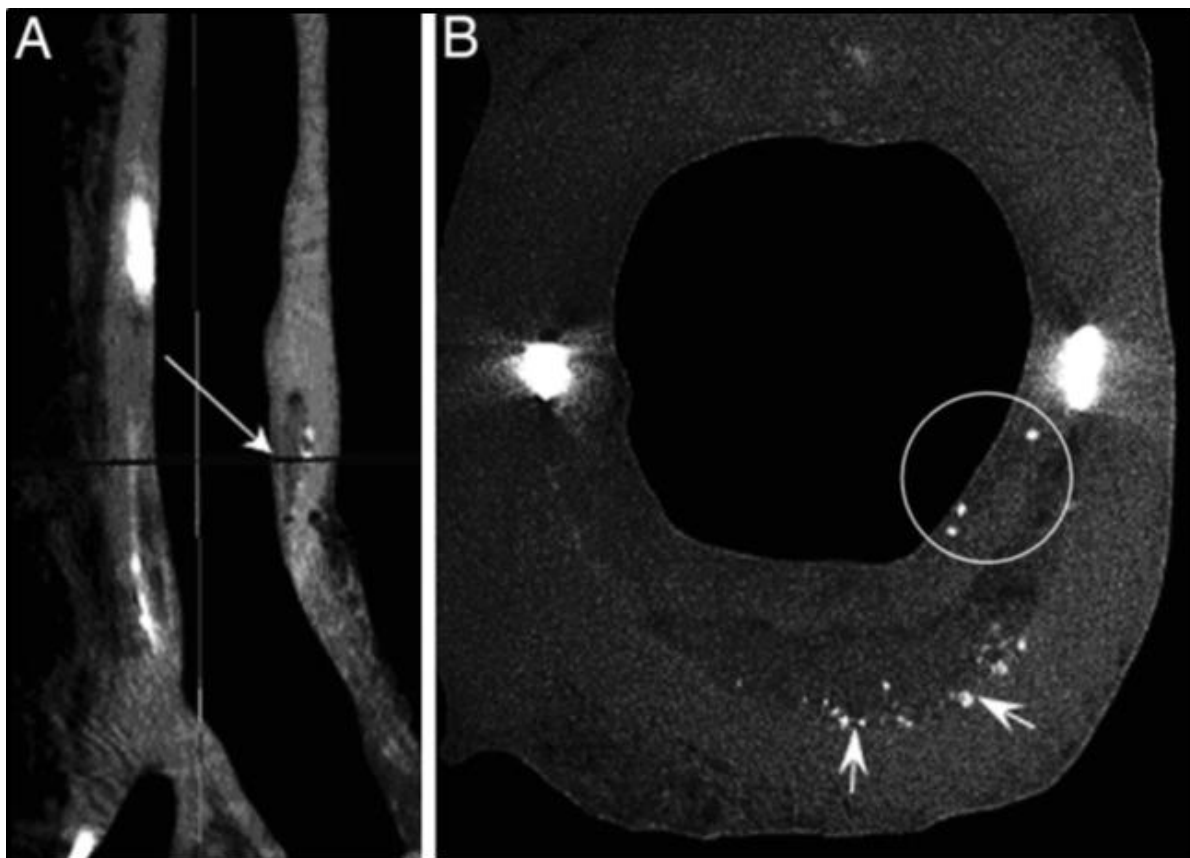


**Figure 24: Micro-CT detection of cellular-level microcalcifications in a fibrous cap. (A) Sagittal view of a coronary artery segment with microcalcifications in the thick cap (35  $\mu\text{m}$  resolution). (B) A cross-section of the lesion (arrow in A) corresponding to the plane marked by an arrow in A with cellular-level microcalcifications 10 to 20  $\mu\text{m}$  diameter in the cap (circled) and numerous calcific deposits at the bottom of the lipid pool shown by arrows (7  $\mu\text{m}$  resolution)(Vengrenyuk, PNAS, 2006)**

Fluid-structure interaction (FSI) simulations of coronary vulnerable plaques were performed using detailed post-mortem micro-CT scans of coronary pathological specimens. We have previously conducted FSI simulations to study the effects of microcalcification embedded in VP fibrous cap in idealized geometries of coronary arteries [19]. In this study, we combine highly-resolved micro-CT imaging, which enables the capture of micro-CA embedded in the VP fibrous cap with FSI, to study aspects of vascular pathology that would not be apparent using conventional scanning methods, e.g. IVUS or conventional CT. The use of micro-CT allows us to resolve the various components of the VP pathology. Moreover, segmentation of soft tissue components in CT is extremely difficult and it was an advancement achieved by microCT used in this study to distinguish the lipid pool from the rest of the tissue components. The original image first published in Vengrenyuk et al 2006 is shown in Figure 23 to emphasize the determination of fibrous cap thickness and the presence and proper locations of the microCa were indeed imaged. This vessel was pressure fixed before imaging process and the integrity of the geometry was not identical but should be similar to the one in vivo. The complex fibroatheroma, composed of a fibrous cap with micro-Ca inclusions, lipid core, and a macrocalcification, was simulated using a fully-coupled FSI methodology. These FSI simulations facilitate the study of the reciprocal interaction of the coronary hemodynamics and the solid components of the vessel wall and the VP. We are able to produce highly detailed stress gradient mapping of the fibrous cap, the most vulnerable aspect of the complex fibroatheroma which is prone to rupture (Figure 22). Estimating the stress levels of a non-ruptured fibrous cap has medical implications for individuals suffering from chronic ischemic disease, which can manifest as any one of the subcategories of acute coronary syndrome [83]. Wall stress would be dominantly dependent on the imposed pressure waveform. For this reason

and due to the fact that we do not know the actual pressure of this patient we imposed physiological pressure conditions were applied at the outlet of the vessel. If the pressure in pathophysiologic will increase substantially, the stresses acting on the coronary wall will also increase accordingly and there has been a linear relationship between the pressure elevation and maximal stress developed (study under preparation). However, an important aspect for this study was the effect of a phase shift between pressure and flow on plaque stability and the major observation due to this fact was a prolonged period of wall shear stress would be induced. According to recent clinical and numerical studies [58, 84], wall shear stress has been found associated with the progression and transformation of coronary atherosclerotic plaque and arterial remodeling. More specifically, coronary wall shear stress would influence the necrotic core growth and calcium progression. Coupling the solid and fluid domain would provide us the opportunity to better assess not only wall stress mainly contributed by hydrostatic pressure but also the wall shear stress heavily influenced by the blood flow

We studied factors that can affect the vulnerability of fibrous cap and lead to localized increases in stress. Inclusion of micro-Ca in the fibrous cap was shown to significantly increase stress locally over 4-fold. In Figure 21, we show that micro-Ca inclusions cause regions of high stress to move from the interface between fibrous cap and lipid core to the interface between the fibrous cap and vessel lumen. This relocation of high stress to the luminal interface could be a trigger for plaque rupture pathogenesis, based on current understanding [23] Previous patient-specific simulations suggested that VP rupture location tends to be close to the fibrous cap shoulder [72]. The Weinbaum group was the first to introduce the concept of relocation of the peak stress based on calcified cellular material [23]. Our results verify this idea, showing that the stresses do, in fact, move from the shoulder to the center of the fibrous cap with micro-Ca

inclusion. Figure 22 depicts the concentration of the stress in fibrous cap for all three embedded micro-Ca cases and also present cross-section at the actual location of micro-Ca.

The previously described analytical model of the effect of micro-Ca inclusions on fibrous cap stress, predicts that a fibrous cap with mean thickness of 200  $\mu\text{m}$  will have increased levels of stress with a single micro-Ca inclusion of 10-20  $\mu\text{m}$  diameter [20]. In this analytical model of an idealized fibrous cap, the microcalcification inclusion increased the stress from below 200 kPa to above 300 kPa. In our isotropic micro-CT based FSI simulation since we have a substantially thicker fibrous cap, approx. 300  $\mu\text{m}$  and also the embedded micro-Ca had larger diameter, varying from 40-60  $\mu\text{m}$ , the calculated stresses were substantially lower (control: 54 kPa to approx. 90 kPa with micro-Ca, corresponding to a slightly smaller than 2-fold stress increase). The results from these FSI simulations are very close to the analytical model predictions when utilizing the isotropic material formulation (Figure 22). Furthermore, our FSI results are in agreement with previously published experimental values [7, 9, 12, 72, 85].

Previous finite element numerical studies identify a mean value of 545 kPa as a threshold of rupture based on patient-based simulations of known ruptured coronary plaques [72]. This threshold of rupture represents a range of peak stress values from 300 to 900 kPa, with multiple factors arguably contributing to the actual patient-specific rupture threshold. The peak stress for control non-ruptured atherosclerotic lesions was reported to be approx. 100 kPa with a 300  $\mu\text{m}$  fibrous cap [20]. Our control FSI simulation from a patient-based geometry shows peak fibrous cap stress of approx. 54 kPa. With the inclusion of pathological features such as micro-Ca of the fibrous cap, the stresses increase substantially but do not reach the predefined rupture stress range (approx. 90 kPa for micro-Ca case). From this data, we assert that micro-Ca, among other factors yet to be identified, have a significant role in VP progression and clinical sequelae. Other

factors not incorporated into this model, such as collagen fiber orientation of the fibrous cap as it relates to altered stretching of the fibrous cap body, may play a role in alteration of the dynamic stress levels. Fibrous cap anisotropy may have a wider role in VP pathogenesis, fibrous cap rupture and thrombus formation and its incorporation into FSI models may ultimately provide a more accurate measure of rupture potential and we are planning to investigate in our future studies.

We show how micro-Ca can increase fibrous cap stresses, potentially increasing the risk of rupture of the fibrous cap. Our analysis of micro-Ca uses a unique combination of micro-CT and FSI methodologies, and the results are similar to what has been previously observed by our group in VP [19] and abdominal aortic aneurysms - AAA [54, 86]. For both VP and AAA, calcified inclusions have been shown to increase vessel wall stresses. Our observation of similar findings with micro-Ca is confirmed at the microscopic level with the observed bipolar stress distribution around the micro-Ca. Our observations in coronary plaques are derived using material properties for coronary vessels based on biaxial mechanical testing [53], and agree with recent literature associated with both intimal fibrous cap micro-Ca [20, 23] and fibrous cap material studies [38]. This study benefits from the powerful combination of highly resolved micro-CT and extremely fine numerical mesh for FSI simulations that enabled capturing the fine details of the various VP components, down to the level of the micro-Ca that are embedded within the VP thin fibrous cap. It clearly demonstrates that this micro-Ca generate distinct localized regions of elevated stress concentrations that increase the plaque burden and eventually may lead to its rupture. Further studies would be required to establish statistical significance with a cohort of pathological VP cases for ascertaining semi-quantitative predictions of plaque rupture. Actually, in the 2006 paper by Vengrenyuk et al only 5 vulnerable plaque were

observed in a sample of 24 examined, and only one of the five vulnerable lesions observed had cellular size microcalcifications in the cap. There is a much larger ongoing study by Weinbaum group involving 92 coronary arteries from victims dying of coronary artery disease. In that study, 62 vessels were found with vulnerable lesion and 15% of these plaques had cellular size microCa in the fibrous cap. These microCT results will be made available to us once the paper is accepted for publication. As demonstrated by the methodology, determination of rupture risk of coronary plaques is still limited by available imaging modalities, which currently do not offer the degree of resolution to capture micro-Ca embedded in the fibrous cap *in vivo*. However, with further advances in imaging, evaluation of coronary plaque rupture potential via high resolution intraluminal imaging modalities combined with FSI modeling may become a staple in clinical practice.

Analyzing the principal stress distribution at cross sections, stress concentrations can be observed around the micro-Ca in the direction of the applied load at the poles of the inclusions. We observed poles of compressive and tensile stresses at each one of the micro-Ca embedded in the fibrous cap. The compressive poles (shown in blue, Figure 22) are on the radial direction of the vessel whereas the tensile poles (shown in red, Figure 22) are on the circumferential direction. These bipolar stress distributions have hypothesized [20, 23, 68] to lead to the debonding of the rigid inclusion causing a rupture of the fibrous cap. The analytical model proposed by Vengrenyuk et al. predicts that the presence of a rigid spherical inclusion will increase the local stress surrounding the micro-Ca by two-fold at the poles in the direction of tension, where the cavitation stress bubbles and detachment of the soft tissue from the surface of the inclusion are most likely to occur. For present study, the comparison between the FSI simulation and the detailed FEM results in Vengrenyuk et al 2008 on the same artery was the

main purpose and it further incorporates the fluid aspects of the problem. Furthermore, the debonding process, which destabilizes the fibrous cap, has been shown to be highly dependent on the size of the inclusion [20, 23, 68] as also observed in our FSI simulations. More specifically, significant differences arose from using different size meshes. In the present results the average stress at the inclusion interface is increased by a factor of two and there is a fivefold increase at the poles of the inclusion, whereas in Vengrenyuk et al the peak circumferential stress PCS is increased by a factor of two only at the tensile poles of the inclusion. There is also little increase in PCS with the size of the microinclusion in the FEM model, whereas the FSI calculation shows a decrease in Von Mises stress with increase in particle size.

### **Conclusions:**

In the IVUS VP study, it incorporates several major biomechanical factors associated with coronary vulnerable plaque risk assessment and elucidates the feasibility of IVUS based patient specific FSI methodologies. It was verified that von Mises stress would exponentially increase with fibrous caps thinner than  $65 \mu\text{m}$ . Stress distributions in the vessel respond linearly to the elevation of pressure. This finding implies that plaque stability can be determined accurately for coronary vulnerable plaque patients with hypertension. Furthermore, the appearance of microscopic level calcified spot in the lesion dramatically destabilizes the fibrous cap. Stress-driven reorientation and biochemically degradation of the collagen fibers in the vessel due to atherosclerosis would result in an anisotropic fibrous cap with  $65^\circ$  degree fiber angles. It was found that the critical stress values were much higher within such a diseased fibrous cap, especially, when micro-Ca was included as well. FSI simulations from patient reconstructed VP mapping the wall stresses while analyzing the impact of biomechanical factors investigated in the study can be used as an additional diagnostic measure to help clinicians



determine the rupture risk and the need for intervention. Particularly, in the Micro-CT VP study, we also affirm the feasibility of the 'micro-CT to FSI' approach for assessing vulnerable plaque rupture potential in realistic patient based vulnerable plaque. Especially, we were able to capture and pinpoint the location of the microcalcification in the fibrous cap. We present dynamic fibrous cap wall stress mapping while assessing the role of micro-Ca and phase lag. Micro-Ca embedded in the fibrous cap produces increased stresses that correspond to a new hypothesis for vulnerable plaque rupture resulting from micro-CA in the VP fibrous cap, and predict stress levels that can definitely lead to VP rupture. Further advancement of the 'micro-CT to FSI' methodology may offer better diagnostic tools for clinicians, while reducing morbidity and mortality rates for patients with vulnerable plaques and curtailing the ensuing healthcare costs.

## References:

1. Marques, K.M., et al., *The diastolic flow-pressure gradient relation in coronary stenoses in humans*. J Am Coll Cardiol, 2002. **39**(10): p. 1630-6.
2. Yusuf, S., et al., *Global burden of cardiovascular diseases: Part II: variations in cardiovascular disease by specific ethnic groups and geographic regions and prevention strategies*. Circulation, 2001. **104**(23): p. 2855-64.
3. Lloyd-Jones, D., et al., *Heart disease and stroke statistics--2010 update: a report from the American Heart Association*. Circulation, 2010. **121**(7): p. e46-e215.
4. Zipes, D.P. and H.J. Wellens, *Sudden cardiac death*. Circulation, 1998. **98**(21): p. 2334-51.
5. Hansson, G.K., *Inflammation, atherosclerosis, and coronary artery disease*. N Engl J Med, 2005. **352**(16): p. 1685-95.
6. Saba, L., et al., *Imaging of the fibrous cap in atherosclerotic carotid plaque*. Cardiovasc Intervent Radiol, 2010. **33**(4): p. 681-9.
7. Burke, A.P., et al., *Coronary risk factors and plaque morphology in men with coronary disease who died suddenly*. N Engl J Med, 1997. **336**(18): p. 1276-82.
8. Virmani, R., et al., *Pathology of the unstable plaque*. Prog Cardiovasc Dis, 2002. **44**(5): p. 349-56.
9. Burke, A.P., et al., *Effect of risk factors on the mechanism of acute thrombosis and sudden coronary death in women*. Circulation, 1998. **97**(21): p. 2110-6.
10. Virmani, R., et al., *Pathology of the vulnerable plaque*. J Am Coll Cardiol, 2006. **47**(8 Suppl): p. C13-8.
11. Blank, A., et al., *Miniature self-contained intravascular magnetic resonance (IVMI) probe for clinical applications*. Magn Reson Med, 2005. **54**(1): p. 105-12.
12. Burke, A.P., et al., *Pathophysiology of calcium deposition in coronary arteries*. Herz, 2001. **26**(4): p. 239-44.
13. Kolodgie, F.D., et al., *The thin-cap fibroatheroma: a type of vulnerable plaque: the major precursor lesion to acute coronary syndromes*. Curr Opin Cardiol, 2001. **16**(5): p. 285-92.
14. Kolodgie, F.D., et al., *Pathologic assessment of the vulnerable human coronary plaque*. Heart, 2004. **90**(12): p. 1385-91.
15. Virmani, R., et al., *Pathology of the Thin-Cap Fibroatheroma: A Type of Vulnerable Plaque*. Journal of Interventional Cardiology, 2003. **16**(3): p. 267-272.
16. Loree, H.M., et al., *Static circumferential tangential modulus of human atherosclerotic tissue*. J Biomech, 1994. **27**(2): p. 195-204.
17. DeWood, M.A., et al., *Prevalence of total coronary occlusion during the early hours of transmural myocardial infarction*. N Engl J Med, 1980. **303**(16): p. 897-902.
18. Dhume, A.S., et al., *Comparison of vascular smooth muscle cell apoptosis and fibrous cap morphology in symptomatic and asymptomatic carotid artery disease*. Ann Vasc Surg, 2003. **17**(1): p. 1-8.
19. Bluestein, D., et al., *Influence of microcalcifications on vulnerable plaque mechanics using FSI modeling*. J Biomech, 2008. **41**(5): p. 1111-8.
20. Vengrenyuk, Y., et al., *A hypothesis for vulnerable plaque rupture due to stress-induced debonding around cellular microcalcifications in thin fibrous caps*. Proc Natl Acad Sci U S A, 2006. **103**(40): p. 14678-83.
21. Huang, H., et al., *The impact of calcification on the biomechanical stability of atherosclerotic plaques*. Circulation, 2001. **103**(8): p. 1051-1056.
22. Imoto, K., et al., *Longitudinal structural determinants of atherosclerotic plaque vulnerability - A computational analysis of stress distribution using vessel models and three-dimensional*

- intravascular ultrasound imaging*. Journal Of The American College Of Cardiology, 2005. **46**(8): p. 1507-1515.
23. Vengrenyuk, Y., L. Cardoso, and S. Weinbaum, *Micro-CT based analysis of a new paradigm for vulnerable plaque rupture: cellular microcalcifications in fibrous caps*. Mol Cell Biomech, 2008. **5**(1): p. 37-47.
  24. Madhavan, S., et al., *Relation of pulse pressure and blood pressure reduction to the incidence of myocardial infarction*. Hypertension, 1994. **23**(3): p. 395-401.
  25. Benetos, A., et al., *Pulse pressure: a predictor of long-term cardiovascular mortality in a French male population*. Hypertension, 1997. **30**(6): p. 1410-5.
  26. Dobrin, P.B., *Pathophysiology and pathogenesis of aortic aneurysms. Current concepts*. Surg Clin North Am, 1989. **69**(4): p. 687-703.
  27. Gasser, T.C., R.W. Ogden, and G.A. Holzapfel, *Hyperelastic modelling of arterial layers with distributed collagen fibre orientations*. Journal of the Royal Society Interface, 2006. **3**(6): p. 15-35.
  28. Libby, P., P.M. Ridker, and A. Maseri, *Inflammation and atherosclerosis*. Circulation, 2002. **105**(9): p. 1135-43.
  29. Moreno, P.R., et al., *Macrophage infiltration in acute coronary syndromes. Implications for plaque rupture*. Circulation, 1994. **90**(2): p. 775-8.
  30. Holzapfel, G., M. Stadler, and T.C. Gasser, *Changes in the mechanical environment of stenotic arteries during interaction with stents: Computational assessment of parametric stent designs*. Journal of Biomechanical Engineering-Transactions of the Asme, 2005. **127**(1): p. 166-180.
  31. Holzapfel, G.A., *Nonlinear Solid Mechanics: A Continuum Approach For Engineering*. 2000, Chichester: John Wiley & Sons Ltd.
  32. Holzapfel, G.A. and T.C. Gasser, *A viscoelastic model for fiber-reinforced composites at finite strains: Continuum basis, computational aspects and applications*. Computer Methods in Applied Mechanics and Engineering, 2001. **190**(34): p. 4379-4403.
  33. Holzapfel, G.A. and T.C. Gasser, *Computational stress-deformation analysis of arterial walls including high-pressure response*. International Journal of Cardiology, 2007. **116**(1): p. 78-85.
  34. Holzapfel, G.A., T.C. Gasser, and R.W. Ogden, *A new constitutive framework for arterial wall mechanics and a comparative study of material models*. Journal of Elasticity, 2000. **61**(1-3): p. 1-48.
  35. Holzapfel, G.A., T.C. Gasser, and R.W. Ogden, *Comparison of a multi-layer structural model for arterial walls with a fung-type model, and issues of material stability*. Journal of Biomechanical Engineering-Transactions of the Asme, 2004. **126**(2): p. 264-275.
  36. Holzapfel, G.A., T.C. Gasser, and M. Stadler, *A structural model for the viscoelastic behavior of arterial walls: Continuum formulation and finite element analysis*. European Journal of Mechanics a-Solids, 2002. **21**(3): p. 441-463.
  37. Sacks, M.S., et al., *In vivo three-dimensional surface geometry of abdominal aortic aneurysms*. Ann Biomed Eng, 1999. **27**(4): p. 469-79.
  38. Holzapfel, G.A., et al., *Determination of layer-specific mechanical properties of human coronary arteries with nonatherosclerotic intimal thickening and related constitutive modeling*. American Journal of Physiology-Heart and Circulatory Physiology, 2005. **289**(5): p. H2048-H2058.
  39. Baldewising, R.A., et al., *A finite element model for performing intravascular ultrasound elastography of human atherosclerotic coronary arteries*. Ultrasound In Medicine And Biology, 2004. **30**(6): p. 803-813.
  40. Gasser, T.C. and G.A. Holzapfel, *Geometrically non-linear and consistently linearized embedded strong discontinuity models for 3D problems with an application to the dissection analysis of soft*

- biological tissues*. Computer Methods in Applied Mechanics and Engineering, 2003. **192**(47-48): p. 5059-5098.
41. Gasser, T.C. and G.A. Holzapfel, *A rate-independent elastoplastic constitutive model for biological fiber-reinforced composites at finite strains: continuum basis, algorithmic formulation and finite element implementation*. Computational Mechanics, 2002. **29**(4-5): p. 340-360.
  42. Gasser, T.C. and G.A. Holzapfel, *Modeling the propagation of arterial dissection*. European Journal of Mechanics a-Solids, 2006. **25**(4): p. 617-633.
  43. Gasser, T.C. and G.A. Holzapfel, *3D Crack propagation in unreinforced concrete. A two-step algorithm for tracking 3D crack paths*. Computer Methods in Applied Mechanics and Engineering, 2006. **195**(37-40): p. 5198-5219.
  44. Gasser, T.C. and G.A. Holzapfel, *Modeling plaque fissuring and dissection during balloon angioplasty intervention*. Annals of Biomedical Engineering, 2007. **35**(5): p. 711-723.
  45. Gasser, T.C. and G.A. Holzapfel, *Finite element modeling of balloon angioplasty by considering overstretch of remnant non-diseased tissues in lesions*. Computational Mechanics, 2007. **40**(1): p. 47-60.
  46. Deguchi, J.O., et al., *Matrix metalloproteinase-13/collagenase-3 deletion promotes collagen accumulation and organization in mouse atherosclerotic plaques*. Circulation, 2005. **112**(17): p. 2708-15.
  47. Hariton, I., et al., *Stress-modulated collagen fiber remodeling in a human carotid bifurcation*. Journal of Theoretical Biology, 2007. **248**(3): p. 460-470.
  48. Hariton, I., et al., *Stress-driven collagen fiber remodeling in arterial walls*. Biomechanics and Modeling in Mechanobiology, 2007. **6**(3): p. 163-175.
  49. Nair, A., D. Calvetti, and D.G. Vince, *Regularized autoregressive analysis of intravascular ultrasound backscatter: improvement in spatial accuracy of tissue maps*. IEEE Trans Ultrason Ferroelectr Freq Control, 2004. **51**(4): p. 420-31.
  50. Nair, A., et al., *Assessing spectral algorithms to predict atherosclerotic plaque composition with normalized and raw intravascular ultrasound data*. Ultrasound Med Biol, 2001. **27**(10): p. 1319-31.
  51. Nair, A., et al., *Coronary plaque classification with intravascular ultrasound radiofrequency data analysis*. Circulation, 2002. **106**(17): p. 2200-6.
  52. Tang, D., et al., *3D MRI-based multicomponent FSI models for atherosclerotic plaques*. Ann Biomed Eng, 2004. **32**(7): p. 947-60.
  53. Yang, C., et al., *In vivo IVUS-based 3-D fluid-structure interaction models with cyclic bending and anisotropic vessel properties for human atherosclerotic coronary plaque mechanical analysis*. IEEE Trans Biomed Eng, 2009. **56**(10): p. 2420-8.
  54. Xenos, M., et al., *Patient-Based Abdominal Aortic Aneurysm Rupture Risk Prediction with Fluid Structure Interaction Modeling*. Ann Biomed Eng, 2010. **38**(11): p. 3323-3337.
  55. Xenos, M., et al., *The effect of angulation in abdominal aortic aneurysms: fluid-structure interaction simulations of idealized geometries*. Med Biol Eng Comput, 2010. **48**(12): p. 1175-90.
  56. Holzapfel, G.A., G. Sommer, and P. Regitnig, *Anisotropic mechanical properties of tissue components in human atherosclerotic plaques*. J Biomech Eng, 2004. **126**(5): p. 657-65.
  57. Gasser, T.C. and G.A. Holzapfel, *Modeling plaque fissuring and dissection during balloon angioplasty intervention*. Ann Biomed Eng, 2007. **35**(5): p. 711-23.
  58. Liu, B. and D. Tang, *Influence of non-Newtonian properties of blood on the wall shear stress in human atherosclerotic right coronary arteries*. Mol Cell Biomech, 2011. **8**(1): p. 73-90.
  59. Tang, D., et al., *Effect of a lipid pool on stress/strain distributions in stenotic arteries: 3-D fluid-structure interactions (FSI) models*. J Biomech Eng, 2004. **126**(3): p. 363-70.

60. Tang, D., et al., *Local maximal stress hypothesis and computational plaque vulnerability index for atherosclerotic plaque assessment*. Ann Biomed Eng, 2005. **33**(12): p. 1789-801.
61. Tang, D., et al., *Quantifying effects of plaque structure and material properties on stress distributions in human atherosclerotic plaques using 3D FSI models*. J Biomech Eng, 2005. **127**(7): p. 1185-1194.
62. Tang, D., et al., *Simulating cyclic artery compression using a 3D unsteady model with fluid-structure interactions*. Computers & Structures, 2002. **80**(20-21): p. 1651-1665.
63. Rodriguez, J.F., et al., *Mechanical stresses in abdominal aortic aneurysms: influence of diameter, asymmetry, and material anisotropy*. J Biomech Eng, 2008. **130**(2): p. 021023.
64. Ma, B., et al., *Nonlinear anisotropic stress analysis of anatomically realistic cerebral aneurysms*. J Biomech Eng, 2007. **129**(1): p. 88-96.
65. Dahl, S.L., M.E. Vaughn, and L.E. Niklason, *An ultrastructural analysis of collagen in tissue engineered arteries*. Ann Biomed Eng, 2007. **35**(10): p. 1749-55.
66. Watton, P.N. and N.A. Hill, *Evolving mechanical properties of a model of abdominal aortic aneurysm*. Biomech Model Mechanobiol, 2009. **8**(1): p. 25-42.
67. Kajiyama, F., et al., *Analysis of flow characteristics in poststenotic regions of the human coronary artery during bypass graft surgery*. Circulation, 1987. **76**(5): p. 1092-100.
68. Gent, A.N. and B. Park, *Failure Processes in Elastomers at or near a Rigid Spherical Inclusion*. Journal of Materials Science, 1984. **19**(6): p. 1947-1956.
69. Tang, D., et al., *Sites of rupture in human atherosclerotic carotid plaques are associated with high structural stresses: an in vivo MRI-based 3D fluid-structure interaction study*. Stroke, 2009. **40**(10): p. 3258-63.
70. Finet, G., J. Ohayon, and G. Rioufol, *Biomechanical interaction between cap thickness, lipid core composition and blood pressure in vulnerable coronary plaque: impact on stability or instability*. Coronary Artery Disease, 2004. **15**(1): p. 13-20.
71. Loree, H.M., et al., *Effects of fibrous cap thickness on peak circumferential stress in model atherosclerotic vessels*. Circ Res, 1992. **71**(4): p. 850-8.
72. Cheng, G.C., et al., *Distribution Of Circumferential Stress In Ruptured And Stable Atherosclerotic Lesions - A Structural-Analysis With Histopathological Correlation*. Circulation, 1993. **87**(4): p. 1179-1187.
73. Giachelli, C.M., *Vascular calcification mechanisms*. J Am Soc Nephrol, 2004. **15**(12): p. 2959-64.
74. Holzapfel, G.A., M. Stadler, and C.A. Schulze-Bauer, *A layer-specific three-dimensional model for the simulation of balloon angioplasty using magnetic resonance imaging and mechanical testing*. Ann Biomed Eng, 2002. **30**(6): p. 753-67.
75. Holzapfel, G.A. and H.W. Weizsacker, *Biomechanical behavior of the arterial wall and its numerical characterization*. Computers in Biology and Medicine, 1998. **28**(4): p. 377-392.
76. Schulze-Bauer, C.A. and G.A. Holzapfel, *Determination of constitutive equations for human arteries from clinical data*. J Biomech, 2003. **36**(2): p. 165-9.
77. Schulze-Bauer, C.A., P. Regitnig, and G.A. Holzapfel, *Mechanics of the human femoral adventitia including the high-pressure response*. Am J Physiol Heart Circ Physiol, 2002. **282**(6): p. H2427-40.
78. Sommer, G., et al., *Dissection properties of the human aortic media: An experimental study*. Journal of Biomechanical Engineering-Transactions of the Asme, 2008. **130**(2): p. -.
79. Zohdi, T.I., G.A. Holzapfel, and S.A. Berger, *A phenomenological model for atherosclerotic plaque growth and rupture*. Journal Of Theoretical Biology, 2004. **227**(3): p. 437-443.
80. Kuhl, E., et al., *Remodeling of biological tissue: Mechanically induced reorientation of a transversely isotropic chain network*. Journal of the Mechanics and Physics of Solids, 2005. **53**(7): p. 1552-1573.

81. Vande Geest, J.P., et al., *A biomechanics-based rupture potential index for abdominal aortic aneurysm risk assessment: demonstrative application*. Ann N Y Acad Sci, 2006. **1085**: p. 11-21.
82. Vande Geest, J.P., M.S. Sacks, and D.A. Vorp, *The effects of aneurysm on the biaxial mechanical behavior of human abdominal aorta*. J Biomech, 2006. **39**(7): p. 1324-1334.
83. Thim, T., et al., *From vulnerable plaque to atherothrombosis*. J Intern Med, 2008. **263**(5): p. 506-16.
84. Samady, H., et al., *Coronary artery wall shear stress is associated with progression and transformation of atherosclerotic plaque and arterial remodeling in patients with coronary artery disease*. Circulation, 2011. **124**(7): p. 779-88.
85. Cheng, C., et al., *Atherosclerotic lesion size and vulnerability are determined by patterns of fluid shear stress*. Circulation, 2006. **113**(23): p. 2744-53.
86. Xenos, M., et al., *Patient based Abdominal Aortic Aneurysm rupture risk prediction combining clinical visualizing modalities with fluid structure interaction numerical simulations*. Conf Proc IEEE Eng Med Biol Soc, 2010. **1**: p. 5173-6.

## Appendix:

Derivation of Cauchy stresses as stretches vary in different directions from both isotropic and anisotropic Mooney-Rivlin strain energy functions.

Strain Energy Function

### *Isotropic Formulation*

$$\bar{\psi} = C_1(I_1 - 3) + D_1[\exp(D_2(I_1 - 3)) - 1]$$

$$I_1 = \text{tr}(C_{ij}), \quad I_2 = \frac{1}{2}[I_1^2 - C_{ij}C_{ij}], \quad J = \lambda_1\lambda_2\lambda_3 = \det F$$

$\lambda_\alpha$  ( $\alpha = 1, 2, 3$ ) Principle Stretches

Second Piola-Kirchhoff Stress

$$S = 2 \frac{\partial \bar{\psi}}{\partial C} = 2 \left[ \frac{\partial \bar{\psi}}{\partial I_1} \frac{\partial I_1}{\partial C} \right]$$

Cauchy Stress Tensor

$$\begin{bmatrix} \frac{1}{\lambda_z^2 \lambda_\theta^2} & 0 & 0 \\ 0 & \frac{1}{\lambda_\theta^2} & 0 \\ 0 & 0 & \frac{1}{\lambda_z^2} \end{bmatrix}$$

$$I_1 = \text{trace}[C_{\text{tensor}}] = \lambda_z^2 + \frac{1}{\lambda_z^2 \lambda_\theta^2} + \lambda_\theta^2$$

$$\frac{\partial I_1}{\partial C} = \frac{\partial \text{tr} C}{\partial C} = \mathbf{I}$$

$$\begin{aligned} S &= 2(C_1 + D_1 D_2 (I_1 - 3)) e^{D_2 (I_1 - 3)} \\ &= 2(C_1 + D_1 D_2 (I_1 - 3)) e^{D_2 (-3 + \lambda_z^2 + \frac{1}{\lambda_z^2 \lambda_\theta^2} + \lambda_\theta^2)} \quad \square \end{aligned}$$

Cauchy Stress :  $\sigma = \mathbf{F} \mathbf{S} \mathbf{F}^T$

$$\sigma_{\text{axial}} = \sigma_{\text{circum}} = \frac{2(C_1 + D_1 D_2 (I_1 - 3)) e^{D_2 (-3 + \lambda_z^2 + \frac{1}{\lambda_z^2 \lambda_\theta^2} + \lambda_\theta^2)}}{\lambda_z^2 \lambda_\theta^2}$$

### Anisotropic Formulation

$$\bar{\psi} = C_1 (I_1 - 3) + D_1 \left[ e^{(D_2 (I_1 - 3))} - 1 \right] + \frac{k_1}{2k_2} \left[ e^{k_2 (I_4 - 1)^2 - 1} \right]$$

$\lambda_\alpha$  ( $\alpha = 1, 2, 3$ ) Principle Stretches

Second Piola-Kirchhoff Stress

$$\mathbf{S} = 2 \frac{\partial \bar{\psi}}{\partial C} = 2 \left[ \frac{\partial \bar{\psi}}{\partial I_1} \frac{\partial I_1}{\partial C} + \frac{\partial \bar{\psi}}{\partial I_4} \frac{\partial I_4}{\partial C} \right]$$

Cauchy Stress Tensor

$$\begin{bmatrix} \frac{1}{\lambda_2^2 \lambda_3^2} & 0 & 0 \\ 0 & \lambda_2^2 & 0 \\ 0 & 0 & \lambda_3^2 \end{bmatrix}$$

Invariants:

$$I_1 = \text{trace}[C_{\text{tensor}}] = \lambda_3^2 + \frac{1}{\lambda_3^2 \lambda_2^2} + \lambda_2^2$$

$\text{tr} = \text{trace}$



$$I_2 = \frac{1}{2} \left[ (\text{tr}(C_{tensor}))^2 - (\text{tr}(C_{tensor}^2)) \right] = \lambda_l^2 \lambda_\theta^2 + \lambda_l^2 \lambda_z^2 + \lambda_z^2 \lambda_\theta^2$$

$$I_3 = \det(C_{tensor}) = J^2 = \lambda_l^2 \lambda_\theta^2 \lambda_z^2$$

$$I_4 = \frac{\cos(\alpha)^2}{\lambda_\theta^2 \lambda_z^2} + \lambda_\theta^2 \sin(\alpha)^2$$

Where

$$\text{Fiber Angle Matrix } a = \begin{bmatrix} \cos(\alpha) \\ \sin(\alpha) \\ 0 \end{bmatrix}$$

Derivatives of the invariants

$$\frac{\partial I_1}{\partial C_{tensor}} = \frac{\partial \text{tr} C_{tensor}}{\partial C_{tensor}} = \mathbf{I}$$

where  $\mathbf{I}$  = Identity Matrix

$$\frac{\partial I_2}{\partial C_{tensor}} = \frac{1}{2} \left( 2C_{tensor} \mathbf{I} - \frac{\partial \text{tr}(C_{tensor}^2)}{\partial C_{tensor}} \right) = I_1 \mathbf{I} - C_{tensor}$$

$$\frac{\partial I_3}{\partial C_{tensor}} = I_3 C_{tensor}^{-1}$$

$$\frac{\partial I_4}{\partial C_{tensor}} = A_0 = a \otimes a = \begin{bmatrix} \cos \alpha \\ \sin \alpha \\ 0 \end{bmatrix} \begin{bmatrix} \cos \alpha & \sin \alpha & 0 \end{bmatrix} = \begin{bmatrix} \cos(\alpha)^2 & \cos(\alpha) \sin(\alpha) & 0 \\ \cos(\alpha) \sin(\alpha) & \sin(\alpha)^2 & 0 \\ 0 & 0 & 0 \end{bmatrix}$$

$$\frac{\partial \bar{\psi}}{\partial I_1} = C_1 + D_1 e^{[D_2(I_1-3)]}$$

$$\frac{\partial \bar{\psi}}{\partial I_4} = k_1 (I_4 - 1) e^{[k_2(I_4-1)^2-1]}$$

So,

$$\begin{aligned} S &= 2 \left[ \frac{\partial \bar{\psi}}{\partial C} \right] = 2 \left[ \frac{\partial \bar{\psi}}{\partial I_1} \frac{\partial I_1}{\partial C} + \frac{\partial \bar{\psi}}{\partial I_4} \frac{\partial I_4}{\partial C} \right] \\ &= \begin{bmatrix} 2 \left[ C_1 + D_1 e^{[D_2(I_1-3)]} + k_1 (I_4 - 1) e^{[k_2(I_4-1)^2-1]} \right] \left[ \cos(\alpha)^2 + \sin(\alpha) \cos(\alpha) \right] \\ 2 \left[ C_1 + D_1 e^{[D_2(I_1-3)]} + k_1 (I_4 - 1) e^{[k_2(I_4-1)^2-1]} \right] \left[ \sin(\alpha)^2 + \cos(\alpha) \sin(\alpha) \right] \\ 2 \left[ C_1 + D_1 e^{[D_2(I_1-3)]} \right] \end{bmatrix} \end{aligned}$$

Cauchy\_Stress\_Tensor  $C_{\text{tensor}}$

$$\sigma = F S F^T$$

$$\text{where } F = \begin{bmatrix} \frac{1}{\lambda_2^2 \lambda_3^2} & 0 & 0 \\ 0 & \frac{1}{\lambda_2^2} & 0 \\ 0 & 0 & \frac{1}{\lambda_3^2} \end{bmatrix}$$

Finally,

$$\sigma_{axial} = 2 \left[ C_1 + D_1 e^{[D_2(I_1-3)]} + k_1 (I_4 - 1) e^{[k_2(I_4-1)^2-1]} \right] \left[ \cos(\alpha)^2 + \sin(\alpha) \cos(\alpha) \right]$$

$$\sigma_{circum} = 2 \left[ C_1 + D_1 e^{[D_2(I_1-3)]} \right] + k_1 (I_4 - 1) e^{[k_2(I_4-1)^2-1]} \left[ \sin(\alpha)^2 + \cos(\alpha) \sin(\alpha) \right]$$

$$\sigma_{longitudinal} = 2 \left[ C_1 + D_1 e^{[D_2(I_1-3)]} \right]$$

By incorporating different fiber orientations, the Cauchy stress/stretch figures reveal better understanding of the anisotropic Mooney-Rivlin material model. As shown in Figure 24

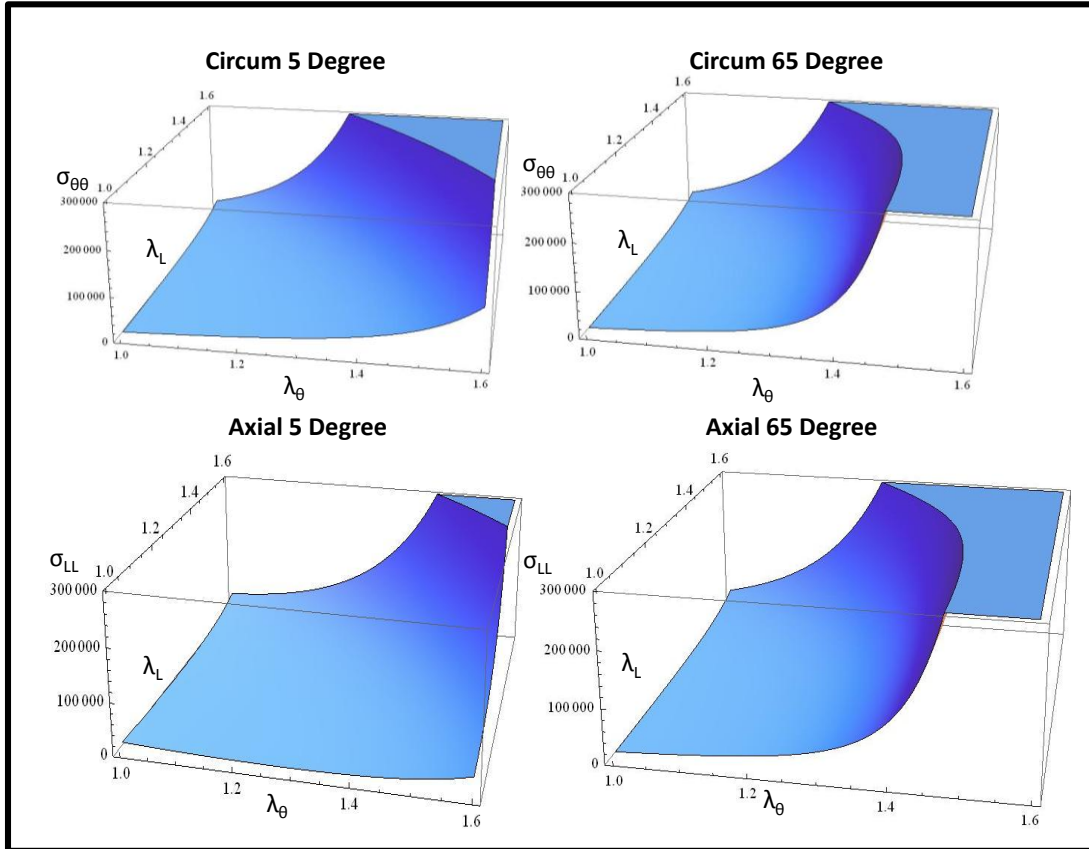


**Figure 24. Cauchy stress versus the axial and circumferential stretches for fibrous cap anisotropic material properties. The mechanical response predicted from the constitutive model shows apparent stiffening in vessel with 65 degree fiber orientation compared to 5 degree fiber orientation.**

### Matlab Code for Curve Fitting the Pressure and Flow boundary Conditions

Matlab code developed was useful in fitting the pressure and flow boundary conditions.

This code uses multiple higher order curve fitting formulations, such as Fourier, Hermite, and Chebyshev polynomial fitting, to fit the boundary condition waveforms taken from clinical literature. Waveforms generated based on fitting are shown below.

```
function SquareFit_Pressure_Data
clc;
clear;

% -----
fid2=fopen('Pressure_output.dat','w');
% -----

load -ascii Pressure.dat
basilar_beat_v2 = Pressure

% load -ascii Pulse_4ventricle.dat
% basilar_beat_v2 = Pulse_4ventricle

N = size(Pressure)
% -----

%Data generated Using the function  $y=1.3 + \cos(x) - 0.5 * \sin(2 * x)$ 

for i = 1 : N
    x(i) = Pressure(i,1);
    y(i) = Pressure(i,2);
end

figure(1)
hold on
for i = 1 : N
    plot(x(i),y(i),'o')
end
hold off
%axis([0.0 1.0 -1.0 1.2])
% -----
weight= [1. 1. 1. 1. 1. 1. 1. 1. 1. 1. 1. 1.];

% weight= [0.5 0.5 0.3 0.3 0.9 0.9 0.5 0.2 0.2 0.2 0.2 0.9 0.9 0.9 0.9 0.8
0.2 0.2 0.2 0.2 0.2 0.3 0.3 0.3 0.3 0.3 ...
%           0.5 0.5 0.5 0.5 0.5 0.5];

for i = 1 : N
    w(i,i) = weight(i);
end

w;

% -----
% ----- number of terms used in the polynomial -----
```

```

number = 8

for j = 1 : N
    BF(j,:) = FourierPoly(x(j),number);
    Bc(j,:) = ChevyshevPoly(x(j));
    Bh(j,:) = HermitePoly(x(j));
end

BF;

AF=BF'*BF; %Coefficient Matrix
YF=BF'*y'; %Right Side

Ac=Bc'*Bc; %Coefficient Matrix
Yc=Bc'*y'; %Right Side

Ah=Bh'*Bh; %Coefficient Matrix
Yh=Bh'*y'; %Right Side

aF=AF\YF % Linear solver for the Coefficients
ac=Ac\Yc; % Linear solver for the Coefficients
ah=Ah\Yh; % Linear solver for the Coefficients

for i=1 : N
    pnF(i)=aF'*FourierPoly(x(i),number)'; % Calculate fitted data
    pnc(i)=ac'*ChevyshevPoly(x(i))'; % Calculate fitted data
    pnh(i)=ah'*HermitePoly(x(i))'; % Calculate fitted data
end

syms X;

Pnc(1)=ac(1)*sym(1);
Pnc(2)=ac(2)*sym(X);
Pnc(3)=ac(3)*sym(2*X^2-1);
Pnc(4)=ac(4)*sym(4*X^3-3*X);
Pnc(5)=ac(5)*sym(16*X^5-20*X^3+5*X);

%Pnc(6)=ac(6)*sym(32*X^6-48*X^4+18*X^2-1);
%Pnc(7)=ac(7)*sym(64*X^7-112*X^5+56*X^3-7*X);

PNc=sum(Pnc);
CoeffC=sym2poly(PNc);

Pnh(1)=ah(1)*sym(1);
Pnh(2)=ah(2)*sym(2*X);
Pnh(3)=ah(3)*sym(4*X^2-2);
Pnh(4)=ah(4)*sym(8*X^3-12*X);
Pnh(5)=ah(5)*sym(16*X^4-48*X+12);

PNh=sum(Pnh);
CoeffH=sym2poly(PNh);

AwF=BF'*w*BF; %Coefficient weighted Matrix
YwF=BF'*w*y'; % Weighted Right Side

```

```

Awc=Bc'*w*Bc; %Coefficient weighted Matrix
Ywc=Bc'*w*y'; % Weighted Right Side

Awh=Bh'*w*Bh; %Coefficient weighted Matrix
Ywh=Bh'*w*y'; % Weighted Right Side

awF=AwF\YwF; % Linear solver for the Coefficients
awc=Awc\Ywc; % Linear solver for the Coefficients
awh=Awh\Ywh; % Linear solver for the Coefficients

for i=1 : N
    pnwF(i)=awF'*FourierPoly(x(i),number)';% Calculate fitted data
    pnwc(i)=awc'*ChevyshevPoly(x(i))';% Calculate fitted data
    pnwh(i)=awh'*HermitePoly(x(i))';% Calculate fitted data
end

t= 0.2 : 0.01 : 1.0;

for i = 1 : length(t)
    tpnwF(i)=awF'*FourierPoly(t(i),number)';% Calculate fitted data
    tpnwc(i)=awc'*ChevyshevPoly(t(i))';% Calculate fitted data
    tpnwh(i)=awh'*HermitePoly(t(i))';% Calculate fitted data
end

for i = 1 : length(t)
    fprintf(fid2,'%10.2f %10.2f \n', t(i), tpnwF(i));
end

figure(2);
plot(x,y,'o',t,tpnwF)
legend('data','Fourier Aproximation') % ,'Weighted Legendre Poly
Aproximation')
%axis([0.0 2.0 -1.0 1.2])

%legend('Location','SE')
%text(4,6,['Eq= ' num2str(CoeffF(1), '%6.4f ') '+' num2str(CoeffF(2),
'%6.4f') '*x +' num2str(CoeffF(3), '%6.4f ') '*x^2 +' num2str(CoeffF(4),
'%6.4f ') '*x^3 +' num2str(CoeffF(5), '%6.4f ') '*x^4'])
%text(4,5.5,['EqWeighted= ' num2str(CoeffwF(1), '%6.4f ') '+'
num2str(CoeffwF(2), '%6.4f') '*x +' num2str(CoeffwF(3), '%6.4f ') '*x^2 +'
num2str(CoeffwF(4), '%6.4f ') '*x^3'])
title('Fourier Polynomial Approximation')
xlabel('x')
ylabel('y')

figure(3);
plot(t,tpnwF,'g')
legend('Fourier Approximation') % ,'Weighted Legendre Poly Aproximation')
%axis([0.0 2.0 -1.0 1.2])

%legend('Location','SE')
%text(4,6,['Eq= ' num2str(CoeffF(1), '%6.4f ') '+' num2str(CoeffF(2),
'%6.4f') '*x +' num2str(CoeffF(3), '%6.4f ') '*x^2 +' num2str(CoeffF(4),
'%6.4f ') '*x^3 +' num2str(CoeffF(5), '%6.4f ') '*x^4'])

```

```

%text(4,5.5,['EqWeighted= ' num2str(CoeffwF(1), '%6.4f ') '+'
num2str(CoeffwF(2), '%6.4f') '*x +' num2str(CoeffwF(3), '%6.4f ') '*x^2 +'
num2str(CoeffwF(4), '%6.4f ') '*x^3'])
title('Fourier Polynomial Approximation')
xlabel('x')
ylabel('y')

figure(4)
bar(abs(awF), 'b')
awF
% figure(4);plot(x,y,'o',t,tpnwc)
% legend('data','Hermite Poly Approximation') % ,'Weighted Hermite Poly
Approximation')
% %text(-.8,6,['Eq= ' num2str(CoeffH(1), '%6.4f ') '+' num2str(CoeffH(2),
'%6.4f') '*x +' num2str(CoeffH(3), '%6.4f ') '*x^2 +' num2str(CoeffH(4),
'%6.4f ') '*x^3 +' num2str(CoeffH(5), '%6.4f ') '*x^4'])
% text(5.0,-0.5,['Eq= ' num2str(CoeffH(1), '%6.4f ') '+' num2str(CoeffH(2),
'%6.4f') '*x +' num2str(CoeffH(3), '%6.4f ') '*x^2 +' num2str(CoeffH(4),
'%6.4f ') '*x^3 +' num2str(CoeffH(5), '%6.4f ') '*x^4'])
% %legend('Location','SE')
% title('Hermite Polynomial Approximation')
% xlabel('x')
% ylabel('y')

% figure(5);plot(x,y,'o',t,tpnwc)
% legend('data','Chevyshev Poly Aproximation') % ,'Weighted Chevyshev Poly
Aproximation')
% %legend('Location','SE')
% %text(0,6,['Eq= ' num2str(CoeffC(1), '%6.4f ') '+' num2str(CoeffC(2),
'%6.4f') '*x +' num2str(CoeffC(3), '%6.4f ') '*x^2 +' num2str(CoeffC(4),
'%6.4f ') '*x^3'])
% %%text(5.0,-0.5,['Eq= ' num2str(CoeffC(1), '%6.4f ') '+'
num2str(CoeffC(2), '%6.4f') '*x +' num2str(CoeffC(3), '%6.4f ') '*x^2 +'
num2str(CoeffC(4), '%6.4f ') '*x^3 +' num2str(CoeffC(5), '%6.4f ') '*x^4'])
% title('Chevyshev Polynomial Approximation')
% xlabel('x')
% ylabel('y')

fclose(fid2);

% -----
% ----- Additional functions -----
function p=FourierPoly(x, number)
p(1) = 1.0;

for i = 2 : number+1
    p(i) = cos(2.0*pi*(i-1)*x);
end

% p(2) = cos(x);
% p(3) = cos(2*x);
% p(4) = cos(3*x);
% p(5) = cos(4*x);
% p(6) = cos(5*x);
% p(7) = cos(6*x);
% p(8) = cos(7*x);

```

```

% p(9) = cos(8*x);
% p(10) = cos(9*x);
% p(11) = cos(10*x);
% p(12) = cos(11*x);
% p(13) = cos(12*x);
% p(14) = cos(13*x);
% p(15) = cos(14*x);
% p(16) = cos(15*x);
% p(17) = cos(16*x);
% p(18) = cos(17*x);
% p(19) = cos(18*x);
% p(20) = cos(19*x);
% p(21) = cos(20*x);
% p(22) = cos(21*x);
% p(23) = cos(22*x);
% p(24) = cos(23*x);
% p(25) = cos(24*x);
% p(26) = cos(25*x);
% p(27) = cos(26*x);
% p(28) = cos(27*x);
% p(29) = cos(28*x);
% p(30) = cos(29*x);
% p(31) = cos(30*x);

for i = number+2 : 2*number+1
    p(i) = sin(2.0*pi*((i-1)-number)*x);
end

% p(32) = sin(x);
% p(33) = sin(2*x);
% p(34) = sin(3*x);
% p(35) = sin(4*x);
% p(36) = sin(5*x);
% p(37) = sin(6*x);
% p(38) = sin(7*x);
% p(39) = sin(8*x);
% p(40) = sin(9*x);
% p(41) = sin(10*x);
% p(42) = sin(11*x);
% p(43) = sin(12*x);
% p(44) = sin(13*x);
% p(45) = sin(14*x);
% p(46) = sin(15*x);
% p(47) = sin(16*x);
% p(48) = sin(17*x);
% p(49) = sin(18*x);
% p(50) = sin(19*x);
% p(51) = sin(20*x);
% p(52) = sin(21*x);
% p(53) = sin(22*x);
% p(54) = sin(23*x);
% p(55) = sin(24*x);
% p(56) = sin(25*x);
% p(57) = sin(26*x);
% p(58) = sin(27*x);
% p(59) = sin(28*x);

```



```

% p(6) = sin(29*x);
% p(61) = sin(30*x);

% p=p';
% -----
function p=ChevyshevPoly(x)
p(1)=1;
p(2)=x;
p(3)=2*x^2-1;
p(4)=4*x^3-3*x;
p(5)=16*x^5-20*x^3+5*x;

%p(6)=32*x^6-48*x^4+18*x^2-1;
%p(7)=64*x^7-112*x^5+56*x^3-7*x;
% p=p';
% -----
function p=HermitePoly(x)
p(1)=1;
p(2)=2*x;
p(3)=4*x^2-2;
p(4)=8*x^3-12*x;
p(5)=16*x^4-48*x+12;

%p(6)=32*x^5-160*x^3+120*x;
%p(7)=64*x^6-480*x^4+720*x^2-120;
% p=p';
% -----

```

